Johannes Steurer, BSc

Helium Droplet Mediated Fabrication and Analysis of Noble Metal Nanoparticles

Master Thesis

For obtaining the academic degree
Diplom-Ingenieur

Master Programme of
Technical Physics

Graz University of Technology

Supervisor:
Univ.-Prof. Mag. Dr.rer.nat. Wolfgang E. Ernst
Institute of Experimental Physics

Graz, April 2014

Deutsche Fassung:
Beschluss der Curricula-Kommission für Bachelor-, Master- und Diplomstudien vom 10.11.2008
Genehmigung des Senates am 1.12.2008

EIDESSTATTLICHE ERKLÄRUNG

Ich erkläre an Eides statt, dass ich die vorliegende Arbeit selbstständig verfasst, andere als die angegebenen Quellen/Hilfsmittel nicht benutzt, und die den benutzten Quellen wörtlich und inhaltlich entnommenen Stellen als solche kenntlich gemacht habe.

Graz, am …………………………… ………………………………………………..
(Unterschrift)

Englische Fassung:

STATUTORY DECLARATION

I declare that I have authored this thesis independently, that I have not used other than the declared sources / resources, and that I have explicitly marked all material which has been quoted either literally or by content from the used sources.

…………………………… ………………………………………………..
date (signature)

Danksagung

Während meiner Diplomarbeit hatte ich die Möglichkeit, in einem noch recht jungen Forschunsgebiet mitzuarbeiten und die aufregende Luft der Grundlagenforschung zu schnuppern. Bei meinen Betreuern Philipp Thaler und Alexander Volk sowie auch Prof. Wolfgang Ernst möchte ich mich für die gute Betreuung und Unterstützung während meiner Arbeit und für viele interessante Gespräche und Diskussionen bedanken.

Mein besonderer Dank gilt meinen Eltern. Danke für das Ermöglichen meines Studiums und die Unterstützung bei all meinen Entscheidungen.

Sehr dankbar bin ich meiner Freundin Lucia. Neben dem Aufwarten mit köstlichem Essen nach langen Messtagen und dem kritischen Beurteilen meines Vortrages war sie immer für mich da und hat mich unterstützt.

Meinen Studienkollegen möchte ich für die gesellige Zeit und das sehr freundschaftliche Umfeld während des gesamten Studiums danken.

Abstract

Helium Droplet Mediated Fabrication and Analysis of Noble Metal Nanoparticles

The synthesis of nanoparticles in superfluid helium nanodroplets is an emerging technique. The droplets provide a unique ultracold and least perturbing environment and deliver the ability to control the growth process of nanoparticles as well as to produce more complex structures like core-shell-nanoparticles. Time-of-flight mass spectroscopy is an excellent way to obtain insight in the nanoparticles' composition. In this thesis the even-odd-effect and the occurrence of magic numbers in the abundance pattern were analysed for gold and silver nanoparticles as well as for water on noble metal nanoparticles. In addition, helium solvation shells were observed.

Nanoparticles were deposited onto substrates for further analysis with transmission electron microscopy. The images obtained, present evidence for the existence of vortices in superfluid helium droplets under certain nozzle conditions in the form of track-like shaped nanoparticles. The morphology of these nanowires was determined and a detailed energy dispersive X-ray spectroscopy analysis of multiply doped droplets revealed a core-shell structure, corresponding to the growth sequence.

Kurzfassung

Herstellung und Analyse von Edelmetall-Nanopartikeln in Heliumtropfen

Die Synthese von Nanopartikeln in suprаflüssigen Helium-Nanotröpfchen ist eine noch junge, aufkommende Technik. Die Heliumtropfen bilden eine ultrakalte und sehr reaktionsarme Umgebung, weswegen sie sich besonders gut zur kontrollierten Herstellung von komplexen Strukturen, wie Kern-Schalen-Nanopartikeln, eignen. Flugzeitmassenspektroskopie ist ein geeigneter Zugang, um Einblick in die Zusammensetzung der produzierten Nanopartikel zu erhalten. Im Zuge dieser Arbeit wurde der sogenannte even-odd-Effekt und das Auftreten von magischen Zahlen in Massenspektren für Gold- und Silber-Nanopartikel analysiert. Außerdem wurden Helium Solvatationsschalen und der even-odd-Effekt für Wasser an Edelmetall Nanopartikeln beobachtet.

Nach ihrer Erzeugung im Heliumtropfen wurden die Nanopartikel, zur Analyse mittels Transmissionselektronenmikroskop, auf ein Substrat deponiert. Aus den erhaltenen Bildern lassen sich Anzeichen für die Existenz von Quantenwirbeln in supraflüssigen Heliumtröpfchen, in Form von länglichen Nanopartikeln, erkennen. Die Morphologie dieser Nanodrähte wurde bestimmt und eine energiedispersive Röntgenspektroskopie von mehrfach dotierten Tropfen zeigte eine Kern-Schalen-Struktur der Nanodrähte, die mit der Dotierungsreihenfolge übereinstimmt.

Contents

List of Figures

List of Tables

Abbreviations

Ag	silver
Au	gold
Cs	cesium
Cu	copper
He	helium
Na	sodium
Rb	rubidium
Xe	xenon

ADC	analog-to-digital converter
Dh	dodecahedral
EDX	energy-dispersive X-ray spectroscopy
fcc	face centred cubic
FWHM	full width at half maximum
Ih	icosahedral
lN_2	liquid nitrogen (boiling point $T_\mathrm{b} = -196\,^\circ\mathrm{C}$)
HRSTEM	high resolution scanning transmission electron microscopy
HRTEM	high resolution transmission electron microscopy
HV	high voltage
MC	main chamber
MCP	micro channel plate
PID	proportional-integral-derivative
PU	pickup
PUC	pickup chamber
QCM	quartz crystal microbalance
QMS	quadrupole mass spectrometer
SC	source chamber
SEM	scanning electron microscopy
TEM	transmission electron microscopy

TOF	time of flight
TOFMS	time of flight mass spectrometer
UHV	ultra high vacuum ($p < 10^{-7}\,\mathrm{mbar}$)

Introduction

In general a cluster is a particle consisting of at least two or three and up to several millions of atoms [1]. Since the dimensions of such particles are in the nanometre range they are often called nanoparticles. They fill the gap between atoms or molecules and bulk materials. In the following the term "droplet" is used for the liquid He clusters (He_N) and the term "cluster" is used for compounds of other materials (D_n, where D is an arbitrary element).

"Nanoparticles or clusters can be fabricated through bottom-up and top-down approaches. With top-down methods large objects are modified into nanostructures, for example, by chemical lithography, plasma methods, beam techniques (electron beam, ion beam, and lasers) and mechanical processing. Many top-down approaches have been developed to produce well defined structures for industrial applications. However, top-down methods generally have severe limitations for producing structures in the size range $< 10\,\mathrm{nm}$ and it is a challenge to elaborate 3-D features [2]."
With bottom-up methods on the other hand the growth process can be controlled by sequential addition of atoms which self-assemble into a cluster. Hence more complex nanoparticles can potentially be fabricated. The fabrication process with bottom-up methods is, however, much more complicated than with the top-down approach. Several quantities, like the size, crystal structure and arrangement of different atom species are crucial for the properties of the resulting nanoparticle [3, 4]. They have a wide area of application, like solar cells [5], medicine [6, 7], catalysis [8], electronic devices [9] and even on historical windows as lustre on majolicas [10]. Common bottom-up techniques are the wet-chemical fabrication of nanoparticles or inert-gas aggregation. A more exotic approach for the fabrication of nanoparticles is the condensation of atoms (dopants) in a beam of superfluid helium (He) nanodroplets (He_N). The subsequent addition of atoms to the droplet allows a high controllability of the growth process. The He droplets provide confinement and ultracold temperatures and thus can be called nano reactors [11, 12]. Additionally, the chemical inertness of He prevents the contamination of the nanoparticle and allows the growth out of highly reactive materials [2].

An apparatus for the production and analysis of nanoparticles in a He_N beam was partly built up and characterised during this thesis (described in Chap. 2). Especially the characterisation and the gain of a deeper understanding of the new assembled time-of-flight mass spectrometer was a major part of this work. Within the mass spectroscopic measurements anomalies in the abundance pattern of the cluster sizes, so called magic numbers, were found. Their origin could be attributed to structurally stable atom arrangements and electronic shell effects. Additionally the even-odd-effect due to electron pairing effects was observed for small clusters and He solvation shells were analysed for silver (Ag) and gold (Au). All these results are given in Chap. 3.

Transmission electron microscopy revealed the successful fabrication of Au and Au/Ag nanowires in vortices of $\mathrm{He_N}$ (see Sec. 3.10). Additionally, core-shell structured nanowires could be reported for the subsequent doping of the He droplet beam with both Au and Ag, after energy dispersive X-ray spectroscopy.

Chapter 1

Theoretical Background

1.1 Formation of Helium Droplets

There are many He droplet beam machines for different purposes like the synthesis of clusters or spectroscopic experiments [12]. In these machines the He droplets are formed via adiabatic supersonic expansion of highly purified ^{4}He under a certain stagnation pressure ($p_0 = 10$ to $50\,\text{bar}$) and temperature ($T_0 = 3$ to $25\,\text{K}$) through a nozzle (typically $5\,\mu\text{m}$ in diameter) into vacuum [11]. Thereby the droplet formation process can be tuned by variation of the He stagnation pressure and the nozzle temperature (see Sec. 1.2).

Depending on the nozzle conditions there exist different growth mechanisms for He_N, assigned to different regimes in the phase diagram of He (see Fig. 1.1) [13, 14]:

- **Subcritical Regime** (regime I): is present at source conditions where $T_0 > 12\,\text{K}$ and $p_0 = 20\,\text{bar}$. Gaseous He expands and the temperature drops linearly with the pressure until the gas-liquid-line is crossed. The He condenses into droplets.
- **Supercritical Regime** (regime III): for $T_0 \lesssim 9\,\text{K}$ and a pressure of $p_0 = 20\,\text{bar}$ the He liquidises already within the nozzle. Hence droplets are formed by disintegration of the liquid phase.
- **Intermediate Regime** (regime II): the isentropes pass near the critical point and unstable behaviour is expected.

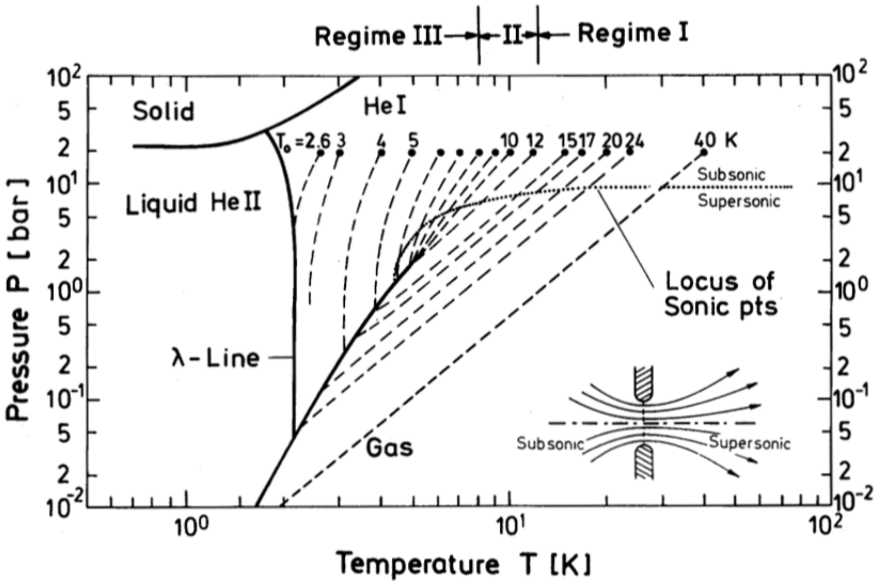

Figure 1.1: Pressure-temperature phase diagram for ^{4}He. The dashed lines are the isentropes[1] which describe the nozzle beam expansion starting from a stagnation pressure of $p_0 = 20\,\mathrm{bar}$ and a range of nozzle temperatures T_0 between 2.6 and 40 K. The expansion leads to a drop in temperature. The locus of sonic points (dotted line) specifies the states at the orifice for isentropic expansions starting from $p_0 = 20\,\mathrm{bar}$ (whether it is sub- or supersonic). Taken from Ref. [14].

As one can see in Fig. 1.1 He has no triple point but has a λ-line that separates the normal fluid (He I) from the superfluid state (He II).

The temperature on[2] and inside[3] a ^{4}He droplet was determined to be 0.37 K [15, 16] which is below the He I - He II transitions temperature $T_\lambda = 2.17\,\mathrm{K}$ [17], i.e. He droplets are superfluid, which has been confirmed by the group of Toennies [18]. Also the observation of quantized vortices in $\mathrm{He_N}$ proves their superfluidity (see Sec. 1.4) [19]. The temperature of 0.37 K is maintained by evaporative cooling which is discussed in more detail in Sec. 1.3.

Superfluid He has some unexpected properties like a vanishing viscosity for flow velocities lower than the so-called Landau velocity ($\approx 58\,{}^{m}/_{s}$) [20], which results in a very high mobility of dopants inside the droplet, fountains, flow and creep, and quantized vortices [11, 17, 21]. In addition, superfluid ^{4}He has a unique heat transport mechanism, second sound, which enables it to transport enormous amounts of heat with no temperature gradient [14]. Superfluidity is a consequence of the bosonic nature of ^{4}He which can form a single macroscopic wave function at a low enough temperature. This is called Bose-Einstein condensation [21].

---

[1] The entropy is constant during the expansion process

[2] By population measurements of Zeeman sublevels in the ground state of alkali dimer molecules

[3] By rotationally resolved spectroscopy of SF_6 molecules

On top of that He is transparent for light of a broad spectral range, which clears the way for optical investigations or photoionisation of dopants inside or on a He droplet.

1.2 Helium Droplet Size

To grow clusters with a certain size inside a He droplet it is crucial to know the correlation between the nozzle conditions and the mean size of the resulting He droplets. The bigger the droplets the bigger the resulting mean cluster size, because the probability for pickup is proportional to the geometrical cross-section of the $\mathrm{He_N}$ [11].
The droplet size distribution is different in each regime. It is log-normal for the subcritical regime [22], exponential for the supercritical regime [23] and bimodal for the intermediate regime [24]. A main interest lies in the mean droplet sizes $\langle N_{\mathrm{He}} \rangle$ for different nozzle conditions. Such measurements cannot be done directly with a classical mass spectrometer, e.g. a time-of-flight mass spectrometer (TOFMS), because the droplets will likely be fragmented upon ionisation (see Sec. 3.1) or they are too big to be detected properly. Therefore other methods were used:

1. Deflection of a $\mathrm{He_N}$ beam upon capture of $\mathrm{SF_6}$ molecules from a secondary beam. $\langle N_{\mathrm{He}} \rangle < 10^4$. The size distribution of the droplets was found to fit the log-normal model by the Toennies group [25].

2. Production of charged $\mathrm{He_N}$ upon electron capture and deflection in an electric field. $10^5 < \langle N_{\mathrm{He}} \rangle < 10^7$ [24]. The measured exponential size distribution is depicted in Fig. 1.2.

3. Attenuation (titration) of a continuous $\mathrm{He_N}$ beam through collisions with Ar and He gas at room temperature. $10^5 < \langle N_{\mathrm{He}} \rangle < 2 \cdot 10^{10}$ [26].

All results of these measurements have been summarised by Gomez *et al.* [26] (see Fig. 1.3). Clearly the droplet size has a very strong dependence on the nozzle temperature T_0, especially in the regions around 9 K which corresponds to a change in the $\mathrm{He_N}$ formation regime, as mentioned before. The kink at around 6 K corresponds to the beginning of the Reileigh-breakup of the fluid He jet (see also Sec. 1.4) [11].

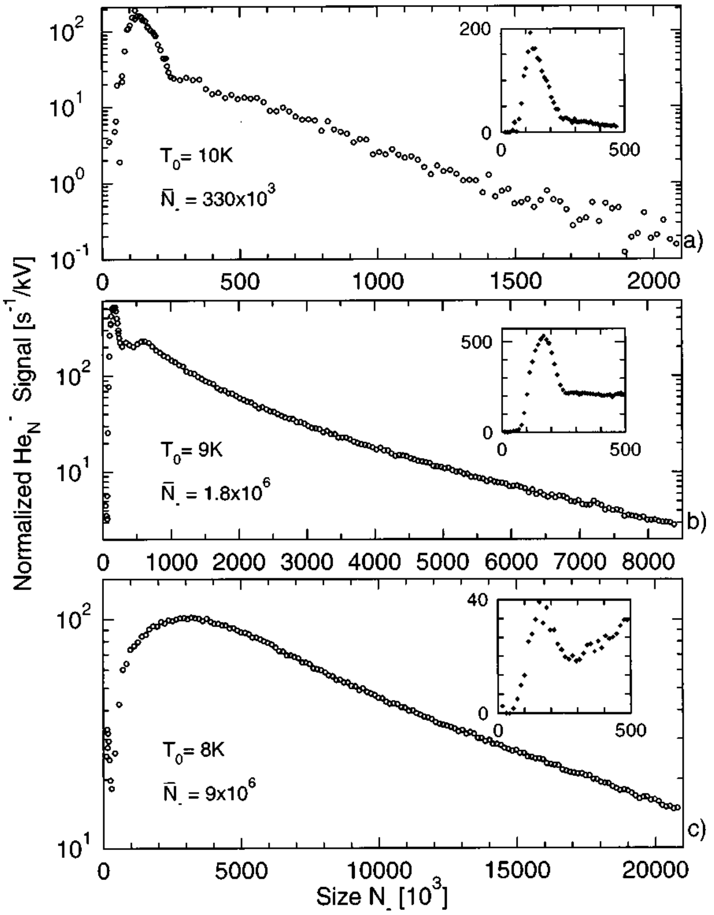

Figure 1.2: Henne *et al.* measured the size distribution for different nozzle temperatures of 8, 9 and 10 K by deflecting the He droplet beam in an electric field after the capture of electrons [24]. The resulting size distributions show an exponential dependence for large droplet sizes. The lower the nozzle temperature gets, the more exponential-like the size distribution becomes [11, 24, 26]. Note the logarithmic ordinate.

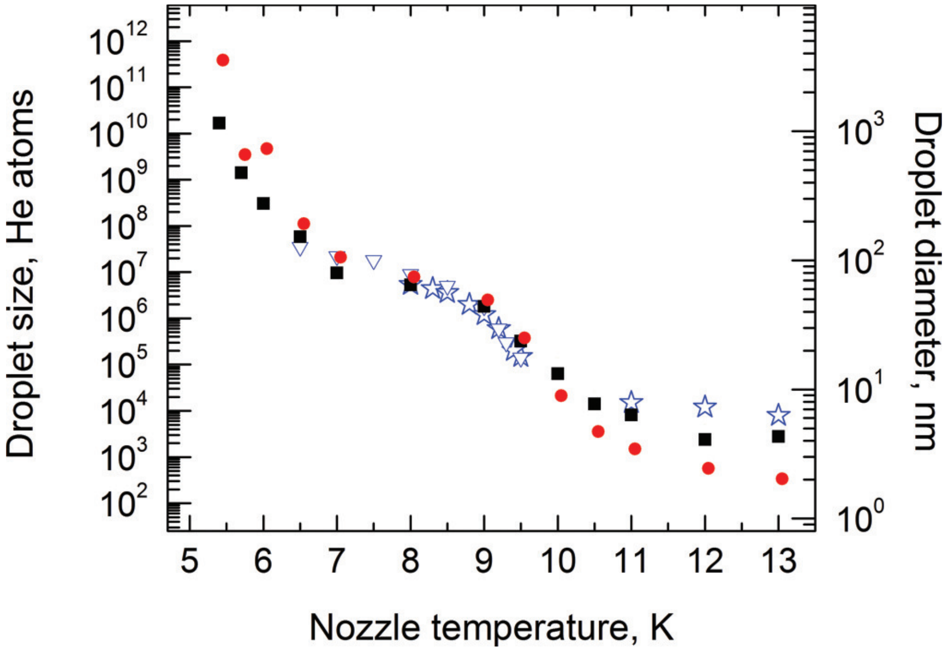

Figure 1.3: Mean droplet size $\langle N_{\mathrm{He}} \rangle$ for different nozzle temperatures T_0 for constant pressure $p_0 = 20\,\mathrm{bar}$. He beam attenuation measurements (method 3 in the above enumeration) for He and Ar pickup are shown by black squares and red circles, open triangles and stars are obtained with method 2 and 1, respectively. Taken from Ref. [26].

1.3 Doping of the Helium Droplets

He droplets have the unique ability to be able to pick up every substance they collide with [27]. That means as long as a species can be forced into the gas phase it can be synthesized in He droplets. For single atom pickup a vapour pressure in the order of 10^{-6} to 10^{-5} mbar is sufficient [11]. The probability of a pickup event was measured by the group of Toennies and determined as a Poisson distribution [28]

$$P_{\mathrm{x}}(k) = \frac{x^k}{k!}e^{-x} \tag{1.1}$$

where x is the average number of collisions between atoms and the He droplet and k the number of atoms or molecules picked up. Because the evaporation of He between successive pickup events is neglected here, this is only valid for rather small x.

The kinetic energy that is transferred from the dopant to the He droplet is dissipated through evaporation of He atoms. The binding energy between a He atom and the droplet is 0.62 meV. An energy transfer of 1 eV to the droplet leads to the evaporation of about 1600 He atoms [12]. If more than one atom is picked up and those atoms form a bond, which they typically do, the released binding energy has to be dissipated too, which results in a much higher He evaporation, e.g. about 4800 He atoms per Ag atom ($E_{\mathrm{b,Ag}} \approx 3\,\mathrm{eV}$ [29]) picked up. The cooling of the droplet after pickup takes place in 10^{-7} to 10^{-9} seconds [30]. Ag is used as an example here and later on, because many of the experiments within this thesis deal with Ag as dopant.

A parameter to describe the loss of He due to evaporative cooling after the pickup of dopants (D) is the beam attenuation A:

$$A = 1 - \frac{p_{\mathrm{He+D}}}{p_{\mathrm{He}}} \tag{1.2}$$

where p_{He} is the partial ^{4}He pressure, monitored with a quadrupole mass spectrometer (QMS) when no pickup occurs (the bare $\mathrm{He_N}$ beam). $p_{\mathrm{He+D}}$ is the respective partial pressure with pickup and entailed beam depletion under the same nozzle conditions. If the background pressure is low enough the absolute pressure approximately equates the partial pressure and can be measured with an ion gauge. Both yield about the same result in experiments (see Sec. 3.2). A is a value between 0 and 1 or 0 and 100 %, respectively.

The resulting cluster size $\langle n_{\mathrm{D}}\rangle$ (where D is the dopant material) under certain pickup and nozzle conditions can be estimated by [31]

$$\langle n_{\mathrm{D}}\rangle = \frac{\Delta p_{\mathrm{He}} \cdot \langle N_{\mathrm{He}}\rangle}{p_{\mathrm{He}}} \cdot \frac{E_{\mathrm{b,He}}}{E_{\mathrm{b,D}}} \tag{1.3}$$

where p_{He} is the partial pressure rise in the chamber where the He droplet beam impacts and all the He in the droplet beam evaporates; $\langle N_{\mathrm{He}} \rangle$ is the mean droplet size for the present nozzle conditions (see Fig. 1.3); Δp_{He} is the drop in the pressure rise p_{He} due to pickup and subsequent evaporative cooling; $E_{\mathrm{b,He}}$ and $E_{\mathrm{b,D}}$ are the binding energies of He to the droplet (0.62 meV) and dopant atom D to the cluster $\mathrm{D_n}$ (e.g. 3 eV for an Ag atom to the $\mathrm{Ag_n}$ cluster), respectively. In this formula the kinetic energy is neglected because $E_{\mathrm{kin,D}} \ll E_{\mathrm{b,D}}$, especially for metal dopants. With Eq. 1.2 this can be written as

$$\langle n_{\mathrm{D}} \rangle = A \cdot \langle N_{\mathrm{He}} \rangle \cdot \frac{E_{\mathrm{b,He}}}{E_{\mathrm{b,D}}} \tag{1.4}$$

After the pickup the dopant can either reside inside the He droplet or on the droplet's surface in a dimple formed around the impurity [11]. Its position can be predicted by calculating the Ancilotto-parameter [32]

$$\lambda = 2^{-1/6} \sigma^{-1} \rho \epsilon R_{\mathrm{m}} \tag{1.5}$$

with σ, the surface tension of the liquid He, ρ the number density, ϵ the depth of the potential well and R_{m} the equilibrium bond length of the He-dopant bond. Basically there are two important cases:

- $\lambda < 1.9$: the dopant resides on the surface of the droplet
- $\lambda > 1.9$: the dopant gets solved inside the droplet.

A proper fabrication of nanoparticles is only possible if the atoms reside inside the He droplet. For metals like Ag and Au this is indeed the case since their respective Ancilotto-parameters are greater than 1.9 ($\lambda \approx 5$ for Ag [33]).

Since the picked up atoms are evaporated they have a thermal kinetic energy and a significant momentum. When they hit a droplet the momentum is transferred. This results in a velocity component perpendicular to the beams direction, i.e. the beam is deflected. This effect can be neglected as long as there is enough He around the dopants, i.e. the beam attenuation A is small. When smaller droplets are doped and/or almost all the He evaporates due to evaporative cooling this has a major effect, as shown in Sec. 3.2.

1.4 Vortices in Helium Droplets

When the He expands through the nozzle at sufficiently low nozzle-temperatures ($T_0 < 6\,\mathrm{K}$ for $p_0 = 20\,\mathrm{bar}$) the gas-liquid transition is passed within the nozzle and droplets are created by the breakup of a fluid He jet (Rayleigh break-up) [11, 14]. During the expansion the fluid is in contact with the nozzle wall. This interaction can induce turbulences in the fluid which can force the droplet into rotation and it will carry a certain angular momentum [19]. At some point the droplet reaches the normal fluid (He I) - superfluid (He II) phase transition temperature of $T_\lambda = 2.17\,\mathrm{K}$ [17] by evaporative cooling. At this point the solid body rotation migrates to the formation of vortices [34].

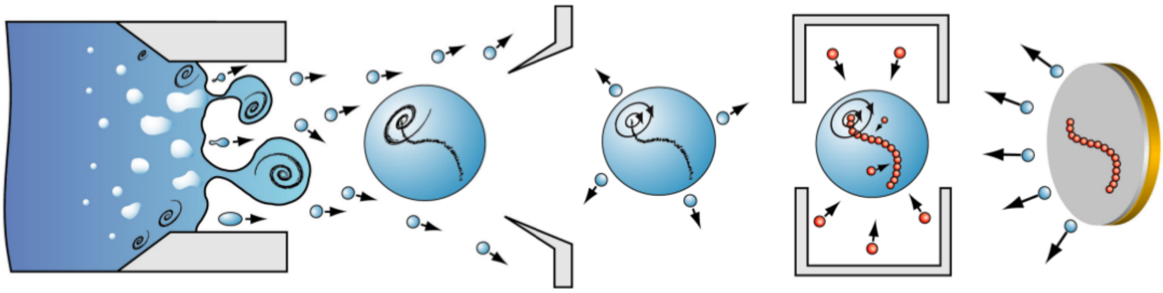

Figure 1.4: He droplets are created by breakup of the liquid He jet and quantum vortices are formed within the droplets. When the droplet is doped, the dopants are likely pinned to the vortex. Taken from Ref. [19].

The fact that impurities in a superfluid are pinned to existing vortices was already shown for bulk superfluid He [35]. Nanowires were grown within these vortices. This is also possible in superfluid He droplets and was first shown by Gomez *et al.* in 2012 [19]. The He droplets evaporate during the impact on the substrate while the particles, arranged in the form of the vortex they were pinned to, are deposited on a substrate and form a two dimensional map of the vortex.

For the formation of vortices in He droplets a certain nozzle temperature is necessary. Gomez *et al.* discovered that nozzle temperatures not higher than 6 K (at $p_0 = 20\,\mathrm{bar}$) are suitable for the formation of vortices [19]. That equals a mean droplet diameter of about 300 nm ($\langle N_{\mathrm{He}} \rangle = 3 \cdot 10^8$) [26].

1.5 Properties of Clusters

Clusters are the intermediate state between atoms or molecules and bulk material. The forces holding a small metal cluster together are like those of covalent bonds, while for bigger clusters the bonds get more and more metal-like [36]. Both, the binding energy and the ionisation potential are dependent on the cluster size n. The binding energy rises with the cluster size [37], while the the ionisation potential decreases until the bulk value, given by the macroscopic work function, is reached [38].

Not only metal clusters can be produced in a He droplet beam, also so called van der Waals Clusters can be synthesized (see Sec. 3.9). Their binding energy is more than an order of magnitude below the one of metal clusters. E.g the Xe-Xe binding energy is about 19 meV [39] compared to 1.65 eV for Ag-Ag [40]. For such clusters the thermal kinetic energy is in the same range as the binding energy and cannot be neglected any more.

1.5.1 Ionisation

For a mass spectroscopic analysis an ionisation process has to take place. Therefore, it is important to know the ionisation mechanisms for bare He droplets and droplets with embedded dopants.

Electron impact ionisation

Due to the much bigger size of the He droplet compared to the dopant and its location in the droplet in the case of Ag and Au, the dopant is almost always covered in He. The mean free path of an electron in a He droplet was calculated to be 2.59 nm for an electron with an energy of 40 eV by Ellis *et al.* [41] and estimated to be 14 nm by Gomez *et al.* for an electron with an energy of 50 eV [26]. Thus direct ionisation of the dopant is very unlikely ($\approx 29\,\%$ for a He droplet with $\langle N_{\mathrm{He}} \rangle = 3000$, which is a very small droplet). Consequently only the He interacts with the electron. When the He is hit by an electron with an energy ($E_{\mathrm{kin}} > E_{\mathrm{ion,He}} = 24.59\,\mathrm{eV}$ [42]) it can be ionized.

$$\mathrm{e}^- + \mathrm{He} \rightarrow \mathrm{He}^+ + 2\mathrm{e}^- \tag{1.6}$$

The resulting He^+ will perform a random walk within the droplet. This effect is called resonant charge hopping [41]. The ionisation energy of the dopant is always smaller than the one for the droplet since He has the highest of all known elements. When a charge transfer from the He^+ to the dopant occurs, excess energy is released, which can lead to fragmentation or an additional excitation of the ionised dopant. In the latter case the relaxation process will result in evaporation of He atoms.

Another possible ionisation mechanism is penning ionisation where a He atom gets excited

$$e^- + \mathrm{He} \rightarrow \mathrm{He}^* + e^- \tag{1.7}$$

and transfers the excitation energy on to the dopant, which can get ionized if the excitation energy is bigger than the dopants (D) ionisation energy [43, 44].

$$\mathrm{He}^* + \mathrm{D} \rightarrow \mathrm{He} + \mathrm{D}^{+(*)} + e^- \tag{1.8}$$

If there is no dopant present the charge hopping goes on, until a charged dimer (He_2^+) is formed. This happens statistically after 11 charge hops [41]. With the hopping distance of 3.1 Å [45] between adjacent He atoms this implies a mean free path of this resonant charge hopping process of about 34 Å. He_2^+ is the most stable He droplet fragment and can yield 30 to 70 % of the total ion yield in mass spectroscopy experiments. That is because ionisation releases excess energy which consequently leads to the evaporation of He atoms. If not all He atoms evaporate the He_2^+ or the resulting He_n^+ can get ejected out of the droplet [46]. This is analysed in detail in Sec. 3.1.2.

Photo ionisation

The big advantage of photo ionisation is the much smaller excess energy as for electron impact ionisation, because the dopant is ionised directly due to the transparency of He. The wavelength can be tuned to exactly match the ionisation energy of a cluster of a certain size. The ionisation energy is slightly dependent on the cluster size [47].

In Fig. 1.5 the two methods are compared by mass spectra of water clusters, produced under different source conditions (different mean cluster size in the beam). Both curves per plot are obtained under the same conditions. The curves with the maximum on the left, i.e. at smaller cluster sizes, originate from a measurement with electron impact ionisation, the curves shifted to the right are obtained with laser ionisation. This is an indication for the cluster fragmentation due to the excess energy when electron impact ionisation is used. The use of very low electron energies to minimise this ef-

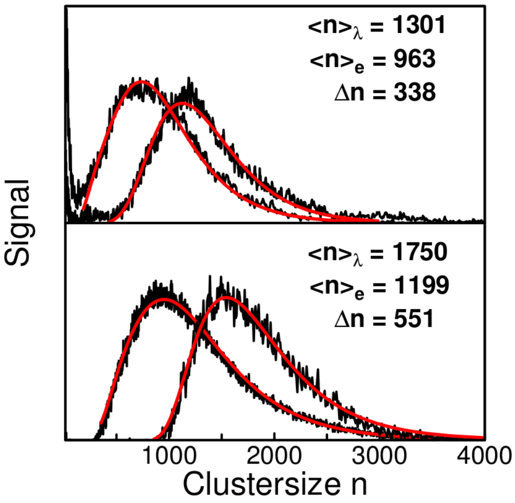

Figure 1.5: Comparison of electron impact and laser ionisation through the example of water clusters. Taken from Ref. [48].

fect is difficult, because of space charge
effects at low acceleration voltages, which
obstruct the production of sufficiently intense electron beams [49].

1.5.2 Deposition on a Substrate

The He droplets used in all experiments within this thesis have a velocity between 150 and 300 $^{m}/_{s}$, as obtained from comparison of the used nozzle conditions and those of Ref. [14]. Since the doping process does not change the droplet's velocity significantly the kinetic energy per dopant atom is $< 0.05\,\mathrm{eV}$ which is much lower than the binding energy of a metal atom to the cluster ($\approx 3\,\mathrm{eV}$ for Ag) or its binding energy to the substrate (e.g. $\approx 1\,\mathrm{eV}$ for amorphous carbon). Thus both, the cluster and the substrate, will remain intact upon the collision. This regime is called "soft landing" [50, 51, 52].

For big clusters the total kinetic energy can exceed the binding energy of all atoms taking part in the impact on the substrate. This would mean that the cluster could get deformed or even be fragmented. The same effect can occur if the binding energy to the substrate is very high and therefore the cluster gains energy in the moment of the impact [51].

When the cluster is surrounded by He, some of the He between the substrate and the cluster will absorb a fraction of the kinetic energy which will then be dissipated by evaporative cooling. Due to the high cooling rate (up to $10^{10}\,^{K}/_{s}$ [53]) a lot of energy can be dissipated during the impact. Thus the He droplet acts as a cushion and can soften the landing of a cluster [54].

1.5.3 Crystal Structure of Clusters

Apart from the bulk crystal structure, e.g. fcc for Ag, in clusters other atom arrangements become possible. From an energetic point of view the preferred crystal structures are icosahedral (Ih) for small, decahedral (Dh) for intermediate and fcc for big clusters [55]. The Ih structure minimizes the surface energy at the price of a big inner strain. The bigger the cluster gets, the more inner strain is built up and the Ih-structure is disfavoured [51, 55]. However, the dependence of the observed structures is different for the production of clusters via inert gas aggregation [56] as well as via $\mathrm{He_N}$.

Five fold symmetries like Ih (see Fig. 1.7) and Dh were reported along with the fcc structure for deposited clusters, fabricated in a He droplet beam [57, 58]. Fig. 1.6 shows a large abundance of five-fold symmetries (like Dh or Ih) for big clusters whereas the highly symmetric fcc structure is dominant for small clusters [57]. The crystal structures were determined from high resolution transmission electron microscopy (HRTEM) images.

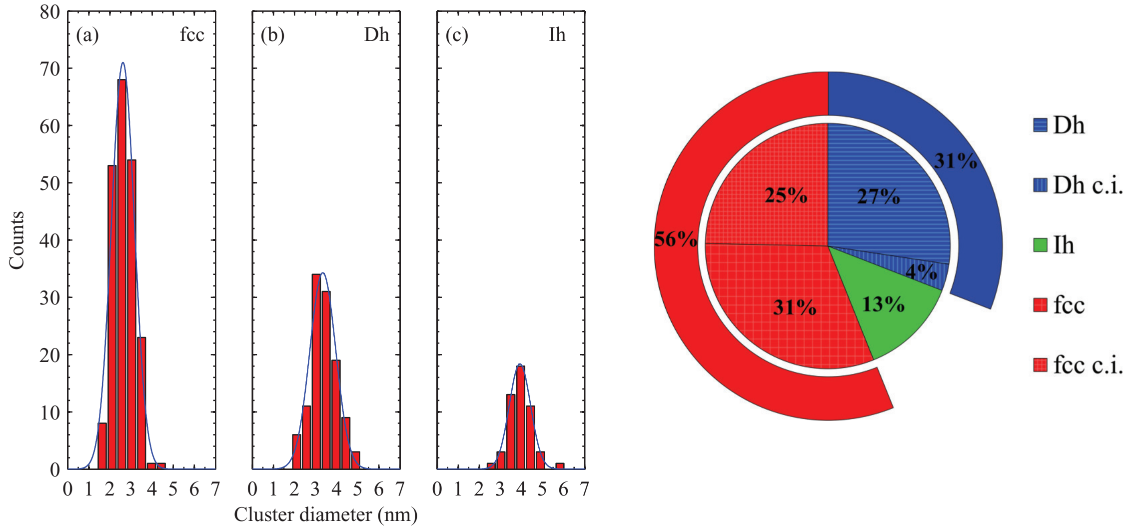

Figure 1.6: On the left side histograms of cluster diameters with fitted Gaussian curves for (a) fcc ($\bar{d} = 2.62(5)\,\mathrm{nm}$, $n \approx 550$), (b) Dh ($\bar{d} = 3.34(7)\,\mathrm{nm}$, $n \approx 1150$), and (c) Ih clusters ($\bar{d} = 3.93(2)\,\mathrm{nm}$, $n \approx 1870$) are plotted. On the right size the relative abundance of the different crystal structures on the substrate are pictured. The analysed Ag clusters were produced in a $\mathrm{He_N}$ beam. Taken from Ref. [57].

For small clusters, as analysed in Fig. 1.6, on the substrate the fcc structure is more common than Dh and Ih. This indicates that small clusters undergo a structural phase transition upon impact due to the interaction potential with the carbon substrate ($\approx 1\,\mathrm{eV}$) [51].

1.5.4 Magic Numbers

In 1984 Knight *et al.* were the first to find anomalies in the abundance pattern of sodium (Na) clusters [49, 59]. They manifest in mass spectra (see e.g. Fig 3.41), where clusters with a number of atoms equal to a magic number yield larger signals.

These magic numbers can basically have two origins. Van der Waals clusters, like xenon (Xe) clusters, form Ih structures and magic numbers occur when a shell of atoms is closed, as Fig. 1.7 shows. Additionally, dependent on the clusters size, other structures can be preferred (e.g. Dh). They are associated with another set of magic numbers [55]. However, there are other peaks in the mass spectrum not associated with closed atomic shells. They can be explained by a combination of clusters with magic numbers and other symmetric shapes. E.g. a cluster with 19 atoms is a 13 atoms cluster, which is a magic number, with a capped pentagonal pyramid attached to it, i.e. a double icosahedron.

The magic numbers Knight *et al.* observed for the ionic Na clusters occur because of electronic shell effects. Noble metals have a similar electronic configuration ($n\mathrm{d}^{10}(\mathrm{n}+1)\mathrm{s}^1$) like alkalimetals ($m\mathrm{p}^6(\mathrm{m}+1)\mathrm{s}^1$), e.g. Na: they both have a single s electron in the outer shell. For the occurrence of magic numbers for both the same conditions

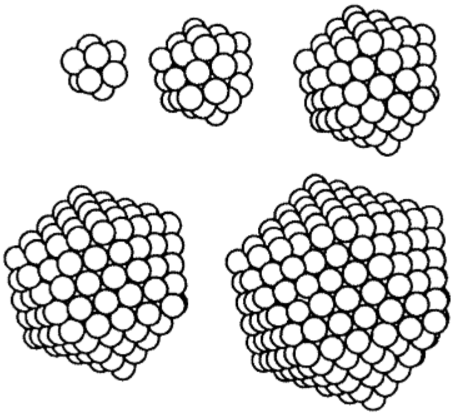

Figure 1.7: Icosahedral configurations with closed shells. The number of atoms required to get these geometrical arrangements are n = 13, 55, 147, 309 and 561, respectively. Taken from Ref. [49].

hold true. In Fig. 1.8 the effective potential of a neutral Na_{20} cluster is illustrated as an example.

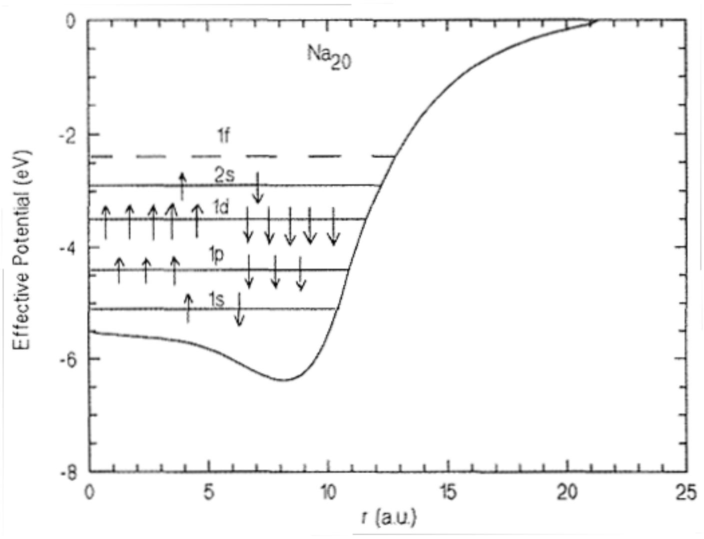

Figure 1.8: The effective potential of a Na_{20} cluster in the spherical jellium model. Taken from Ref. [49].

The 20 valence electrons of the single atoms are subsequently filled into subshells (1s, 1p, 1d, 2s ...) associated with the cluster. If one more atom is added to the cluster, its electron is placed into the 1f-shell. I.e. the cluster with 21 atoms has a lower ionisation potential, hence can be ionised easier, than the one with e.g. 20 atoms [49]. Under the same ionisation conditions this leads to a higher yield in the mass spectra. In Tab. 1.1 a few magic numbers are listed with the corresponding filled shells for Na as an example. When the cluster gets bigger, the shells get narrower. At some point they evolve into the solid-state like bands [49].

Table 1.1: Cluster sizes associated with magic numbers for atoms with one valence electrons (e.g. Na, Ag, Au). Shells are filled according to the spherical jellium model. Derived from Ref. [60].

Cluster size n	filled electron shells
2	$1s^2$
8	$1s^2 1p^6$
18	$1s^2 1p^6 1d^{10}$
20	$1s^2 1p^6 1d^{10} 2s^2$
34	$1s^2 1p^6 1d^{10} 2s^2 1f^{14}$
40	$1s^2 1p^6 1d^{10} 2s^2 1f^{14} 2p^6$
58	$1s^2 1p^6 1d^{10} 2s^2 1f^{14} 2p^6 1g^{18}$
68	$1s^2 1p^6 1d^{10} 2s^2 1f^{14} 2p^6 1g^{18} 2d^{10}$
70	$1s^2 1p^6 1d^{10} 2s^2 1f^{14} 2p^6 1g^{18} 2d^{10} 3s^2$
92	$1s^2 1p^6 1d^{10} 2s^2 1f^{14} 2p^6 1g^{18} 2d^{10} 3s^2 1h^{22}$

Chapter 2

Experimental Setup

In this chapter the apparatus, used for all the measurements within this thesis, is described. Basically it consists of three vacuum chambers (source-, pickup-, and main-chamber) which can be separated by valves. They are described in more detail in Sec. 2.1 - 2.4. For diagnostics a quadrupole - and a time-of-flight mass spectrometer (see Sec. 2.4.2) are used. Additionally deposition rates can be determined with a quartz crystal microbalance (see Sec. 2.4.1). Fig. 2.1 shows a schematic of the apparatus. The single parts are described in more detail later on.

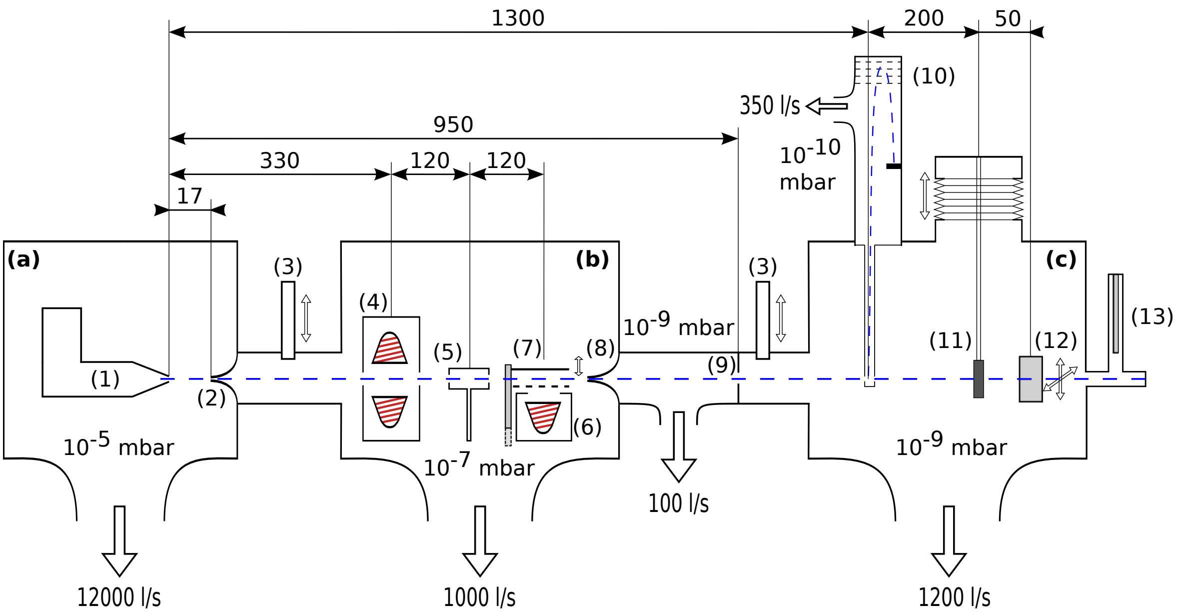

Figure 2.1: Sketch of the experimental setup. (a) source-; (b) pickup-; (c) main-chamber; (1) He nozzle; (2) skimmer (0.5 mm diameter); (3) gate valves; (4) water cooled resistively heated Au evaporation cell; (5) gas-pickup cell (Xe); (6) water cooled resistively heated Ag evaporation cell (crossed beam setup); (7) beam flag to engage Ag pickup (the solid line symbolises the opened state); (8) skimmer (3 mm diameter); (9) Cu orifice (3x8 mm); (10) reflectron time-of-flight mass spectrometer; (11) substrate holder; (12) quartz crystal microbalance; (13) QMS. The dimensions are given in mm. Typical pressure values with the He droplet beam off are indicated. The trajectory of the He droplet beam is drawn as dashed blue line.

2.1 Source Chamber

In the source chamber the He droplet beam is produced by adiabatic supersonic expansion (see Sec. 1.1) of He with a purity of 99.9999 % through a nozzle plate (1) with a nominal diameter of 5 μm. The nozzle plate is pictured in Fig. 2.2.

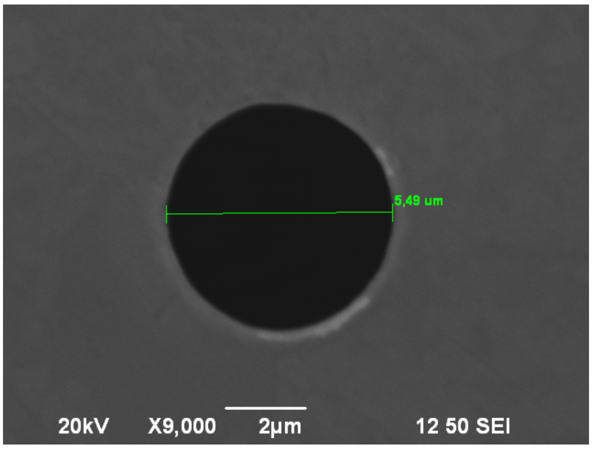

Figure 2.2: SEM image of the nozzle palate. The measured diameter is 5.49 μm in contrast to the specified nominal diameter of 5 μm.

The nozzle construction is connected to the 2^{nd} stage of a two stage coldhead[1] which uses He as the process gas in a Gifford-McMahon cyclic process. The construction is surrounded by a radiation shield, which is connected to the 1^{st} stage of the coldhead. The nozzle can be positioned with a manipulator which allows shifting in the two directions perpendicular to the beam to be able to align nozzle and skimmer properly in order to get maximum He flux.

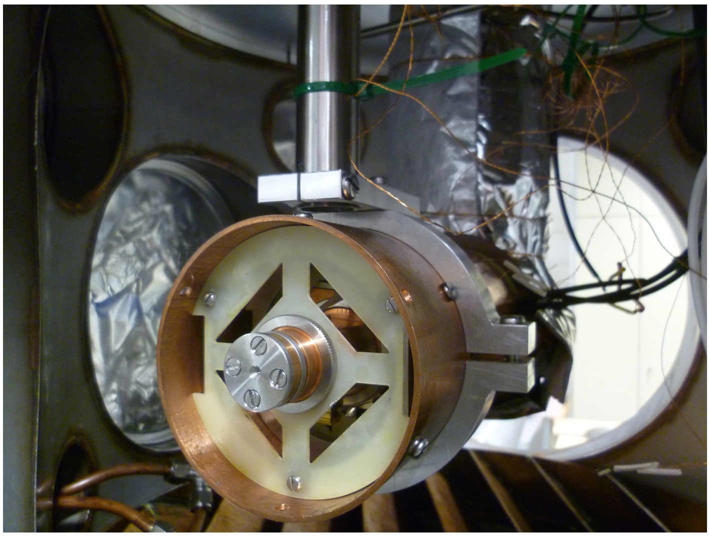

Figure 2.3: He nozzle mounted in the source chamber. The outer copper tube (radiation shield) is cooled down to about 45 K. The nozzle in the middle can be cooled as low as 6 K.

The nozzle position is optimised by looking at the pressure in the differential pumping stage while the valve to the main chamber (MC) is closed and the He droplet beam is on. The higher the pressure, the better is the alignment of the beam. Typical pressure values are given in Tab. 2.1.

Table 2.1: Typical pressure values in the differential pumping station (DPS) (p_{DPS}) with closed valve to the MC for aligning the He nozzle at the source conditions $T_0 = 9\,\text{K}$ and $p_0 = 50\,\text{bar}$.

	p_{DPS}
good alignment	$1.7 \cdot 10^{-7}$ mbar
bad alignment	$4 \cdot 10^{-8}$ mbar

To end up with a droplet beam, a skimmer with a diameter of 0.5 mm (sketched in Fig. 2.4) at a distance of about 17 mm downstream from the nozzle is used. As intended, most of the He intensity is lost due to the skimmer. The amount of He that contributes to the beam is called skimmer efficiency, is dependent on the source conditions and varies from 0.04 % for high nozzle temperatures $T_0 > 20\,\text{K}$ and goes

---

[1] ”RDK-408D2” from sumitomo cryogenics

up to 10 % for $T_0 = 5\,\mathrm{K}$ [61]. Because of the large He flux into the source chamber a diffusion pump with a very high throughput (12000 $^{l}/_{s}$ for N_2) is used.

2.2 Pickup Chamber

After passing the source-skimmer the droplet beam passes through the pickup chamber. Here the droplets are doped with either Au (4), Ag (6) or a gas (5). An illustration of the pickup process for a metal can be found in Fig. 2.4.

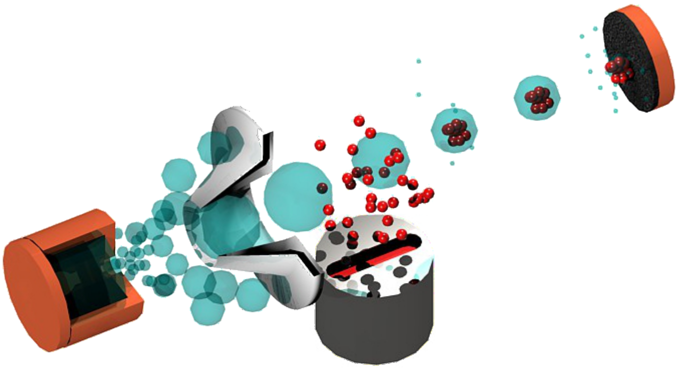

Figure 2.4: Illustration of the pickup process with a crossed beam setup.

To synthesize a metal cluster in a He droplet the metal has to be evaporated. For doing this, two different setups were used in the apparatus, a crossed beam setup and a closed evaporation cell, which are described in the following sections 2.2.1 and 2.2.2, respectively. For both cases resistively heated crucibles[2] were used to heat up the metal.

2.2.1 Crossed Beam Setup

In this design the passing He droplet beam is hit by evaporated atoms in one direction under an angle of about 90°. The tungsten crucible is covered with a sheet made of tantalum (see Fig. 2.5a). This way loss of Ag atoms and the heat flow to the cooling shield due to radiation are minimised. To avoid heating up temperature sensitive parts inside the chamber by radiation the crucible ($T_{\mathrm{crucible}} > 1000\,^{\circ}\mathrm{C}$) is housed in a water cooled copper shield (see Fig. 2.5b).

The first design was equipped with a thermocouple (type C) to measure and control the metal temperature. The thermocouple is housed in a ceramic husk to avoid direct contact with the metal. The oven temperature was controlled (and held constant) by a LabView-program in order to get and retain the same doping/pickup conditions. Mass spectroscopic measurements, as well as measurements of the deposition rate showed

---

[2] TED-Pella Aluminia Coated Tungsten Wire Basket, Style 6

poor reproducibility of the pickup conditions. Not only the pickup conditions varied at the same measured temperature but also the required power to heat the crucible to the respective temperature.

Although the main criterion specifying the pickup-conditions is the vapour pressure which is only temperature dependent (see. Fig. 3.9), there are certain other influences which can result in different pickup conditions and thus different deposition rates:

- Since the crucible is formed like a cone the effective surface of which the metal can evaporate depends on the filling level and can change during a long experiment.
- During long measurements the slit in the cooled shield can narrow due to condensing metal which reduces the flux through the slit.
- The housing of the thermocouple conducts a significant amount of heat[3] which changes when the metal melts and the thermocouple moves. This can result in an error in the temperature measurement.

For further measurements the thermocouple was unmounted at the price of not knowing the temperature any more. The new approach was to monitor the partial pressure for the mass 4 (He) in the MC over time. This mass can only originate from the He droplet beam, hence is an indicator for the He transport. When Ag is picked up in the PC the $\mathrm{He_N}$ beam gets depleted, due to evaporative cooling of the droplets. This results in a lower He signal. The heating power is tuned until the desired beam attenuation is reached. To turn on and off the Ag pickup a beam flag (a shutter) was introduced (see Fig 2.5c). This way the He signal can be monitored (with the QMS and/or the TOFMS) for both cases, with and without pickup and thus the beam attenuation defined in Eq. 1.2 can easily be estimated. This oven design is ideal for initial characterisation measurements, because deposition can be turned on and off on a short time scale. Using the beam attenuation as the criterion for the pickup conditions (heating power of the crucible) leads to a good reproducibility of the experiments.

An electromagnet was used as the actuator for the beam flag. Its coil can be seen in Fig. 2.5b and 2.5c. With an electrical pulse of $> 10\,\mathrm{V}$ the shutter opens and stays open with a reduced voltage $\approx 1.5\,\mathrm{V}$. In the latter case power less than $1\,\mathrm{W}$ is dissipated which allows long measurements without the worry that the coil may overheat.

In a crossed beam setup all dopants hit the droplet in almost the same direction. Thus the momenta in one direction add up and the beam will be deflected. As experiments showed, this can have a major effect (see Sec. 3.2). This is a disadvantage of this setup when it is used for cluster deposition experiments. For the synthesis of small clusters, which are used e.g. in spectroscopic experiments, this disadvantage is obsolete because the beam deflection can be neglected as pointed out it Sec. 1.3.

---

[3] Measurements with and without the ceramic husk revealed that an amount of heat in the order of 50 W is drained through the husk

(a) (b) (c)

Figure 2.5: Image of the crossed beam setup for evaporating Ag. (a): the crucible with the Ta cover (1), the Cu electrodes which hold the crucible in position and provide the heating current (2), the water cooled Cu baseplate and the skimmer can be seen. The beam direction is indicated with the dashed blue line (b): the water cooled Cu shield was mounted over the crucible so that the slits in the Ta sheet and the shield align. (c): the beam flag in the closed state.

2.2.2 Closed Evaporation Cell

Here two crucibles are mounted on top of each other (mirrored), the beam passes between the crucibles (see Fig. 2.6). Electrically they are connected parallel and consequently will statically have about the same temperature[4]. The one at the bottom is filled with the metal to evaporate. Atoms that are evaporated in the bottom crucible are either picked up by the He droplet beam or they arrive at the top crucible and will be reflected and thus will hit the droplet from the opposite direction. With this design the droplet beam is not deflected like in a crossed beam setup, which is crucial for experiments where high beam attenuations, leading to high deposition rates, are desired. At most a slight divergence of the beam occurs which does not have an effect on the experiments.

This design has the disadvantage that the use of a beamflag to quickly determine the beam attenuation due to pickup is no longer possible. For measuring the beam attenuation the oven has to be cooled down until the vapour pressure is low enough that no pickup occurs. In contrast to the crossed beam setup the temperature measurement with a thermocouple, housed in a ceramic husk, yielded satisfying, reproducible results, although the absolute value of the temperature will not be correct. In all further measurements the temperature will be given as T_{TC} to indicate that the given temperature is determined with the thermocouple and is not the actual temperature of the metal. The absolute error was roughly estimated to be 85 °C in Appendix A.4.

---

[4] Not exactly because of the crucibles big fabrication tolerance and thus individual resistance

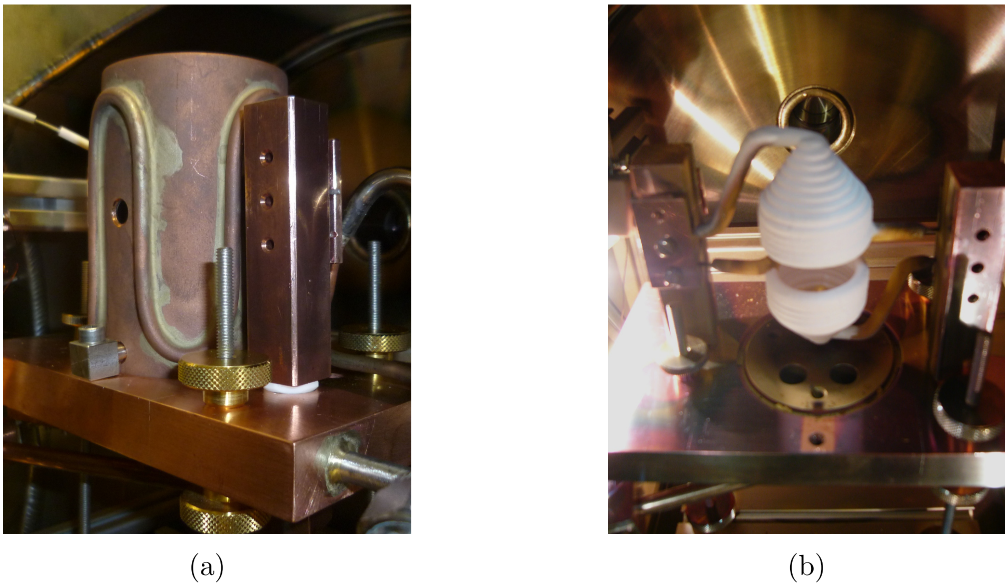

(a) (b)

Figure 2.6: Picture of the symmetric oven design with (a) and without the Cu cooling shield (b).

2.3 Differential Pumping Stage

Coming from the pickup chamber, the beam passes another skimmer (diameter 3 mm) and enters the differential pumping stage. Its function is to smooth the pressure gradient from the PU chamber (10^{-7} mbar) to the MC (10^{-9} mbar) by having a pressure in the range of 10^{-8} mbar (pressures with a present He droplet beam). The low pressure in this region is beneficial to avoid collisions of evaporated He with the droplet that could shrink or even destroy the droplet. Also a badly pumped volume between the skimmer (8) and the Cu orifice (9) is thereby avoided.

2.4 Main Chamber

The main chamber is intended to be oil-free to avoid contamination of both, the droplets and the substrates. Therefore, an oil free fore-pump is used to back the turbo molecular pumps. Since the turbo pumps are lubricated by oil and the He droplet may transport oil from the source chamber, which originates from the diffusion pump, into the MC the vacuum cannot be guaranteed to be 100 % oil free. This becomes manifest in three peaks in the mass spectrum at $m = 203\,\mathrm{u}$, $m = 276\,\mathrm{u}$ and $m = 390\,\mathrm{u}$.

2.4.1 Microbalance

On a x-y-z manipulator in the MC, a quartz crystal microbalance (QCM) is mounted. The relocatability has the advantage that either the deposition rate can be determined or the beamline can be optically inspected by a telescope. Also the deposition rate depending on the location can be determined which is interesting in case of a beam deflection. While depositing onto the QCM the partial pressure of ^{4}He is measured with the QMS ((13) in Fig. 2.1), which can be used as an indicator for the beam attenuation due to evaporative cooling after the pickup process.

Theoretical background

In 1959 Sauerbrey proposed the use of oscillating crystals for weighing thin films [62]. Therefore, a quartz crystal is forced into a thickness shear oscillation. Its natural frequency is then not only dependent on its thickness but also on the mass of deposited material on the surface. The more material is deposited on the surface the slower the motion gets. Since frequencies and especially frequency changes can be measured very accurately this is a very exact method. Fig. 2.7 shows a pure shear oscillation. The antinode of the stationary wave is at the surface. That means only the mass of the deposited material and not its elastic properties influence the crystal's frequency.

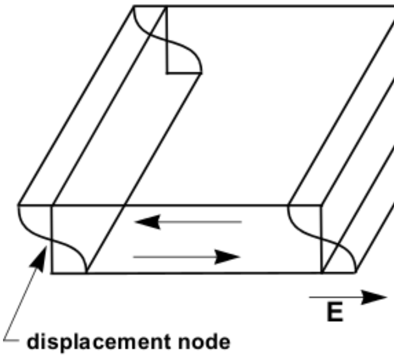

Figure 2.7: Ideal thickness shear oscillation of a quartz plate. The direction of the electric field for exciting the oscillation is indicated. Taken from Ref. [63].

The natural frequency of an ideal thickness shear oscillation is

$$f = \frac{c_{\mathrm{tr}}}{2d} \tag{2.1}$$

where d is the thickness of the crystal and c_{tr} the transversal speed of sound. The frequency change due to a change in thickness is then

$$\frac{\Delta f}{f} = -\frac{\Delta d}{d} = \frac{\Delta m}{\rho A d} \tag{2.2}$$

where Δm is the deposited mass and ρ the density of the deposited material. A is the area of the quartz plate. To measure these frequency changes the quartz crystal is used as the frequency determining component in an active oscillation circuit. It is schematised in Fig. 2.8. If the natural frequency of the crystal changes the frequency in the circuit changes. This frequency change is monitored from which the mass change can be calculated.

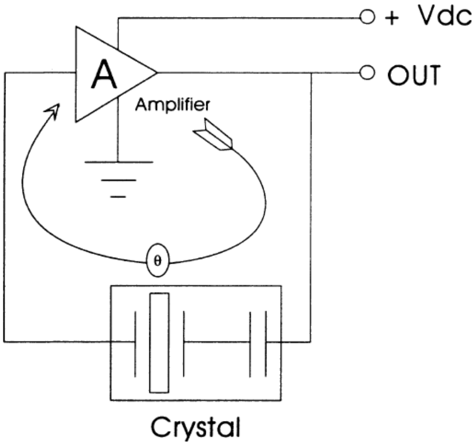

Figure 2.8: Schematic diagram of the active oscillating circuit used to measure the frequency of the QCM. Taken from Ref. [63].

Temperature stabilisation

In a deposition experiment QCM measurements are very useful to get an idea of the actual mass transport of dopant atoms through the He droplet beam. This is crucial to determine the exposure time in deposition experiments when the objective is a certain surface coverage. For the following experiments the QCM "IPN 074-156" from INFICON was used (see Fig. 2.9) which has the following specifications [63]:

- a Resolution of 0.05 Hz at 6 MHz (which is about the frequency the QCM is operated at in all experiments within this thesis)
- and a frequency accuracy of 0.002 % which accords to an uncertainty of 120 Hz

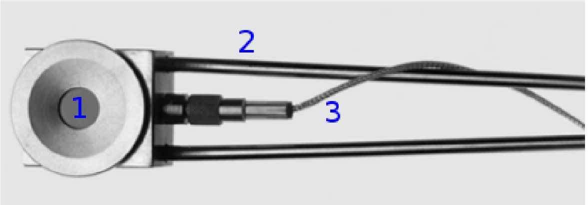

Figure 2.9: The QCM "IPN 074-156" from INFICON, with the quartz crystal (1), the pipes for optional water cooling (2) and the electrical wiring (3). Taken from Ref. [63].

In cluster deposition experiments frequency changes of a few Hz within a couple of minutes are expected which corresponds to deposition rates in the range from 10^{-3} to $10^{-6}\,\frac{\mu\mathrm{g}}{\mathrm{cm}^2\mathrm{s}}$ [57, 64].

To be able to measure in these ranges all frequency shifting effects of the microbalance have to be obliterated. The main frequency shifting effect is the variable room temperature, which leads to virtual deposition rates up to $5 \cdot 10^{-5}\,\frac{\mu\mathrm{g}}{\mathrm{cm}^2\mathrm{s}}$ without stabilisation and variations of the room temperature below ±1 °C. In past experiments with the same microbalance [57], oscillations in the deposited mass that correspond to the cycle of the air conditioning were observed. Those oscillations were attributed to temperature oscillations of the quartz crystal.

In the past the temperature was held constant by a constant water flow through the microbalance. The water was pumped through a reservoir which was held at a constant temperature (±0.1 °C). A more elegant way needed to be found.

The new approach was to use an electrical heater to keep the QCM at a constant temperature. For a good controllability, hence enough heat flow, the temperature to maintain was chosen to be significantly above room temperature ($T_{\mathrm{nominal}} = 50\,^{\circ}\mathrm{C}$).

First some simulations, using the Finite Elements technique, were run to determine the power for an attached heater and whether an available Eurotherm 2132[5] is suitable. The microbalance was modeled as a block of steel and on the opposite side of the quartz crystal, which is the part that needs a constant temperature, a heat source was placed on an attached block made of Cu. The heat can flow off through the two steel pipes for the optional water supply and through radiation. The simulations revealed that the temperature on the side where the quartz crystal is mounted is fairly constant, because the steel housing acts as a lowpass filter.

A standard power resistor ($R = 30\,\Omega$, $P_{\mathrm{max}} = 10\,\mathrm{W}$) was used as a heater. The temperature was measured with a type K thermocouple directly connected to the Eurotherm 2132 controller. The temperature was measured between the block of copper and the housing of the microbalance to keep the oscillations due to the on/off cycles of the controller to a minimum. This setup worked nicely in the pickup chamber ($p \approx 10^{-7}\,\mathrm{mbar}$). As it turned out the resistor, used for the heating, is not UHV compatible. The mass spectrum showed high carbon and hydrocarbon peaks, especially when the resistor was heated up. Therefore, it was replaced by a standard halogen bulb which was also mounted on the opposite side of the quartz crystal.

Closer investigation into the still present temperature dependence of the deposited mass showed, that not only the crystal but also the electronics (oscillating circuit) outside of the vacuum chamber is very temperature sensitive. In the next step the outside electronics was put in a box along with the Eurotherm-controller[6] for the temperature stabilization of the QCM. The box was maintained at a constant temperature significantly above the room temperature, actively controlled by a second Eurotherm-controller with a PT100 resistance thermometer.

---

[5] The controller can just switch on or off the output which might lead to oscillations in temperature

[6] It turned out that the cold junction compensation inside the Eurotherm-controller is also temperature dependent and has to be taken care of.

In Fig. 2.10 the deposited mass is plotted while the aircondition was running. Clearly the oscillations in the QCM-graph correspond to the oscillating temperature induced by the on and off cycle of the aircondition which caused a temperature change as high as ±2 °C. The resulting virtual deposition rates are in the order of $10^{-6}\ \frac{\mu\text{g}}{\text{cm}^2\text{s}}$ in this worst case scenario, which is lower than the usual deposition rates. This stability is satisfying, especially when compared to the virtual deposition rates of up to $5 \cdot 10^{-5}\ \frac{\mu\text{g}}{\text{cm}^2\text{s}}$ before introducing the temperature stabilisation. Additionally a very good stability on a long time scale was achieved. The mass stays within one resolution step ($7.5 \cdot 10^{-5}\ \frac{\mu\text{g}}{\text{cm}^2}$) in time scales > 10 min which equals a virtual deposition rate in the order of $10^{-7}\ \frac{\mu\text{g}}{\text{cm}^2\text{s}}$.

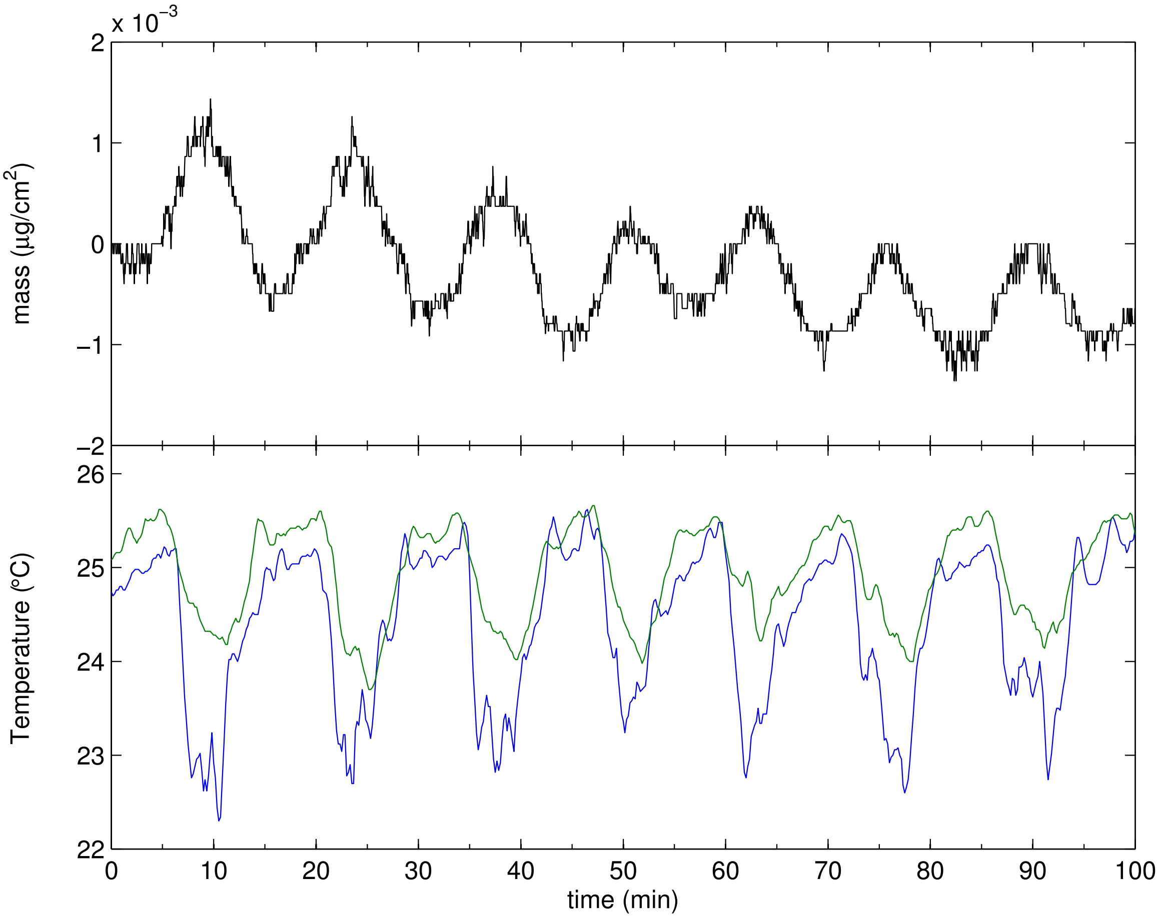

Figure 2.10: Temperature dependence of the QCM-mass signal after temperature stabilisation. In the upper graph the mass, monitored with the QCM, is plotted. In the lower graph the temperatures at two locations in the room are shown. Clearly the oscillations in the mass have their origin in the oscillating room temperature. The shift in time can be explained by the thermal inertia of the system.

Since all temperature critical parts have been thermally stabilized properly the only remaining possibilities for a temperature influence on the measurement are the short coaxial cable that connects the microbalance with the outside electronics and changes in the temperature of the vacuum chamber, which have a minor effect.

2.4.2 Time-of-Flight Mass Spectrometer

For all mass spectroscopic experiments within this work the "Reflectron Time-of-Flight Spectrometer RFT50 with Electron Impact Ionisation and 20 kV Post Acceleration"[7] is used. In the following its function and properties are described briefly.

In mass spectroscopy only charged particles can be analysed. The ions are produced in the ion source of the TOFMS (see Fig. 2.11) with two different techniques:

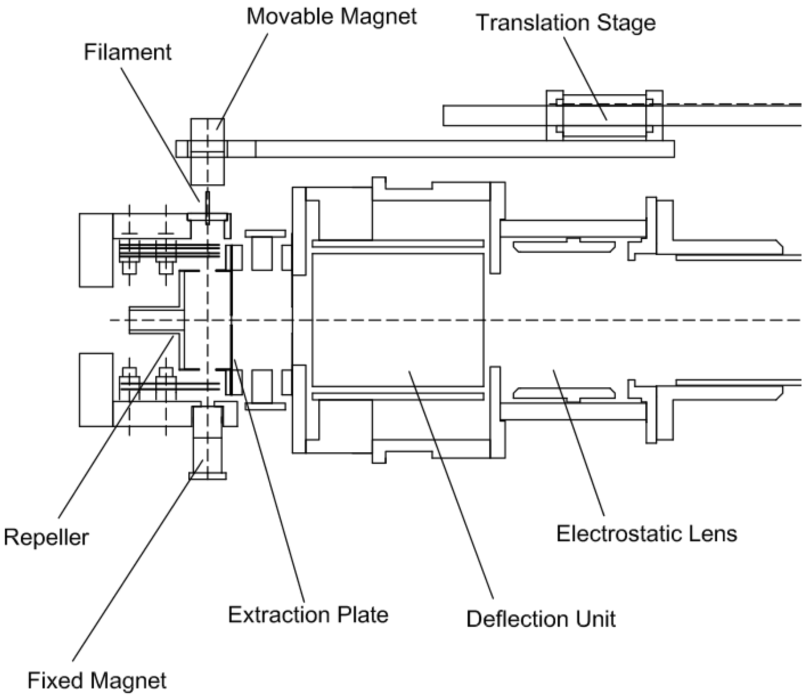

Figure 2.11: Ion source of the TOFMS. The important parts are the filament for the production of electrons if electron impact ionisation is used, the repeller and extraction plates for the extraction of ions and the deflection unit for compensating transversal velocities. Not shown is the laser beam for the optional photo ionisation, which would be perpendicular to the cross section drawn here. Taken from Ref. [65].

Electron impact ionisation

Electrons are emitted by an electrically heated filament. The electrons gain kinetic energy by passing through a known potential U. If an electron with the energy $E = eU$ hits an atom with an ionisation energy below that, the atom will most likely loose an electron and will remain positively ionized (see Eq. 1.6). To ionize as many atoms as possible in a determined volume, the so called ionisation volume (marked as (2) in Fig. 2.12), the electrons are forced on a spiral trajectory by a constant magnetic field which results in a much longer trajectory and therefore yield in a higher ion density inside the ionisation volume.

---

[7] The device is distributed and manufactured by Stefan Kaesdorf - Geräte für Industrie und Forschung

Photo ionisation

If a photon hits an atom with an energy $\hbar\omega$ higher than the ionisation potential of the atom, the atom can loose an electron and remains positively charged. With a photon energy below the ionisation threshold and high laser intensities this also can be done with (resonant) multi-photon-absorption.

Ion extraction

The ions are then extracted from the ionisation volume into the flight tube[8]. This is done by two electrodes, the repeller and the extractor (see Fig. 2.11, marked as (3) and (4) in Fig. 2.12). A short voltage pulse (max. 4800 V) of a variable duration is applied. This pulse is negative for the repeller and positive for the extraction plate, i.e. the ionisation volume is at ground potential. In first approximation all ions traverse the same potential and thus have the same kinetic energy. Hence their velocity depends on their mass. The heavier they are the slower they travel. A closer look reveals that an ion nearer to the extractor gains less kinetic energy than one further away. The point where the nearer ion gets overtaken by the further due to its lower velocity is called primary focal point ("space focusing") [66]. This point is fixed and only depends on the extraction and the liner potential ((5) in Fig. 2.12). That means that the length of the flight path is fixed for constant liner and extraction voltages, because the best resolution is possible if the detector is placed in that point. A common way to operate the TOFMS at different voltages anyway is to introduce a reflectron. Additionally the reflectron extends the time of flight (TOF), hence increases the resolution of the mass spectrometer.

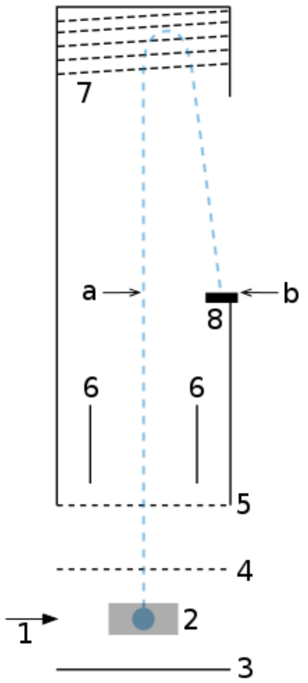

Figure 2.12: Schematics of the TOFMS. Description in the text.

Deflection unit

In Fig. 2.12 a sketch of the TOFMS is pictured. (1) symbolises the electron source which ionises atoms on its way. Only ions from the ionisation volume (2) can contribute to the ion current. Ions outside that volume do not reach the detector (8). After the ions get extracted by the repeller (3) and extractor (4) electrodes they get accelerated to the liner potential (5). Ions with a high transversal velocity component (perpendicular to the ion beam) may not reach the detector because of spacial drift during the flight

---

[8] It is sometimes called "field free drift region"

time. Two electrodes (6) can therefore be set up to deflect the ion beam in the x and y direction (if z is the direction of the ion beam). Those deflection fields are crucial if big clusters are to be detected. For big clusters (e.g. 50 Au atoms) the flight time[9] is in the range of $100\,\mu$s or more[10]. A typical He droplet has a transversal velocity of 100 to $300\,{}^{m}\!/\!{}_{s}$ [14]. That means a transversal drift of a few centimetres, which can be more than the MCP's dimensions. If the deflection unit is set up properly this drift can be compensated. If the deflection voltage is optimised for big masses (e.g. $m = 10000\,\mathrm{u}$) the small masses (e.g. $H_2O \mathrel{\hat{=}} \mathrm{m} = 18\,\mathrm{u}$) are deflected too and may not reach the MCP. Hence not any arbitrary mass range can be properly analysed at once.

Reflectron

The usage of a reflectron has several benefits. First the TOF gets longer by shifting the primary focal point "a" to the point "b", without violating the conditions for space focusing. The higher TOF results in a better resolution. Another important factor is energy focusing. When the ions get extracted from the ionisation volume (2) they have statistically distributed velocities. The velocity components parallel to the ion extraction field are compensated by the reflectron, because faster ions have a longer trajectory through the reflectron because they penetrate deeper into the ion mirror than slow ones. Hence they have a slightly longer TOF. With the reflectron it is possible to change the extraction voltages which results in a shift of the point "a" and would violate the space focus condition in a linear TOF. By choosing the right voltages for the reflectron (called last- and central grid), space and energy focusing in the point "b" can be maintained. It is worth mentioning that achieving complete space and energy focusing at the same time is impossible due to the Liouville theory.

Detection

For detecting the extracted ions a 3-stage micro channel plate (MCP) is used. It has an amplification of about 10^7 [65]. An MCP is an array of 10^4 to 10^7 miniature electron multipliers oriented parallel to one another (see Fig. 2.13); typical channel diameters are in the range of 10 to $100\,\mu$m [67].

When an ion arrives at the MCP it must be guaranteed that it can be detected. Therefore, the channels are tilted by a small angle with respect to the flight path. This way every impacting ion hits the wall of a channel. If it has a sufficient kinetic energy, an electron is knocked out from a channel. A voltage (the MCP voltage) is applied between the faces of the MCP which accelerates this electron towards the wall of the channel. There multiple secondary electrons get knocked out and an electron

---

[9] Time from the pulse for the ion extraction to their impact on the detector

[10] The exact value depends on the settings for the different voltages in the TOFMS

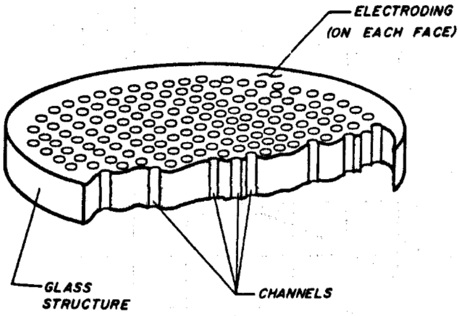

Figure 2.13: A micro channel plate. Taken from Ref. [67].

avalanche is built up which is detected as a current between the faces. After such an electron avalanche the MCP needs some time to regenerate before another event can be registered. This time is in the order of 100 ps [67].

For large clusters the detection probability increases with the velocity. If big clusters are to be detected, their velocities can be too small to be detected properly since every ion has the same kinetic energy. Therefore, a post acceleration field is applied just before the detector. The corresponding voltage can be as high as 20 kV. This way the detection probability for heavy particles can be enhanced significantly [65].

The detection of the current peaks is done by a Multiscaler (Fast P7887) with a time resolution of 250 ps. If multiple ions impact on the detector within this time interval the corresponding peak appears saturated. Because the MCP can be destroyed by very high saturation, a mass filter can be applied [65]. This way the light ions[11] are deflected away from the detector and do not contribute to the mass spectrum any more.

Characterization of the time-of-flight mass spectrometer

The voltages for the repeller and extraction can be chosen freely. Afterwards the liner- and lens voltages are optimised until a signal is found. The difficulty is to find matching voltages for the reflectron, i.e. the last grid and the central grid. They have to be optimised for best resolution, i.e. narrowest peaks. In Tab. A.1 some possible voltage settings for the TOFMS are given. Besides the voltages there is another set of parameters that can be adjusted including pulse durations, time delays and settings for the recording. Not every set of parameters yield the same result. Some are to be preferred for a maximum resolution (up to $\frac{m}{\Delta m} = 10000$ [65]), some for maximal signal, some for minimal noise or for the detection of very big masses. In Tab. 2.2 the influence of some settings are given.

---

[11] Usually there are much more light ions present in the mass spectrum than big ones

Table 2.2: Influences of the different parameters accessible when operating the TOFMS. Partially extracted from [65].

Ion source	
magnet position	for optimisation of the electrometer current to maximise the resulting ion current
filament current	major influence on the resulting ion current; the higher the more signal ($I_{\text{Filament,max}} = 2.6\,\text{A}$)
electron energy	for maximal signal it is set to the maximum of the ionisation cross-section of the element to analyse ($E_{\text{Electron,max}} = 89\,\text{eV}$)
1^{st} aperture	optimise for maximal electrometer current
Voltage settings	
repeller/extraction	higher values are to be used in case of a broad energy distribution (space charge effects or fragmentation)
lens	compensation of a beam divergence; usually set on liner potential
liner	higher potential for shorter flight times (lowers the resolution)
repeller offset	makes sure the ions aren't attracted to the liner → symmetric peaks (important if big masses are to be detected and a long electron beam duration is used)
mass filter	prevents light ions from reaching (and saturating) the detector; exact voltage does not matter for $U > 250\,\text{V}$; after activation the deflection unit should be optimised again
last- and central grid	alternately adjust for best resolution (narrow peaks) to obtain energy focusing
deflection unit	adjust for best overall result (whether small or high masses are of interest)
MCP	major influence on signal yield; higher values necessary for the detection of big masses (max. $U_{\text{MCP}} = 3.3\,\text{kV}$)
Post acceleration	practically always at maximum for best ion detection
Pulse generator	
repetition frequency	number of sweeps per second
duration e-beam	longer duration → higher electrometer current → higher ion current, but more space-charge-effects which lower the resolution
duration ion extraction	make sure the duration is long enough to extract the heavy ions as well (a higher value will do no harm)
duration mass filter	Use when operating at high MCP values to avoid heavy saturation by small masses (e.g. H_2O)
Fast Multiscaler	
number of sweeps	more sweeps → more significant spectrum
range	defines the number of bins (one bin equals a flight time of 250 ps) that are recorded
bin width	lowers the resolution for the advantage of a smaller datafile
Start/Stop Disc.	set the voltage levels above which a signal from the MCP + Preamp is recorded as an event. (0.3/-0.15 are good values)

As stated in Tab. 2.2, four parameters have a dominant influence on the sensitivity of the TOFMS [65]:

- The MCP voltage
- The filament heating current
- The duration of the electron beam
- The discriminator thresholds of the multiscaler

The ideal MCP voltage for the analysis of clusters was extracted by a series of measurements like the one shown in Tab. 2.3. The higher the MCP voltage gets the bigger clusters get visible in the spectrum. As a compromise between proper detection of heavy particles and acceptable saturation for smaller masses a value of 2.7 kV was chosen for further measurements.

Table 2.3: Variation of the MCP voltage U_{MCP} while inspecting the bare He droplet beam ($T_0 = 10\,\mathrm{K}$ and $p_0 = 20\,\mathrm{bar}$). $N_{\max}$ determines the number of He atoms of the biggest $\mathrm{He_N}$ visible in the TOF mass spectrum. $5 \cdot 10^5$ sweeps were recorded for each MCP voltage.

U_{MCP} (kV)	$N_{\max}$
2.5	250
2.6	375
2.7	440
2.8	450
2.9	450

Since a large heating current lowers the lifetime of the filament, a moderate current of lower than 2.4 A should be used for all measurements. To find good values for the discriminator threshold a mass spectrum is recorded with very low MCP voltage (e.g. 1.5 kV). The threshold is then set to the edge where no electrical noise appears in the spectrum any more.

The highest possible electron energy of 89 eV was used for all measurements within this thesis, because the maximum ion yield was obtained with these settings. Since there is always a He droplet involved in the performed mass spectroscopic experiments, this is consistent with the ionisation cross-section of He (see. Fig 2.14a) which has a maximum at about 100 eV. The cross section for double ionisation is about one order of magnitude lower (see. Fig 2.14b). Therefore, all following mass spectra will give the term "mass in u" in the abscissa label rather than the actual quantity which would be the mass to charge ratio. The unity for the mass on an atomic scale is always $1\,\mathrm{u} = 1.660538782(83) \cdot 10^{27}\,\mathrm{kg}$.

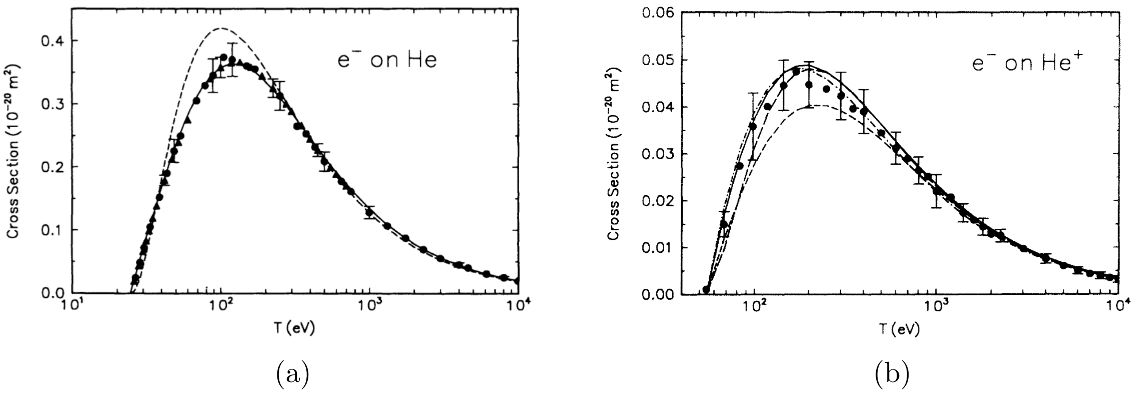

(a) (b)

Figure 2.14: Total cross-section for the ionisation of neutral He atoms (a) and He^+ (b) by electron impact. Calculated by Kim *et al.* and measured by references therein [68].

A double ionisation of the dopant is very unlikely, because of the Coulomb repulsion between the single ionised dopant and the He^+, that performs a resonant charge hopping process [43]. However multiple ionisation can happen by multiple penning ionisation processes [69] where a metastable He atom ionises the dopant (see. Sec. 1.5.1), albeit this likely leads to a charge separation by Coulomb explosion of the cluster [70, 71].

By comparing the spectra of the He droplet beam ($T_0 = 12\,\mathrm{K}$ and $p_0 = 40\,\mathrm{bar}$), up to a mass of 80 u, at different TOFMS voltage settings the best overall result was achieved with setting #3 (see. Tab. A.1). The other parameters, mentioned in Tab. 2.2, were set according to Tab. A.2.

For the detection of bigger particles with $m > 10000\,\mathrm{u}$ the settings in Tab. A.3 yielded the best overall result. For this settings, i.e. with relatively high MCP voltage and high electron gun pulse duration, it is advisable to turn on the mass filter to avoid saturation of the MCP for small masses. Heavy saturation can accelerate the ageing process or even destroy the MCP [65].
In Appendix A.1 guidelines for the operation of the TOFMS are given as well as some notes for troubleshooting.

Chapter 3

Experimental Results

In this chapter some of the performed measurements are analysed and discussed. Mass spectra of the bare He droplet beam are analysed in Sec. 3.1, cluster beam deposition rates are determined and the two oven designs are compared in Sec. 3.2. In Sec. 3.3, 3.4 and 3.9 mass spectra of doped He droplet beams are examined. The abundance of magic numbers and the occurrence of even-odd oscillations is analysed in greater detail in Sec. 3.6. He solvation shells and the metal-water cluster compounds are analysed in Sec. 3.7 and Sec. 3.8, respectively.

All mass spectra in this chapter were recorded with the TOFMS, described and briefly characterised in Sec. 2.4.2.

3.1 Characterisation of the Helium Droplet Source

This section deals with the characterisation of the He droplet source used in this thesis ((1) in Fig. 2.1). The nozzle is cooled by a closed cycle refrigerator (see Sec. 2.1). The temperature dependence of the current-voltage-characteristic of a silicon diode ("Lake Shore cryotronics") is used to measure the nozzles temperature and a PID controller (Eurotherm) maintains a constant temperature by pulse width modulation of the voltage applied to a resistor which is mounted on the nozzle body. This way constant nozzle temperatures in the range from 6 to 20 K are accessible.

3.1.1 Nozzle Parameters

A first important property is the He flux in the droplet beam. It was measured by monitoring the He partial pressure (with the QMS) in the MC for different nozzle temperatures ($p_0 = 20\,\mathrm{bar}$). The relationship, plotted in Fig. 3.1, reveals a kink at around 10 K. There the droplet formation mechanism changes from pure gas condensation to an expansion where the He liquefies already inside the nozzle (see Sec. 1.1). This kink can also be seen in the droplet size distribution in Fig. 1.3.

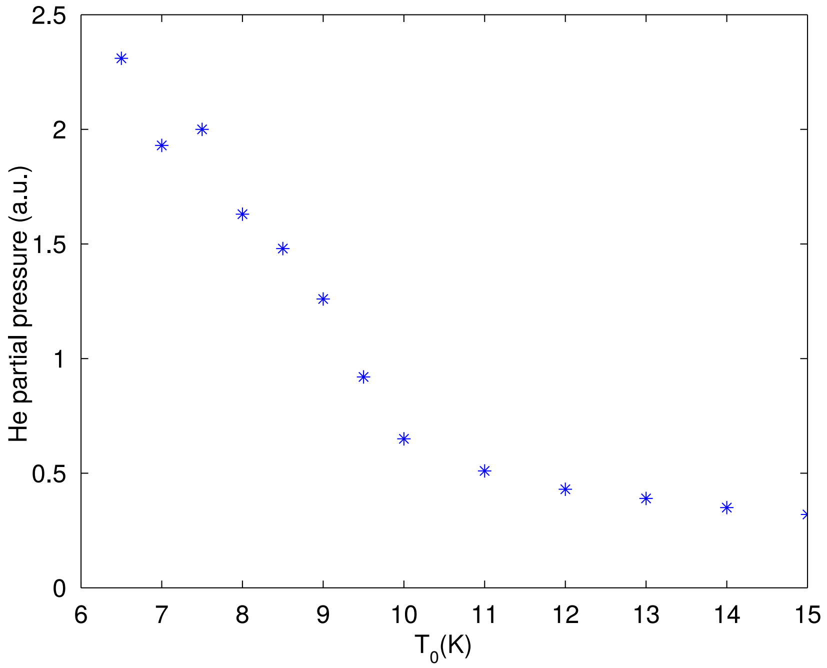

Figure 3.1: He partial pressure in the MC (measured with the QMS) for different nozzle temperatures T_0. $p_0 = 20\,\text{bar}$.

The He flux not only depends on the nozzle temperature T_0 but also on the stagnation pressure p_0. This connection was measured with the QMS aligned onto the beam axis so that the droplet beam can directly be monitored and not only the partial pressure in the MC. The measured values are given in Tab. 3.1.

Table 3.1: Ion currents in Ampere (A) as measured with the QMS at different stagnation pressures p_0. The nozzle temperature T_0 was at the respective minimum, given by the cooling capacity of the cold head.

p_0 (bar)	T_0 (K)	$m = 4\,\text{u}$	$m = 8\,\text{u}$
50	6.64	$5.8 \cdot 10^{-9}$	$1.9 \cdot 10^{-11}$
40	6.49	$4.1 \cdot 10^{-9}$	$1.5 \cdot 10^{-11}$
30	6.28	$2.4 \cdot 10^{-9}$	$9.7 \cdot 10^{-12}$
20	6.21	$1.1 \cdot 10^{-9}$	$5.1 \cdot 10^{-12}$
10	6.30	$4.0 \cdot 10^{-12}$	$1.7 \cdot 10^{-12}$

3.1.2 Mass Spectroscopy of Helium Droplets

A mass spectrum of the bare He droplet beam is plotted in Fig. 3.2. For all following mass spectra the settings, given in Tab. A.3 were used, except when stated otherwise.

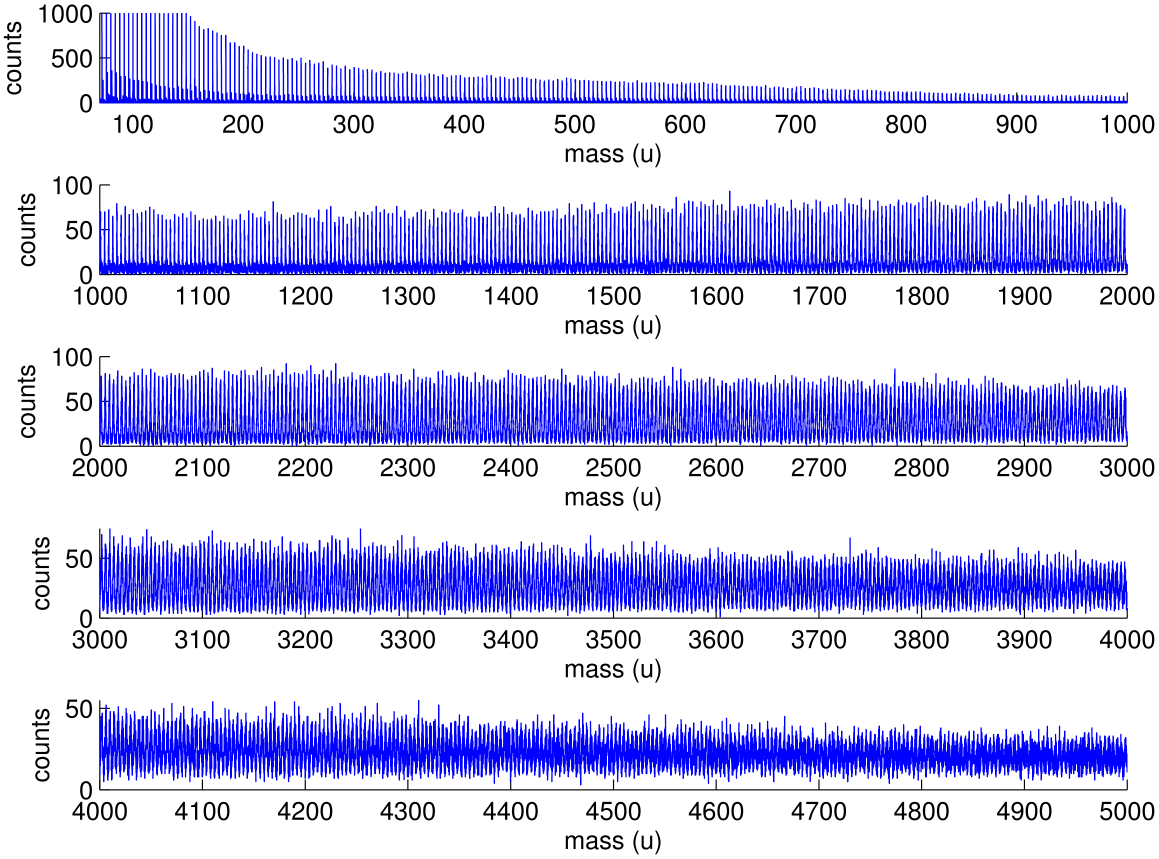

Figure 3.2: Mass spectrum of the bare He droplet beam formed under the source conditions $T_0 = 15\,\mathrm{K}$ and $p_0 = 20\,\mathrm{bar}$. The settings for the TOFMS are given in Tab. A.3.

The peaks, separated by the He mass (4.0026 u) represent the different He droplet sizes. The peak height, i.e. the frequency of occurrence, decays strongly with growing droplet size, hence it seems that small droplets are dominant in the He droplet beam. Droplets consisting of up to about 1300 He atoms are visible in the spectrum.

In Fig. 3.3 mass spectra of the He droplet beam for different nozzle temperature T_0 are depicted. The spectra show only small He droplets for low nozzle temperatures. The droplets seem to get bigger with rising nozzle temperature. To illustrate this effect, the biggest droplet for each spectrum was searched by a computer algorithm (the method is described in Appendix A.2) and plotted in Fig. 3.4.

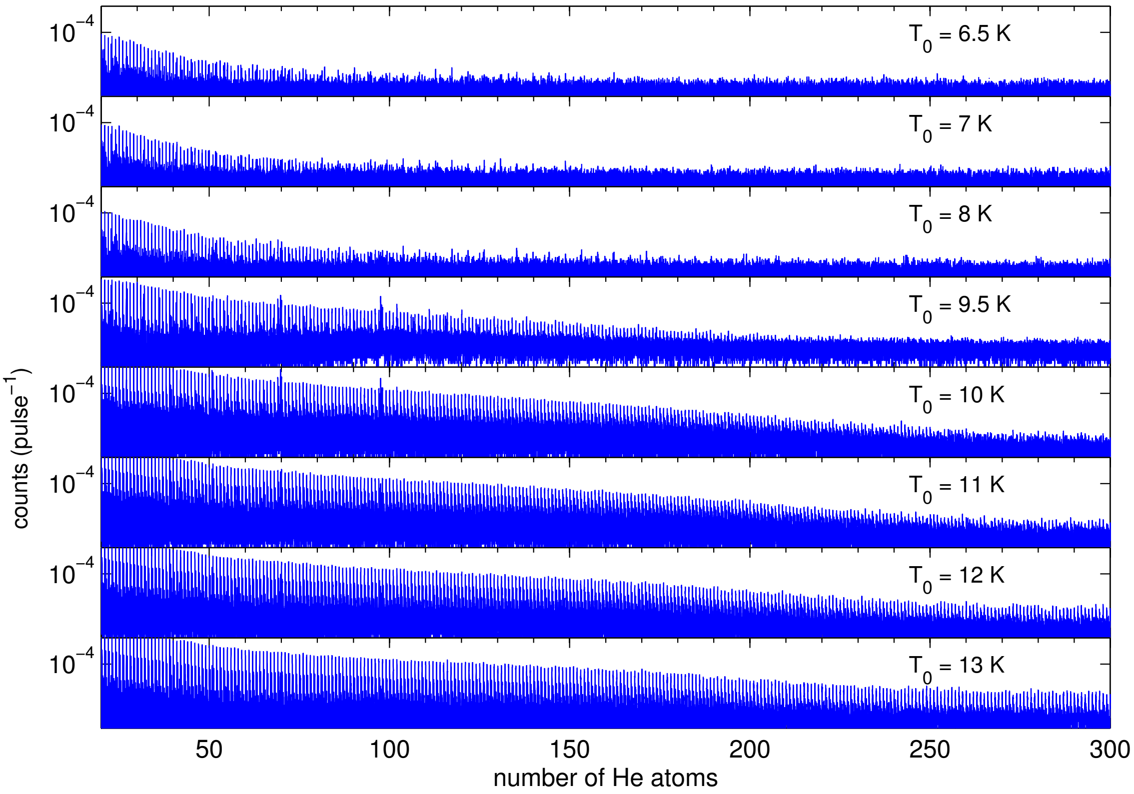

Figure 3.3: Mass spectra of the He droplet beam for different nozzle temperatures T_0, given in the inset, and $p_0 = 20\,\text{bar}$.

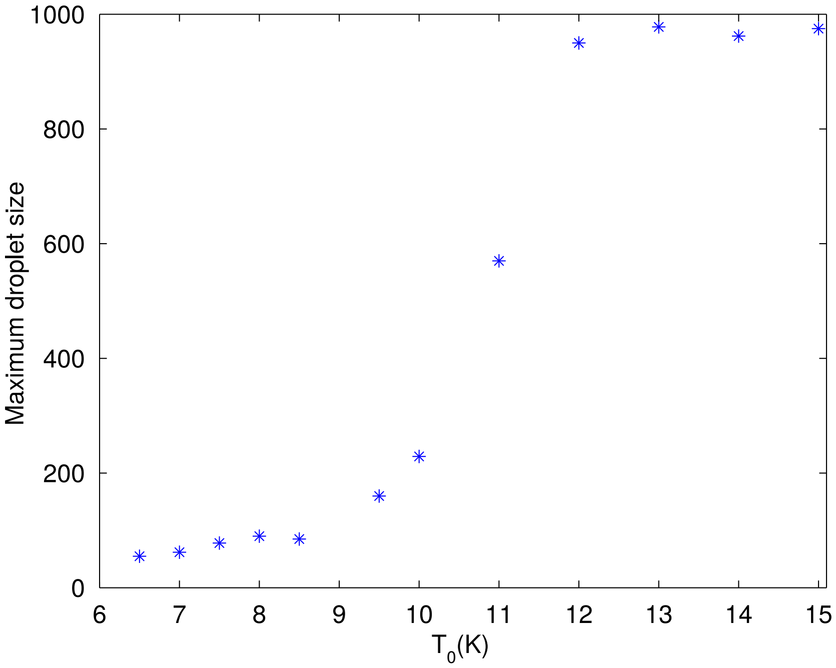

Figure 3.4: Maximum droplet size extracted from the mass spectra in Fig. 3.3. The actual droplet size is orders of magnitude higher as pointed out in Sec. 1.2.

These findings seem to be contrary to those of Gomez *et al.*, pictured in Fig. 1.3. In explaining this difference the ionisation mechanism of a He droplet as well as the size dependent sensitivity of the TOFMS plays a crucial role in explaining this contradiction. Buchenau *et al.* proposed some possible ionisation mechanisms for He droplets [72]:

- For small droplets (10^4 - 10^5 atoms), direct ionisation of the droplet is possible (see. Fig. 3.5a). If an electron with an energy higher than (29 ± 3) eV hits the droplet a He atom is ionised. The resulting He^+ forms a He_2^+ molecule (or larger). This relaxation releases about 2.3 eV of binding energy. The He atoms surrounding the ion are compressed by electrostriction and form a so called "snowball". This compression releases another 0.5 - 1 eV of energy. That equals an evaporation of about 5000 He atoms. The resulting (small) ion fragments will then be detected.
- For high electron energies (> 41 eV) the production of two excitons (He^*) in the same droplet by one electron becomes possible besides direct ionisation. The recombination of these two excited He atoms can lead to autoionisation of a He atom. The very high excess energy then leads to the evaporation of up to $7 \cdot 10^4$ He atoms. Hence small droplet ion fragments are expected. This process is sketched in Fig. 3.5b and is only valid for the ionisation of big droplets due to the big excess energy.

Thus the contrary effect, seen in Fig. 3.4, that bigger clusters are present in the mass spectra for higher nozzle temperatures can be explained by the ionisation mechanism of the He droplet and does not reflect the situation in the He_N beam. Only small droplets can be ionised directly and reach the detector of the TOFMS without fragmentation. For low temperatures (< 10 K) almost no small droplets exist in the droplet beam [26] and only fragments of the big droplets are analysed with the TOFMS (mechanism in Fig. 3.5b). When the temperature gets higher, a larger amount of small droplets is present in the He_N beam and can therefore be ionised directly (Fig. 3.5a).

A closer look into the mass spectrum of the He droplet beam especially for small droplets[1] reveals some anomalies, marked in Fig. 3.6. For the droplet abundance in Fig. 3.7 the Counts contained in each peak in the mass spectrum were summed, as described in Appendix A.2.

---

[1] From now on the term "droplet" in the context of a mass spectrum includes droplet fragments originating form the electron impact ionisation as well.

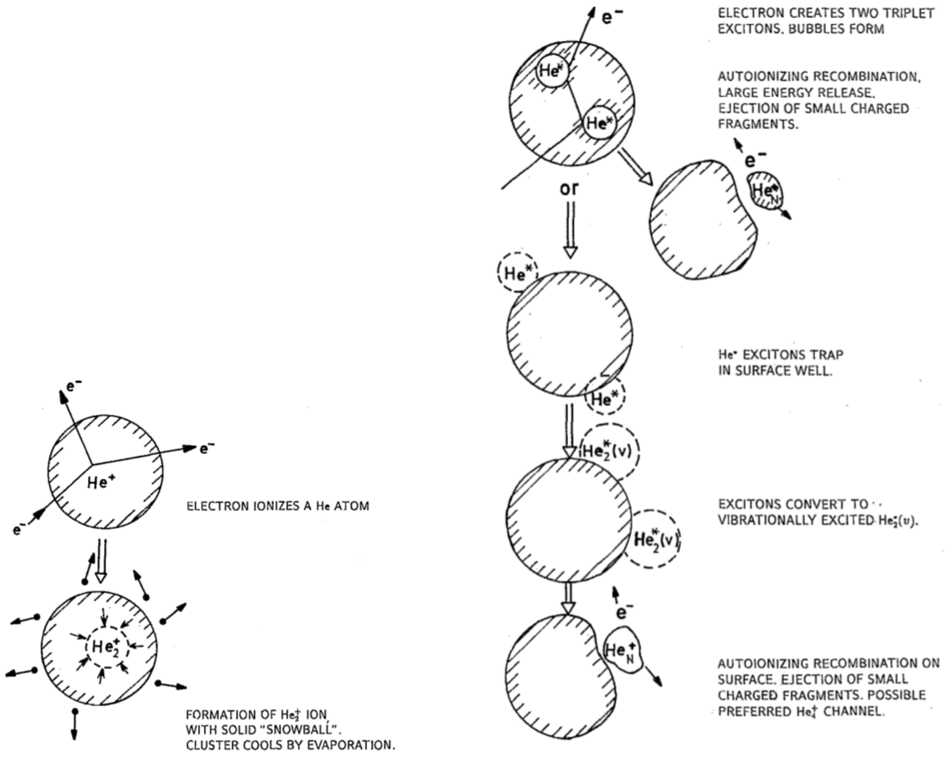

(a) (b)

Figure 3.5: Two possible processes following the impact of an electron on a neutral He droplet. Taken from Ref. [72].

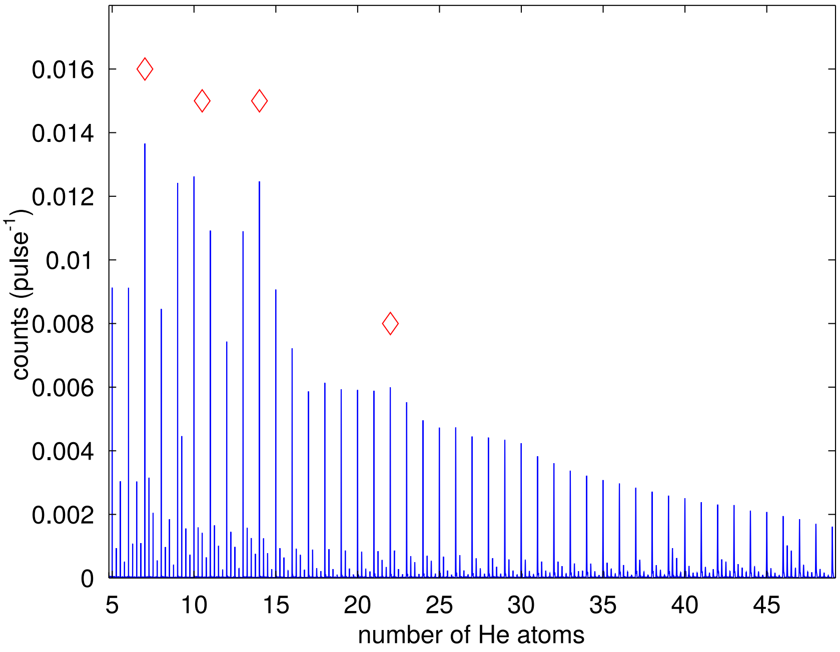

Figure 3.6: Mass spectrum of a He droplet beam at $T_0 = 10\,\mathrm{K}$ and $p_0 = 20\,\mathrm{bar}$. Magic numbers are marked with red diamonds.

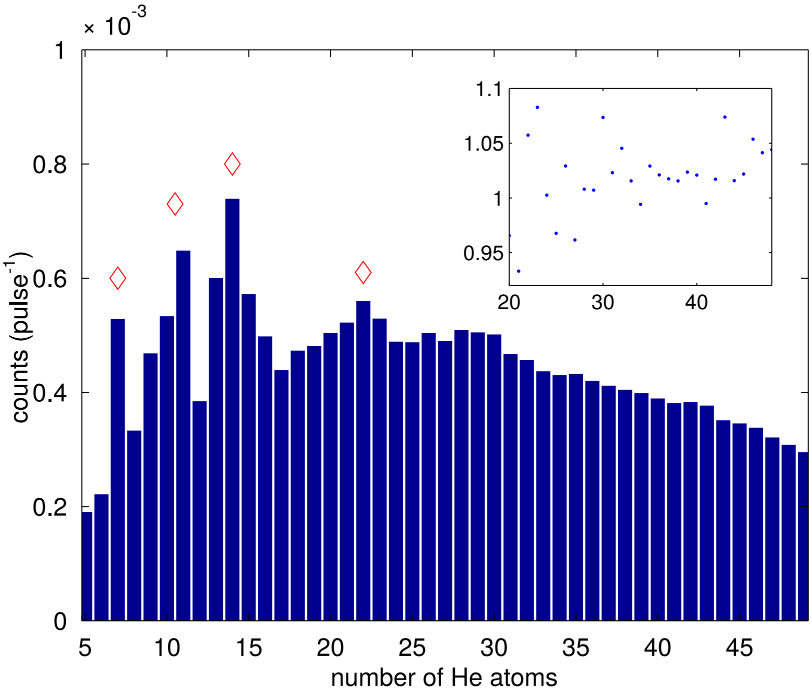

Figure 3.7: The abundance of the different cluster sizes extracted from the spectrum in Fig. 3.6. For an increased sensitivity the inset gives the ratio of adjacent peaks. The features at a cluster size of 22, 30 and 43 can be seen.

The droplets consisting of 7, 11 and 14 He atoms are outstanding upon the other sizes. There are smaller features at a size of 22 and only minor ones at around 30 and 43. These magic numbers have been reported by various groups [14, 46, 72, 73, 74, 75]. The magic numbers, reported in this thesis, are obtained after an ionisation process, hence they reflect the enhanced stability of the droplet ion and not the one of the neutral droplet, although most of these anomalies also appear in neutral He droplet beams. Brühl *et al.* found maxima in the droplet size distribution of the neutral droplet beam for droplet sizes of 10–11, 14, 22, 26–27 and 44 He atoms by diffraction of the neutral He droplets from a nanostructured transmission grating [75]. They explain the occurrence of these anomalies ”by the stabilization of an additional quantized elementary excitation state at certain sizes, which affects the partition functions and thus the equilibrium cluster populations in the formative stages of the expansion” [75]. Some groups found 5 to be a magic number too [46], which is not consistent with the performed measurements, where 5 appears more as an ”antimagic” number. Soler *et al.* showed theoretically that in case a dimer ion is formed (which is often the case when a He droplet is ionised by electron impact [43, 72] (see Fig. 3.5a)) the ”magic numbers in the mass spectra do not mirror the stability and structure of neutral clusters, but they form as a consequence of available excess energy and enhanced stability of certain positively charged clusters [76].” To give an example the magic number 14 represents a closed icosahedron (see Fig. 1.7) with a He_2^+ in the core.

3.2 Determination of Deposition Rates

For the measurements in this section the QCM, described in Sec. 2.4.1, and the QMS, mounted on the MC (see Fig. 2.1), are used.

3.2.1 Doping with the Crossed Beam Setup

In the following an exemplary deposition experiment is given. Ag clusters were synthesised in a He droplet beam formed under the source conditions $T_0 = 7.08$ - $7.05\,\mathrm{K}$ and $p_0 = 50\,\mathrm{bar}$. The crossed beam setup, pictured in Fig. 2.5, was used. The background pressures are given in Tab. 3.2.

Table 3.2: Pressures in the vacuum chambers during the experiment.

without He droplet beam
$p_{\mathrm{PU}} = 6.7 \cdot 10^{-8}\,\mathrm{mbar}$ $p_{\mathrm{DPS}} = 6.2 \cdot 10^{-9}\,\mathrm{mbar}$ $p_{\mathrm{Main}} = 4.1 \cdot 10^{-9}\,\mathrm{mbar}$
with He droplet beam ($T_0 = 7.08$, $p_0 = 50\,\mathrm{bar}$)
$p_{\mathrm{Source}} \approx 9 \cdot 10^{-5}\,\mathrm{mbar}$ $p_{\mathrm{PU}} \approx 1 \cdot 10^{-6}\,\mathrm{mbar}$ (with cooling trap filled with $\mathrm{lN_2}$) $p_{\mathrm{DPS}} \approx 2 \cdot 10^{-7}\,\mathrm{mbar}$ p_{Main} can be extracted from Tab. 3.3

Tab. 3.3 gives the tunable and monitored parameters of a typical deposition experiment. The heating current for the Ag source (see Fig. 2.5a) was controlled by the power supply ”EA-PS 9080-100” and the voltage was measured with a highly precise voltmeter (”Keithley 196 System DMM”). While changing the heating power by setting a new current value, the shutter stayed closed until a constant voltage level was reached, meaning that the measured voltage value was constant within the first three decimal places.

The deposited mass and the ^{4}He ion current (partial pressure in the MC) during the experiment are plotted over time in Fig. 3.8. With increasing time the heating current of the crucible was raised. This results in a rising vapour pressure, hence, a higher beam attenuation because the more Ag atoms are picked up the more He atoms evaporate in the pickup region. The vapour pressure for Ag and Au as a function of temperature is plotted in Fig. 3.9.

In Fig. 3.10 the deposition rate is plotted over the beam attenuation to illustrate the beam deflection due to momentum transfer. The deposition rates were determined from Fig. 3.8 while the shutter was opened (the constant slope in the shaded regions) and are given in Tab. 3.3. For low beam attenuations $< 30\,\%$ the deposition rate rises

Table 3.3: Parameters tuned and monitored during a typical deposition experiment. Ag clusters are synthesised in a He droplet beam ($T_0 = 7.08$ - $7.05\,\mathrm{K}$ and $p_0 = 50\,\mathrm{bar}$). The column "sector" refers to the gray areas in Fig. 3.8.

I_{Ag},U_{Ag},P_{Ag}	current, voltage and heating power ($P = U \cdot I$) applied to the crucible
p_{main}	pressure in the MC measured with an ionization gauge
A_p	attenuation calculated from the absolute pressure decrease $A_p = (1 - \frac{p_{\mathrm{main,opened}}}{p_{\mathrm{main,closed}}}) \cdot 100\,\%$
I_{He}	ion current for the mass 4 u measured with the QMS in the MC
$A_{\mathrm{I_{He}}}$	attenuation calculated from the He ion current decrease $A_{\mathrm{I_{He}}} = (1 - \frac{I_{\mathrm{He,opened}}}{I_{\mathrm{He,closed}}}) \cdot 100\,\%$
dep. rate	mass deposition rate measured with the QCM in the MC

sector	shutter	I_{Ag}	U_{Ag}	P_{Ag}	p_{main}	A_p	I_{He}	$A_{\mathrm{I_{He}}}$	dep. rate
		A	V	W	10^{-8} mbar	%	10^{-9} A	%	$10^{-5}\,\frac{\mu\mathrm{g}}{\mathrm{cm}^2\mathrm{s}}$
1	closed opened	22.5	6.42	145	6.0 5.5	8	2.14 1.98	7.5	5.0
2	closed opened	23.0	6.79	156	6.0 5.3	12	2.12 1.95	8	7.5
3	closed opened	23.5	7.08	166	5.9 5.2	13	2.18 1.91	12	9.0
4	closed opened	24.0	7.34	176	6.0 4.4	27	2.20 1.62	26	18.0
5	closed opened	24.5	7.64	187	5.9 3.8	36	2.22 1.37	38	12.0
6	closed opened	25.0	7.91	198	5.8 3.4	41	2.10 1.12	47	5.0
7	closed opened	25.5	8.19	209	5.8 2.7	53	2.05 0.81	60	0.5

almost linearly. Although the beam is depleted by the pickup of Ag atoms (the pickup of each Ag atom leads to the evaporation of about 5000 He atoms) even more, the deposition rate is dropping at some point. At a beam attenuation over about 60 % no deposition is measured any more. The doped He droplet beam does not impact on the QCM any more because of the beam deflection due to momentum transfer.

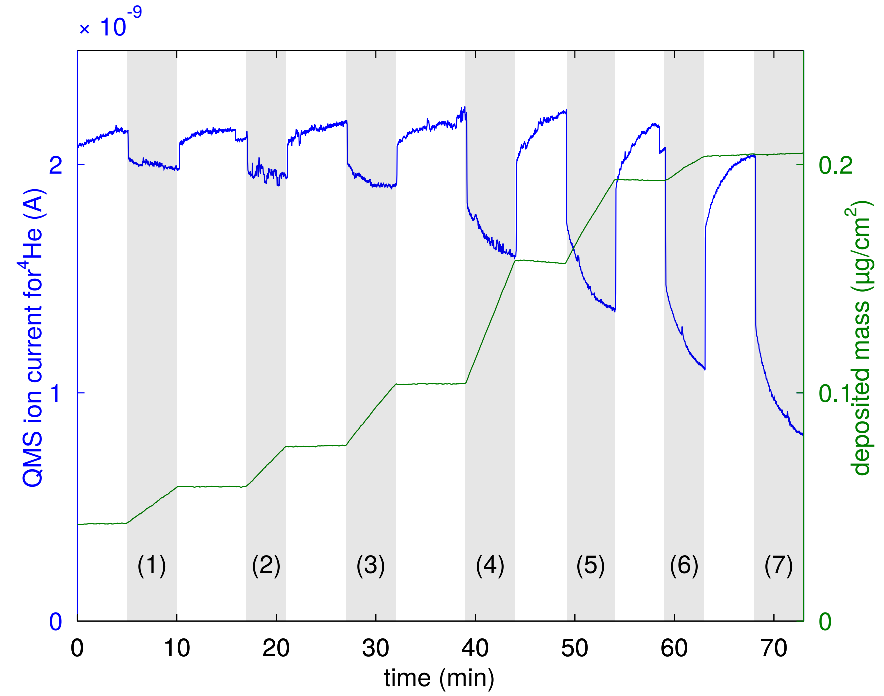

Figure 3.8: Deposited mass and attenuation of the He droplet beam while synthesising Ag clusters. The blue line represents the ion current for the mass 4 u measured with the QMS. The green line shows the deposited mass as measured with the QCM. The values corresponding to the numbered sectors can be found in Tab. 3.3. Only within these shaded areas the shutter (see Fig. 2.5c) was opened and a mass transport by the He droplet beam was possible.

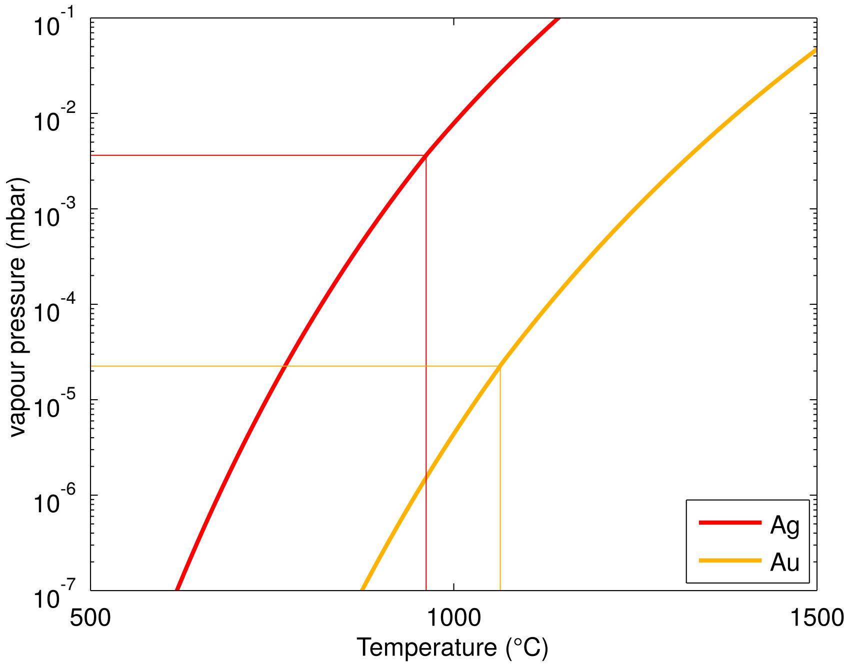

Figure 3.9: Vapour pressures for Ag and Au as a function of temperature. The respective melting points are marked. Data from [77].

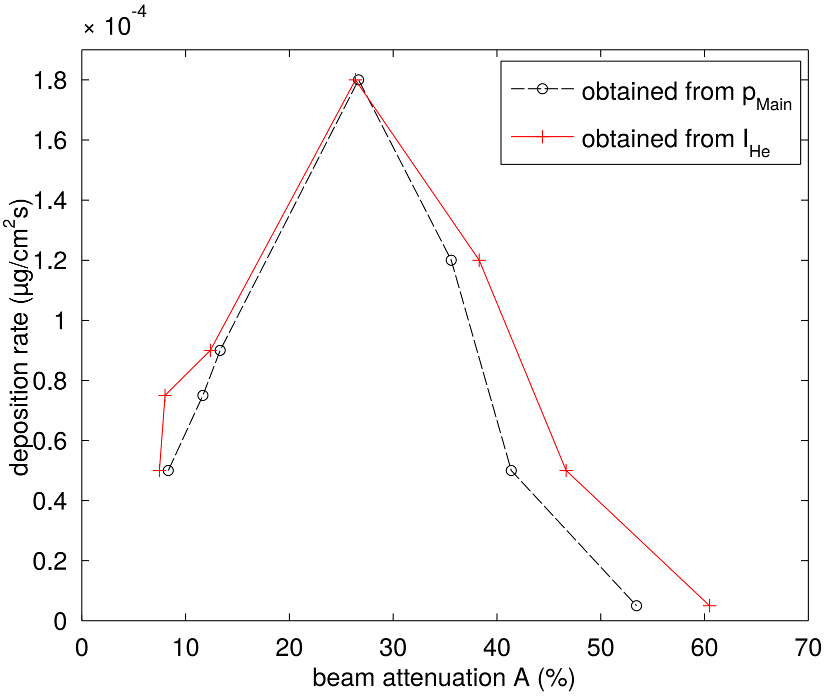

Figure 3.10: Plot of the deposition rate over the He beam attenuation for the deposition of Ag clusters in the crossed beam setup. The red crosses and black circles represent the beam attenuation calculated from the QMS ion current and from the pressure in the MC, respectively. The corresponding values can be found in Tab. 3.3. The datapoints are connected to guide the eye.

3.2.2 Doping with the Symmetric Oven Design

If the same measurement as in Sec. 2.2.1 is done for the symmetric oven design (see Fig. 2.6) the resulting picture is different as shown by Fig 3.11. In contrast to the crossed beam setup the linear behaviour between deposition rate and beam attenuation continues to beam attenuations of over 70 %. During the experiment the nozzle conditions were held constant at $T_0 = 9\,\mathrm{K}$ and $p_0 = 20\,\mathrm{bar}$.

In contrast to the crossed beam setup, the symmetric design features an effusive atom beam at sufficiently high vapour pressures, i.e. oven temperatures, which is plotted in Fig. 3.12. Additionally the shutter concept, as employed in the crossed beam setup, cannot be applied here.

In Fig. 3.13a the deposition rate is plotted as a function of the Au oven temperature. The correlation is analogous to the temperature dependence of the vapour pressure, pictured in Fig. 3.9. The higher the vapour pressure the more likely it is for each He droplet to collide with multiple atoms. Furthermore a correlation between the nozzle temperature T_0 and the deposition rate is observable. Although the He flux rises with lower temperature (see e.g. Sec. 3.1) the deposition rate drops for $T_0 < 9.5\,\mathrm{K}$. The explanation lies in the droplet formation mechanism and the pickup process. For low nozzle temperatures bigger droplets form. Although the absolute number of He atoms

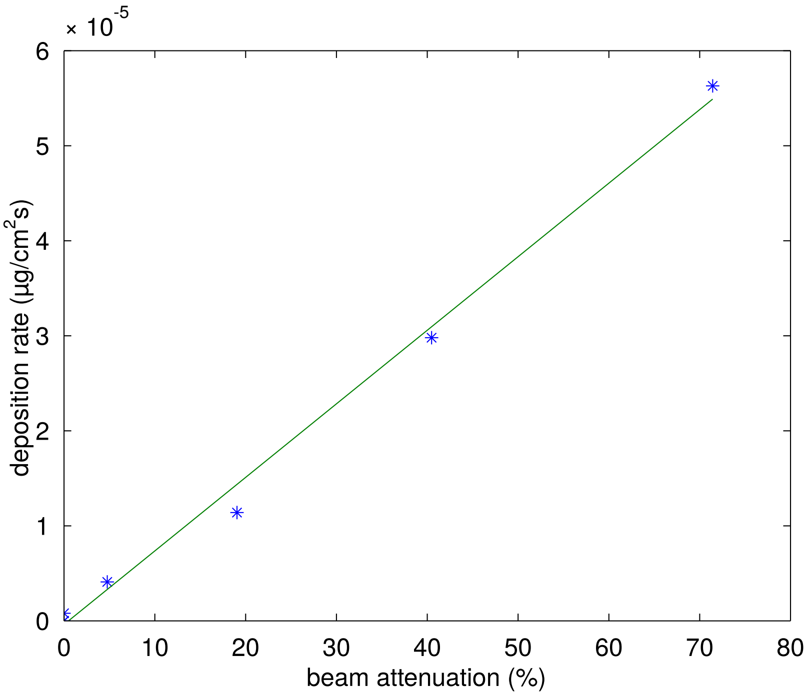

Figure 3.11: Deposition rate as a function of the beam attenuation for the deposition of Au clusters with the symmetric oven design. The linear model between the two variables fits well.

rises with lower nozzle temperatures the number of droplets, the droplet flow rate, decreases [61]. That implies that the overall droplet cross-section ($\propto N^{2/3}$), which is proportional to the pickup probability [11], has a maximum at a certain nozzle temperature.

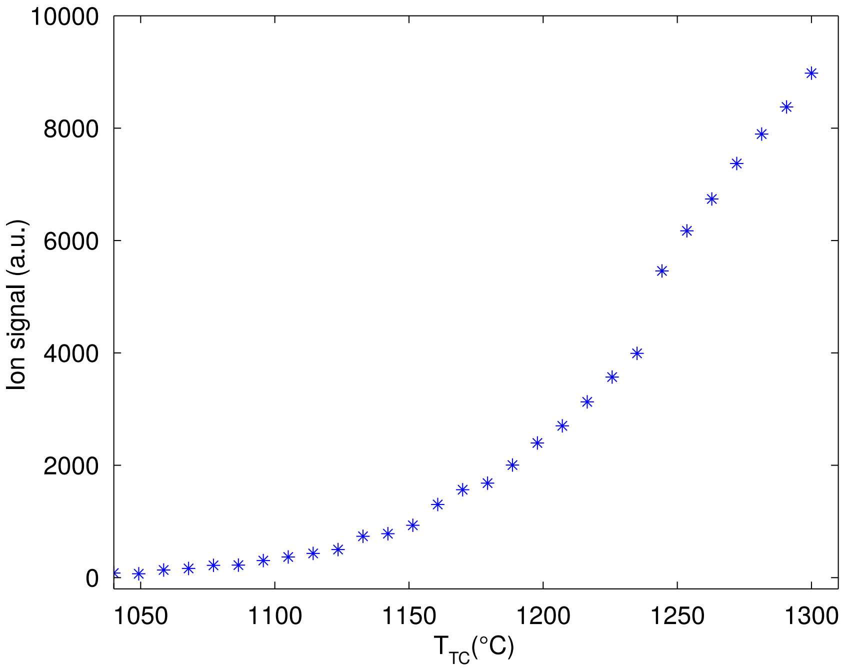

Figure 3.12: Measurement of the effusive regime of the Au oven by monitoring the mass 197 u with the TOFMS while raising the oven-temperature. The relative uncertainty of the temperature was estimated to be ±20 °C.

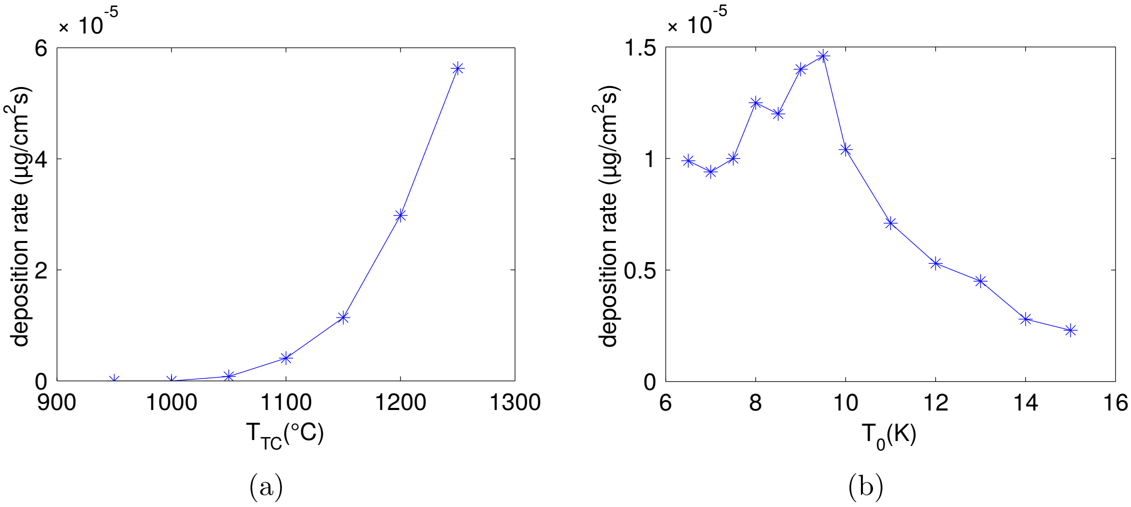

Figure 3.13: Dependence of the deposition rate on the Au oven temperature T_{TC} and on the nozzle temperature T_0.

3.2.3 Comparison of the two Oven Designs

With a similar crossed beam oven design as described in Sec. 2.2.1, but with the QCM closer to the PU-region as in the current setup, deposition rates of about one order of magnitude higher were reported [57]. In addition, a comparison of Fig. 3.10 and 3.11 fortifies the beam deflection theory presented in Sec. 3.2.1. The on average vanishing momentum transfer onto the droplet is a very big advantage of the 2-crucible-design. Otherwise heavy doping of the droplet beam (as needed in Sec. 3.10) would not be possible.

3.3 Mass Spectroscopy of Silver Clusters

In Fig. 3.14 the TOF mass spectrum for an Ag doped He droplet beam is plotted. The doping was done with the initial design of the crossed beam setup including a thermocouple in the crucible. The biggest clusters in the spectrum have a mass of slightly under 7000 u which equals the mass of 65 Ag atoms. To build such a cluster the initial He droplet has to consist of considerably more than 300.000 He atoms, as this number of He atoms evaporates due to subsequent release of Ag-Ag binding energy ($\approx 3\,\mathrm{eV}$). The spectrum originating from the undoped He droplets can be seen up to a mass of about 500 u.

The even-odd effect is particularly well illustrated for small clusters. Here the clusters consisting of an odd number of atoms appear more likely. This effect is analysed in detail in Sec. 3.6.1. Since the He droplets can pick up every substance they collide with, as pointed out in Sec. 1.3, it is not surprising that water is picked up also. In the upper plot in Fig. 3.14 every peak, originating from the bare $\mathrm{Ag_n}$ cluster, is followed by peaks originating from the pickup of water ($\mathrm{Ag_n(H_2O)_m}$, $m_{\mathrm{H_2O}} = 18\,\mathrm{u}$). This is shown in detail in Fig. 3.15 for the $\mathrm{Ag_8}$ cluster.

For the bare Ag cluster the "fine structure" reveals some binomially distributed peaks around a mass of 864 u, which originate from the different possibilities to mix the two naturally present Ag isotopes $^{107}\mathrm{Ag}$ and $^{109}\mathrm{Ag}$, which are almost equally common [78]. The peaks in between originate from an additional hydrogen atom. Water, picked up by the He droplet, can manifest as OH (17 u), $\mathrm{H_2O}$ (18 u) and $\mathrm{H_3O}$ (19 u) in the mass spectrum (see also Sec. 3.8). Hence, all these masses (17 u, 18 u and 19 u) added to the peaks stemming from the neat Ag cluster (around 856 u - 872 u) result in additional peaks in the mass spectrum (peaks around $m = 881$). The same applies to multiple water pickups (peaks around $m = 898$, $m = 916$ and so on). The dissociation of the water molecule due to the ionisation process manifests in a blur of the $\mathrm{Ag}_n(\mathrm{H_2O})_m$ peaks. The effects, resulting from the addition of water to the metal cluster, are analysed in more detail in Sec. 3.8.

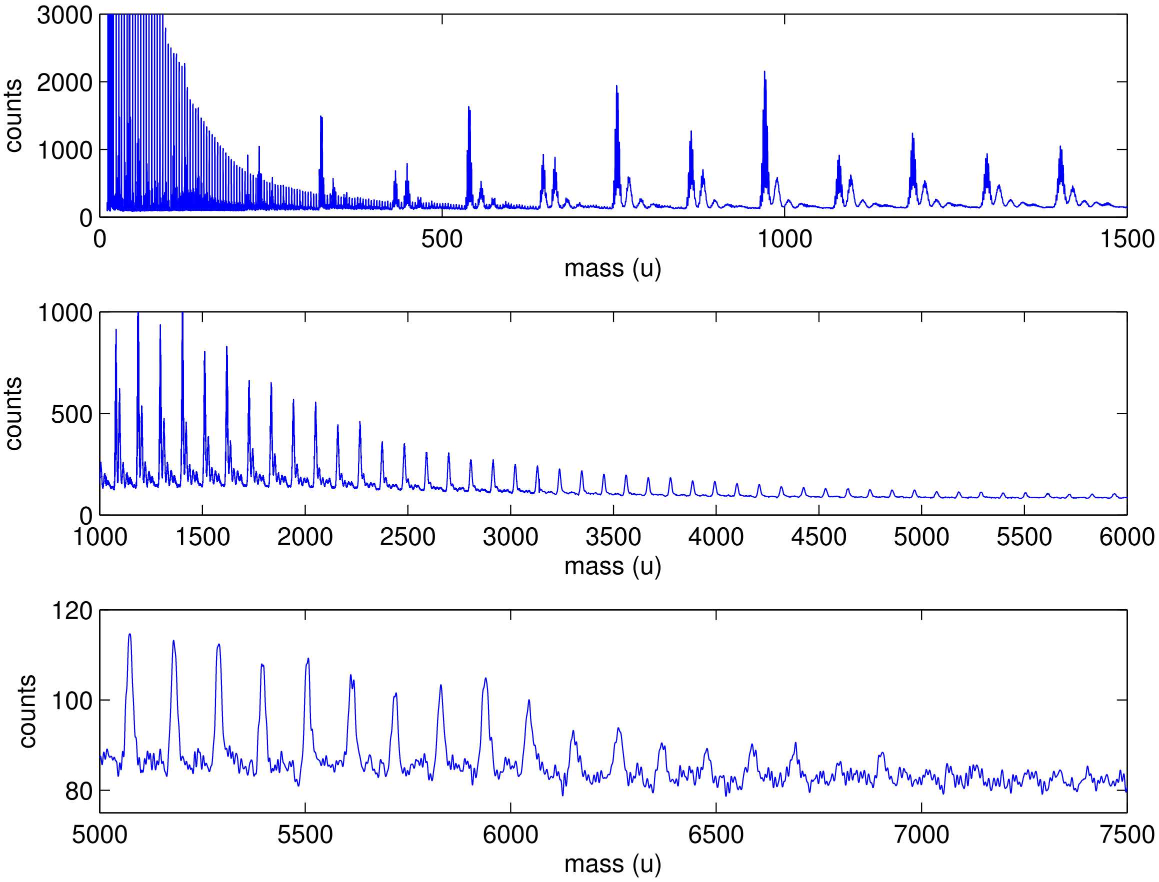

Figure 3.14: TOF mass spectrum for an Ag-doped He droplet beam. The Ag oven was heated at $T_{\mathrm{TC}} = 1040\,^{\circ}\mathrm{C}$; with the source conditions $T_0 = 9.5\,\mathrm{K}$ and $p_0 = 20\,\mathrm{bar}$. The data up to mass 3000 is smoothed with a moving average filter. For bigger masses a Dirichlet-filter was applied. The used TOFMS parameter-set is listed in Tab. A.2.

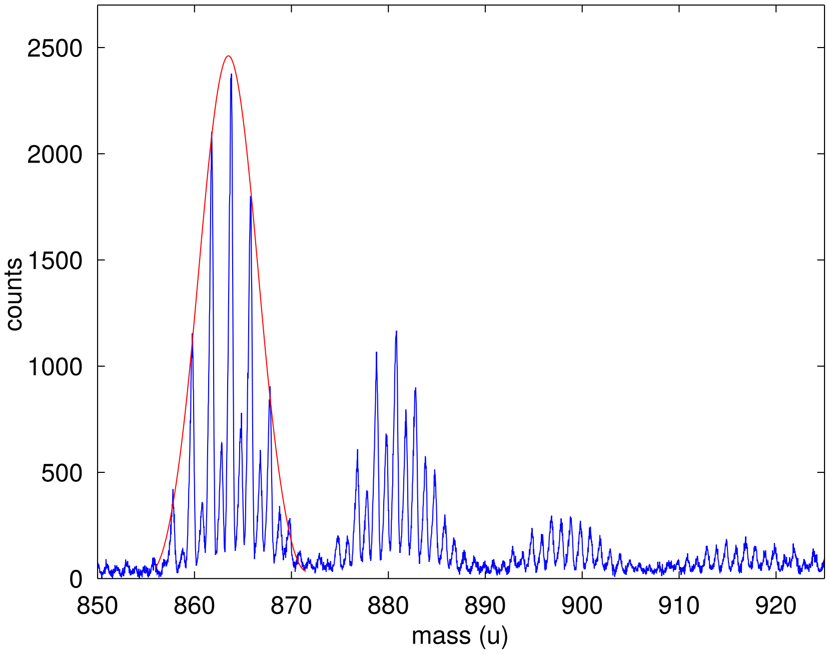

Figure 3.15: Detail from Fig. 3.14, the Ag_8 cluster. On the left the neat Ag_8 cluster with its different masses (all possible combinations for the two isotopes ^{107}Ag and ^{109}Ag) is visible. The red line indicates the binomial distribution of the isotope compounds. To the right every group of peaks correspond to an additional water molecule.

3.3.1 Mass Spectra for Different Oven Temperatures

For all following experiments with Ag a symmetric oven design was used. As seen in Sec. 3.2, the Ag mass transport through the He droplet beam is dependent on the oven temperature and the source conditions.

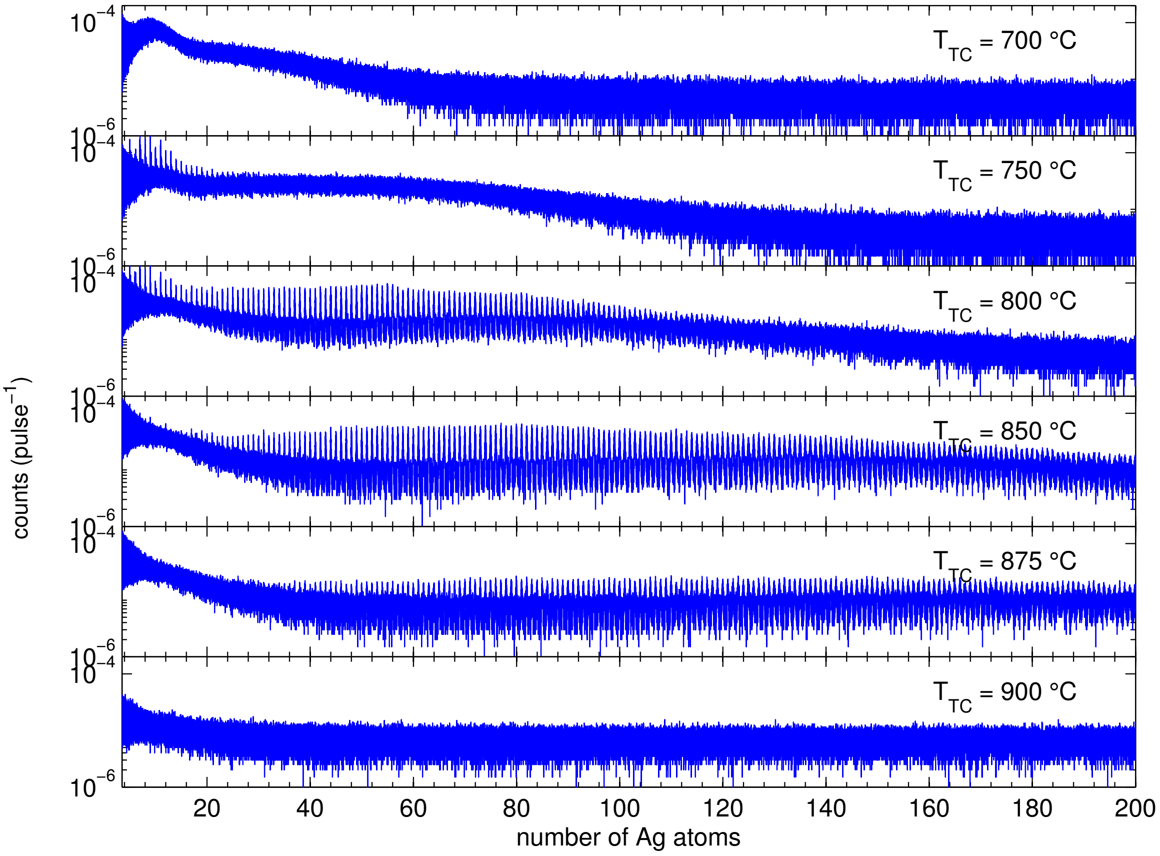

Figure 3.16: Mass spectra obtained for an Ag doped He droplet beam ($T_0 = 9\,\mathrm{K}$ and $p_0 = 20\,\mathrm{bar}$, $\langle N_{\mathrm{He}}\rangle \approx 1.8 \cdot 10^6$) for different oven temperatures indicated by respective insets.

Fig. 3.16 compares the mass spectra for different oven temperatures at constant source conditions. For low temperatures ($T_{\mathrm{TC}} = 700\,°\mathrm{C}$) the Ag vapour density is low, hence the probability for Ag pickup is low. Only very small Ag clusters are visible in the spectrum. The higher the temperature gets, the bigger the clusters in the mass spectra become. At $T_{\mathrm{TC}} = 900\,°\mathrm{C}$ the vapour pressure is high enough to destroy all droplets and only an effusive Ag beam is detected. Boatwright *et al.* observed a similar correlation for nickel doped He droplets [3].

For a better visibility of this effect, the counts contained in each Ag peak were calculated with the method described in Appendix A.2 and plotted in Fig. 3.17. For moderate oven temperatures (800 - 850 °C) the Ag cluster size distribution is visible, which is analysed in Sec. 3.5. The kinks in the abundance pattern of the cluster sizes are analysed in more detail in Sec. 3.6. The maximum cluster size for each temperature is extracted from Fig 3.17 and plotted in Fig. 3.18. A big dependence on the oven temperature can be seen around 800 °C. The biggest clusters are present between 850 and 875 °C.

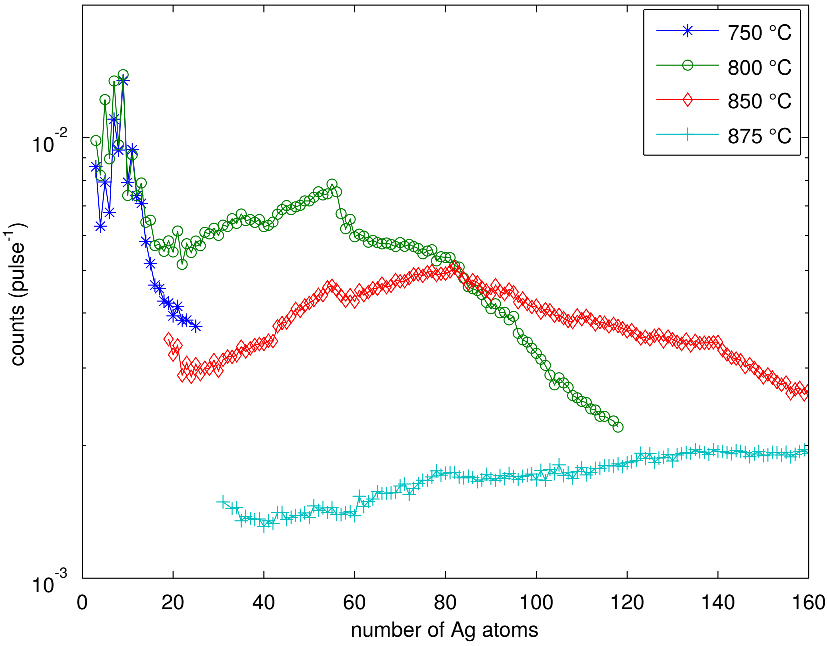

Figure 3.17: Counts contained in each Ag peak extracted from Fig. 3.16.

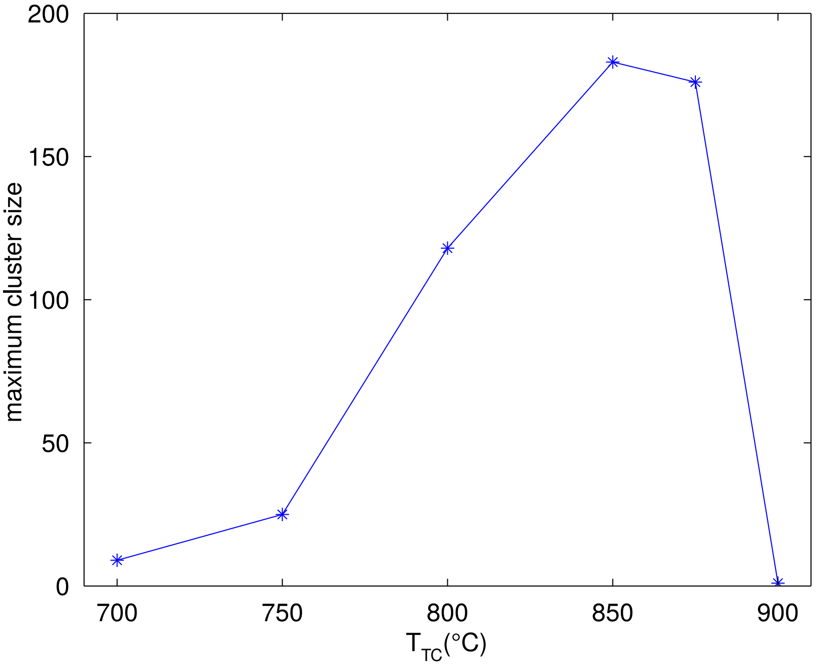

Figure 3.18: Maximum Ag cluster size for different oven temperatures ($T_0 = 9\,\mathrm{K}$ and $p_0 = 20\,\mathrm{bar}$) in the TOF mass spectrum. The datapoints are connected to guide the eye.

As stated before, the cluster size distribution in Fig. 3.17 and the maximum cluster size plotted in Fig. 3.18 do not necessarily have to mirror the real cluster sizes in the neutral droplet, since the ionisation process can cause fragmentation of the cluster before detection. Further the size dependent sensitivity of the TOFMS underrepresents large cluster sizes.

3.3.2 Mass Spectra for Different Nozzle Temperatures

In Fig. 3.19 the mass spectra of an Ag doped He droplet beam are plotted for different nozzle temperatures T_0. The temperature of the Ag oven was held constant at $T_{\mathrm{TC}} = 850\,°\mathrm{C}$. The number of He atoms in the droplets for each nozzle temperature is given in Tab. A.5.

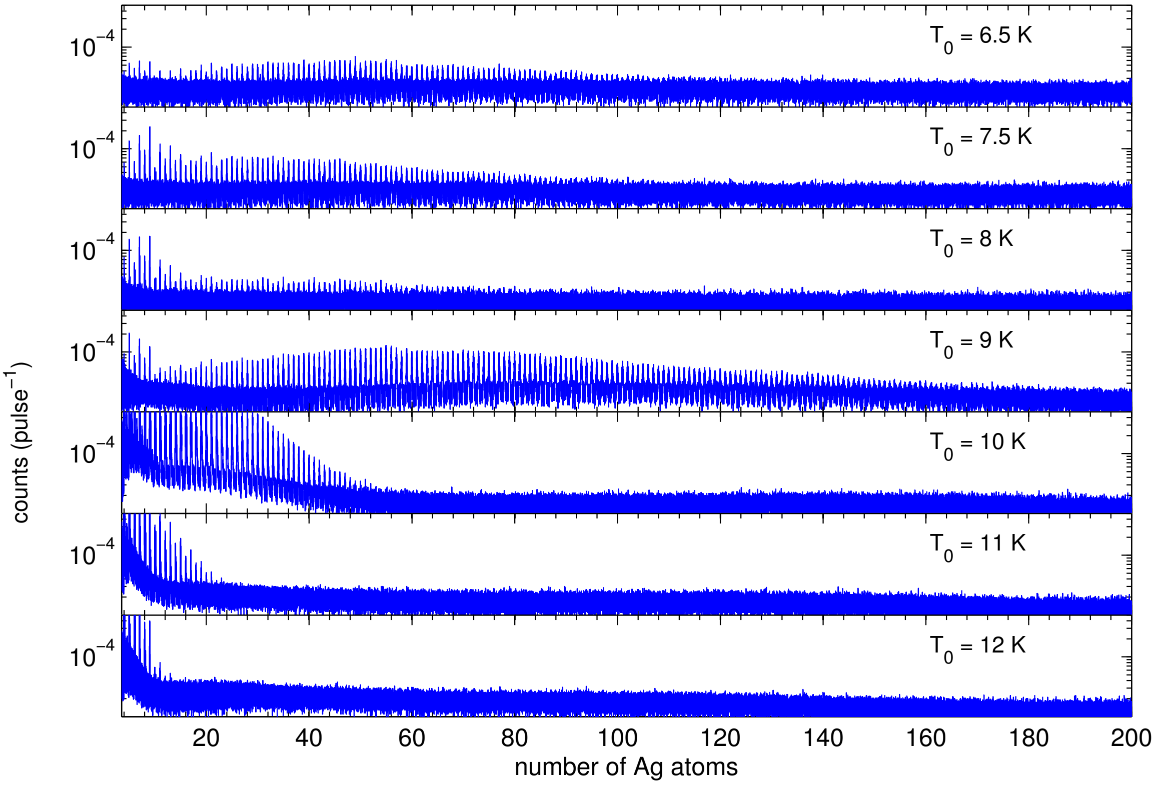

Figure 3.19: Mass spectra obtained for an Ag doped He droplet beam at different nozzle temperatures T_0 and $p_0 = 20\,\mathrm{bar}$ at a constant Ag oven temperature $T_{\mathrm{TC}} = 850\,°\mathrm{C}$.

For decreasing nozzle temperatures the clusters get larger. For temperatures from 16 to 10 K the increase in the cluster size is evident and was discussed before. The non-trivial behaviour for even lower nozzle temperatures is discussed in the following.

As measured by Gomez *et al.* [26] the mean droplet size increases by more than 1 order of magnitude between 10 and 9 K and continues increasing for lower temperatures, but with a slower rate (Tab. A.5 and Fig. 1.3). Besides the change in the droplet size distribution, the total flux of He rises by about a factor of 4 when cooling the nozzle from 10 to 7 K (see Fig. 3.1). This means that while the number of He atoms in the beam increases, the number of droplets in the beam decreases dramatically[2]. This behaviour is reflected in the mass spectra of bare He droplets (shown in Fig. 3.3) where below 9 K the mass spectra hardly change with the nozzle temperature, because only fragments are visible, as discussed in the respective Sec. 3.1.2.

In the experiments with doped helium droplets similar effects are expected. When analysing the obtained spectra, the decreasing sensitivity of the TOFMS for big masses as well as the lower ionization cross section for clusters in larger droplets have to be kept in mind. The mass spectra shown in Fig. 3.19 and the peak-intensity distribution in Fig. 3.20 nicely show all the above mentioned characteristics. Between 10 and 9 K the observed cluster sizes strongly increase, because of the increasing droplet size, while the intensity decreases, because of the less likely ionisation of the dopant in the bigger droplets. For the spectrum at 8 K the mean Ag_n cluster size has already shifted to sizes that are no longer detectable with the TOFMS ($\langle n \rangle \approx 700$ according to Eq. 1.4). Only the low-mass-tail of the cluster size distribution is barely visible because the overall intensity is too low ($n_{\max} \approx 60$).

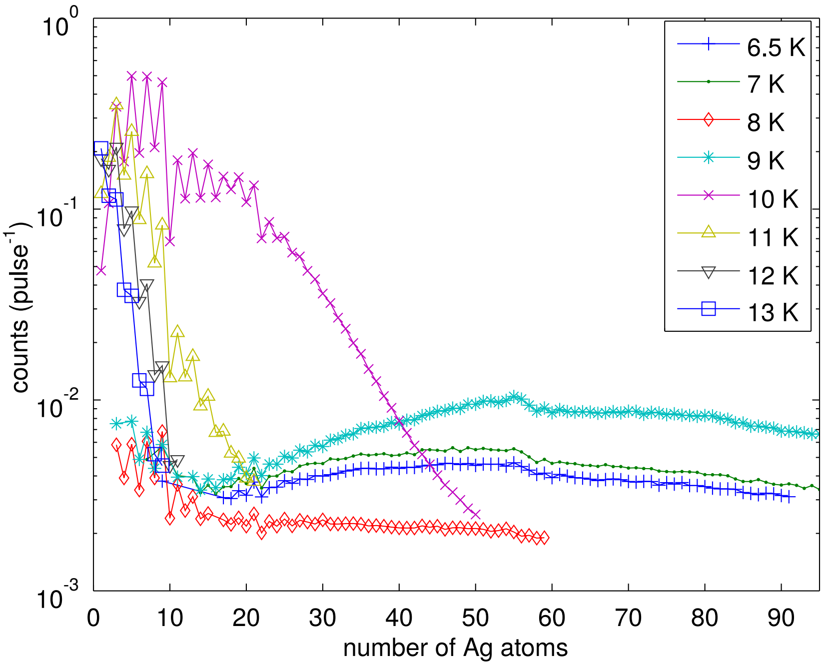

Figure 3.20: Counts contained in each Ag peak extracted from Fig. 3.19. The datapoints are connected to guide the eye. The big fluctuations for small clusters is analysed in detail later on.

At nozzle temperatures below 8 K, i.e. mean He_N sizes in the order of $\langle N \rangle = 10^7$, Ag_n clusters up to almost $n = 100$ start to reappear in the spectra. As stated by Loginov *et al.* the cluster aggregation scenario changes for droplets larger than about

---

[2] This relationship is plotted in Fig. 11 in Ref. [61]

$\langle N \rangle = 10^6$ He atoms from single centre to multi centre growth [79], which corresponds to a nozzle temperature between 8 and 9 K. This is fortified by experimental photoabsorption spectra which show the same characteristic as simulated spectra of cluster-cluster aggregates. In the experiments within this thesis this could mean that separated clusters are aggregated and still exist in the same droplet when the beam passes the ionisation zone of the TOFMS for nozzle temperature below 8 K.

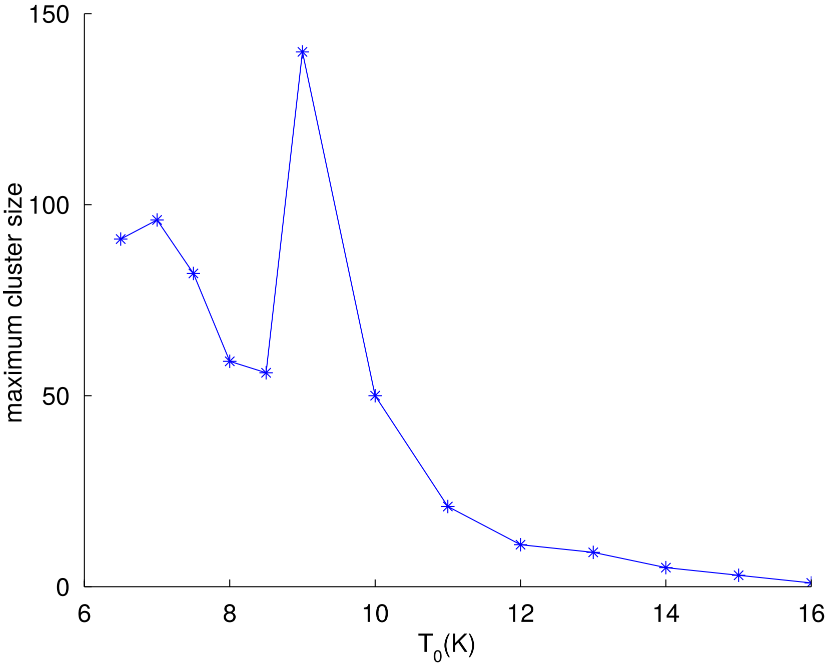

Figure 3.21: Maximum Ag cluster size for different nozzle temperatures ($p_0 = 20$ bar). The datapoints are connected to guide the eye.

In Fig. 3.21 the largest observed cluster sizes for different nozzle temperatures are displayed. As described above, only clusters up to a certain size can be detected properly with the TOFMS. The drastic decrease in the number of droplets in the beam, i.e. drastic decrease in intensity, at lower temperature leads to a decrease of the observed maximum cluster size ($T_0 < 9$ K). The reappearance of bigger clusters at even lower temperatures ($T_0 < 8$ K) can be attributed to the multi-centre growth process inside the droplet.

As the droplets get bigger for lower nozzle temperature their cross-section increases like $N^{2/3}$. For the temperature range from 8 to 7 K the mean droplet size increases about a factor of 2 (see Tab. A.5) which entails a rise in the pickup cross-section of about a factor of 1.6 and should lead to an increase in the mean cluster size of about the same factor. This is indeed the case, as can be seen in Fig. 3.21. The discussed temperature range lies well in the multi-centre growth regime [79].

The fact that for low nozzle temperatures, like $T_0 = 6.5$ K, still a reasonable amount of Ag clusters can be ionised stands in contradiction to the short mean free path for electrons in the droplet stated by Ellis *et al.* [41] (2.59 nm for 40 eV, as mentioned in Sec. 1.5.1) but is more consistent with estimation of Gomez *et al.* [26] (up to 180 nm).

3.4 Mass Spectroscopy of Gold Clusters

Au is, like Ag, a group-11 element. The electronic configuration is similar, as both elements have a valence electron in the s-orbital. Thus the behaviour of Au as a dopant in a He droplet is expected to be similar to Ag. Fig. 3.22 shows the appearance of Au_1, Au_2 and the Au_5 cluster as a function of temperature. Clearly the bigger clusters are more likely to be found at higher oven temperature, because of the higher probability for multiple pickup after Eq. 1.1. This also manifests in the drop of the He_2 signal, which is an indicator of the droplet beams intensity.

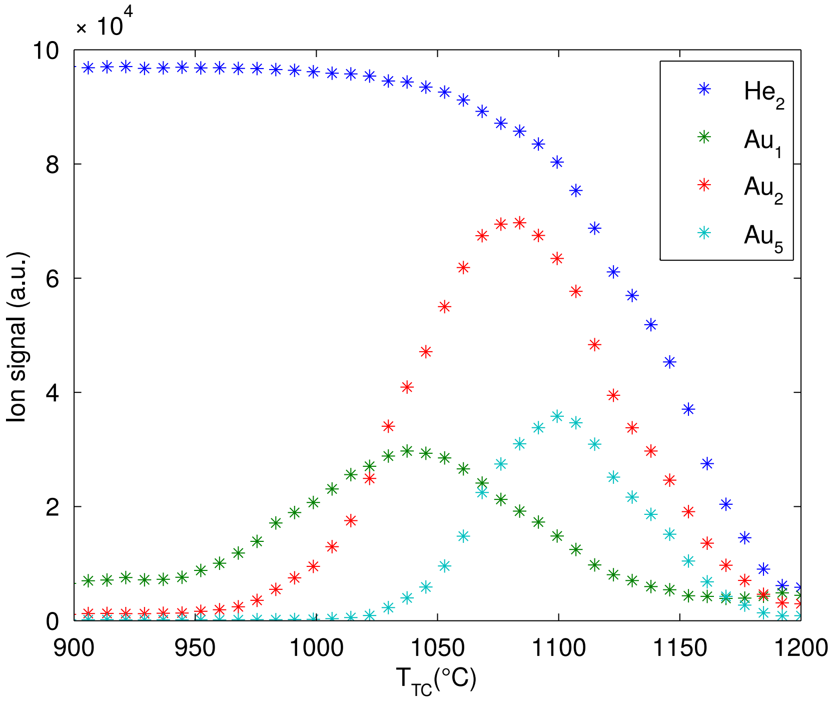

Figure 3.22: TOF ion signals of different Au clusters as a function of the oven temperature. The He_2- Signal is saturated for temperatures $\lesssim 1100\,°C$, hence the beam attenuation is not significant. The temperature has a relative uncertainty of $\pm 20\,°C$. The source conditions were $T_0 = 10\,K$ and $p_0 = 20\,bar$.

3.4.1 Mass Spectra for Different Oven Temperatures

In Fig. 3.23 the mass spectra of an Au doped He droplet beam are plotted for different oven temperatures. The picture is the same as for Ag. The higher the oven temperature, the bigger the clusters in the mass spectra get.

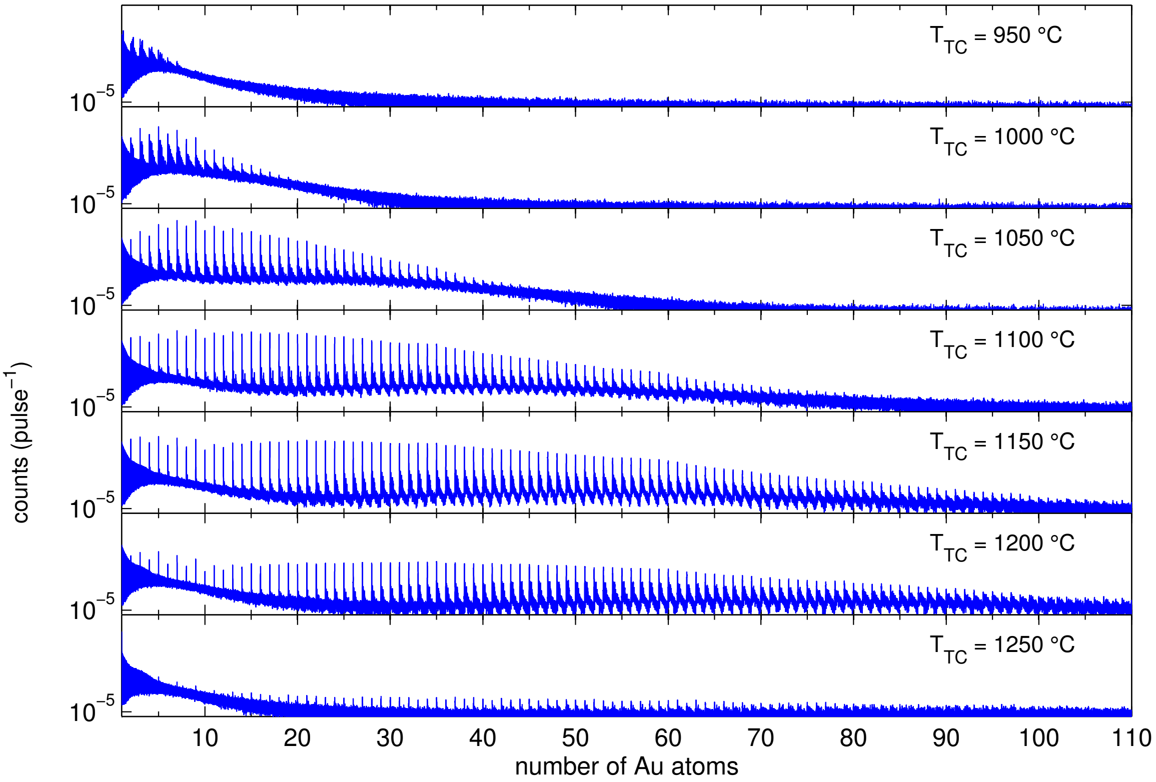

Figure 3.23: Mass spectra of an Au doped He droplet beam ($T_0 = 9\,\mathrm{K}$ and $p_0 = 20\,\mathrm{bar}$, $\langle N_{\mathrm{He}} \rangle \approx 1.8 \cdot 10^6$) for different oven temperatures.

The size distribution (Fig. 3.24) of the Au clusters show the same behaviour as for Ag clusters. The higher the temperature, the wider the mean cluster size is shifted to the right, i.e. bigger clusters. The same goes for the maximum visible cluster sizes in Fig. 3.25, although the overall cluster size is smaller for Au clusters compared to Ag, which can be attributed to the higher atomic weight of Au and the sensitivity function of the TOFMS.

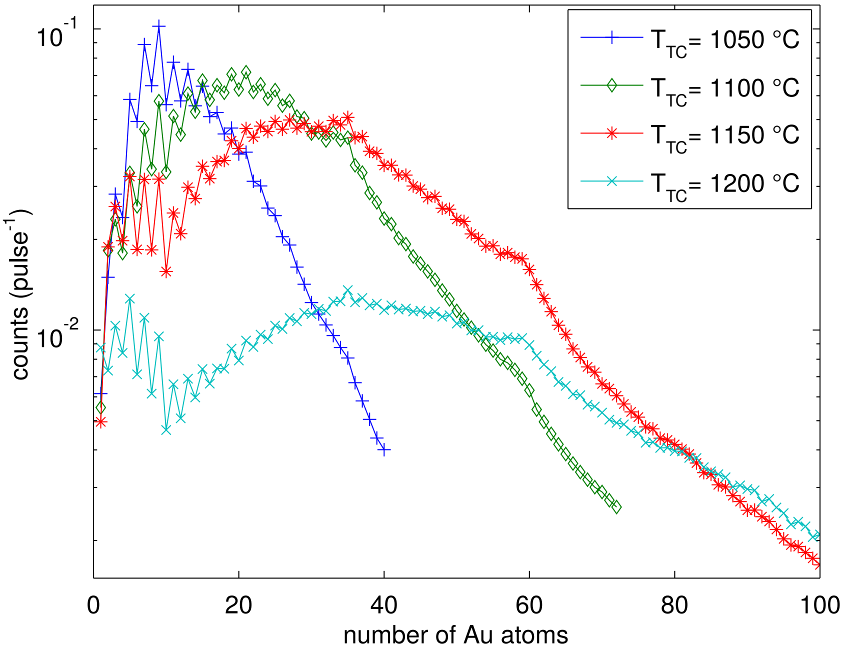

Figure 3.24: Counts contained in each Au peak extracted from Fig. 3.23. The datapoints are connected to guide the eye.

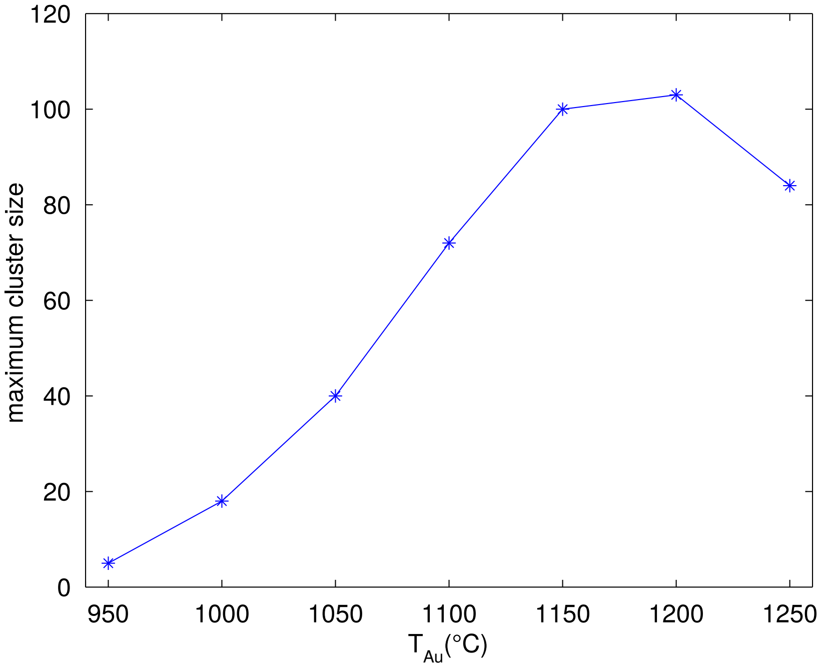

Figure 3.25: Maximum Au cluster size in the TOF spectra for different oven temperatures. The datapoints are connected to guide the eye.

3.4.2 Mass Spectra for Different Nozzle Temperatures

The behaviour at different nozzle temperatures (see Fig. 3.26) is also similar to Ag.

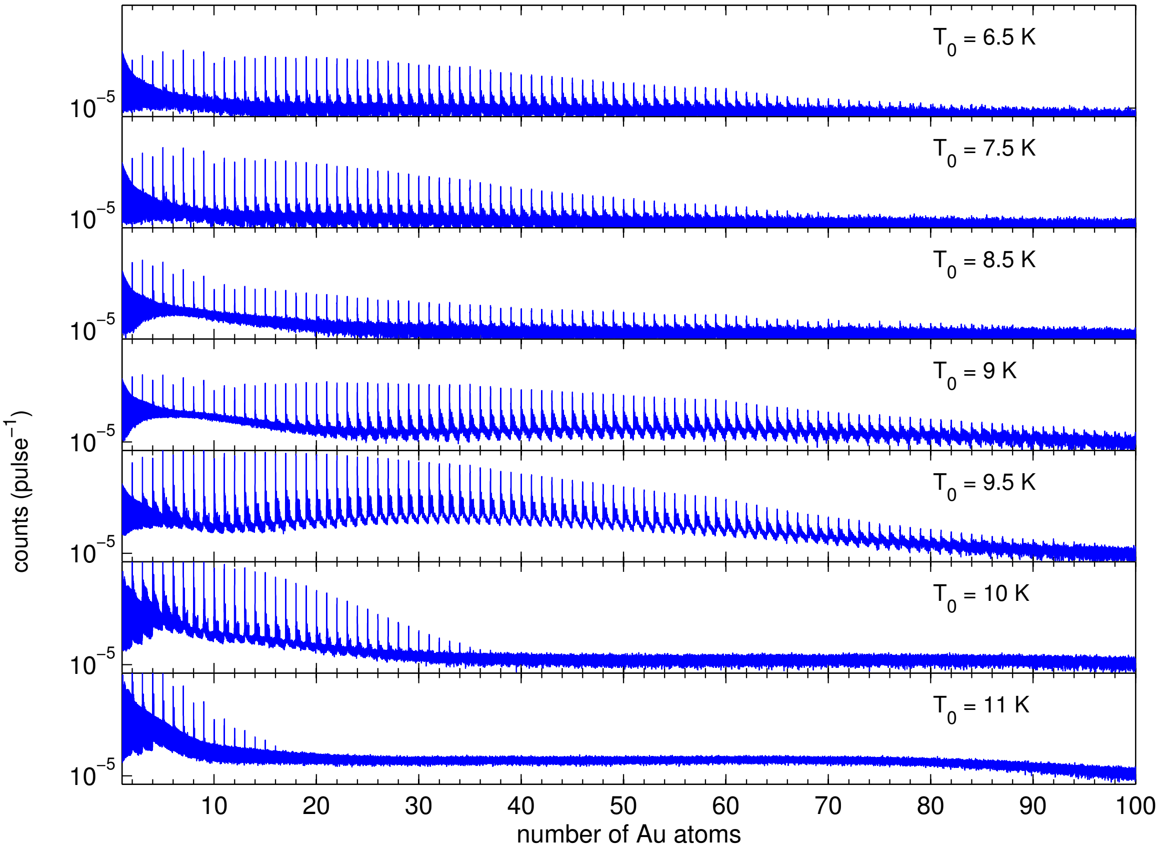

Figure 3.26: Mass spectra obtained for an Au doped He droplet beam at different nozzle temperatures T_0 and $p_0 = 20\,\mathrm{bar}$ for a constant Au oven temperature $T_{\mathrm{TC}} = 1150\,°\mathrm{C}$.

In Fig. 3.27 the shift in the size distribution, described for Ag, around $T_0 = 10\,\mathrm{K}$ can be seen. In the plot of the maximum visible cluster sizes in Fig. 3.28 for different nozzle temperatures, the transition from single- to multi-centre growth at about 9 K can be seen although it is not as distinct as for Ag.

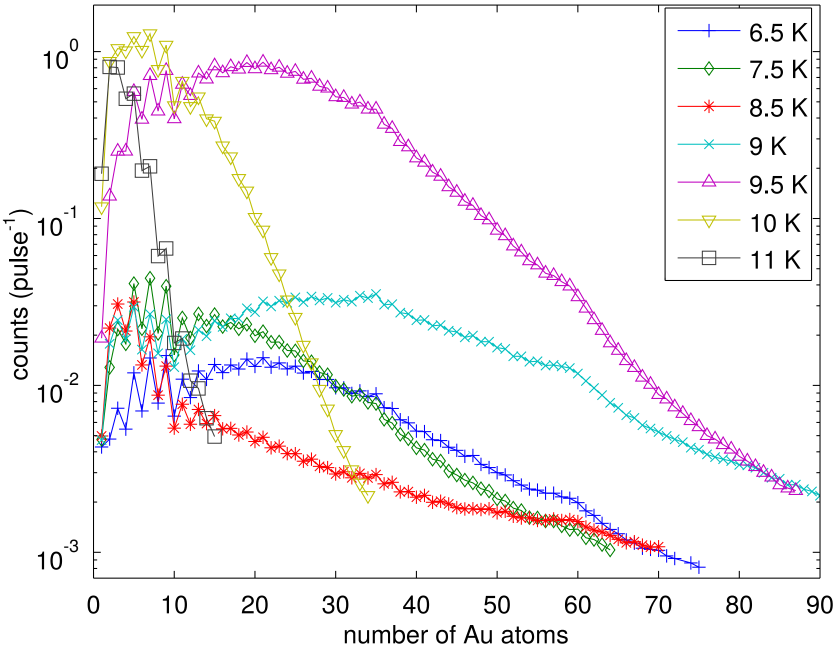

Figure 3.27: Counts contained in each Au peak extracted from Fig. 3.26. The datapoints are connected to guide the eye.

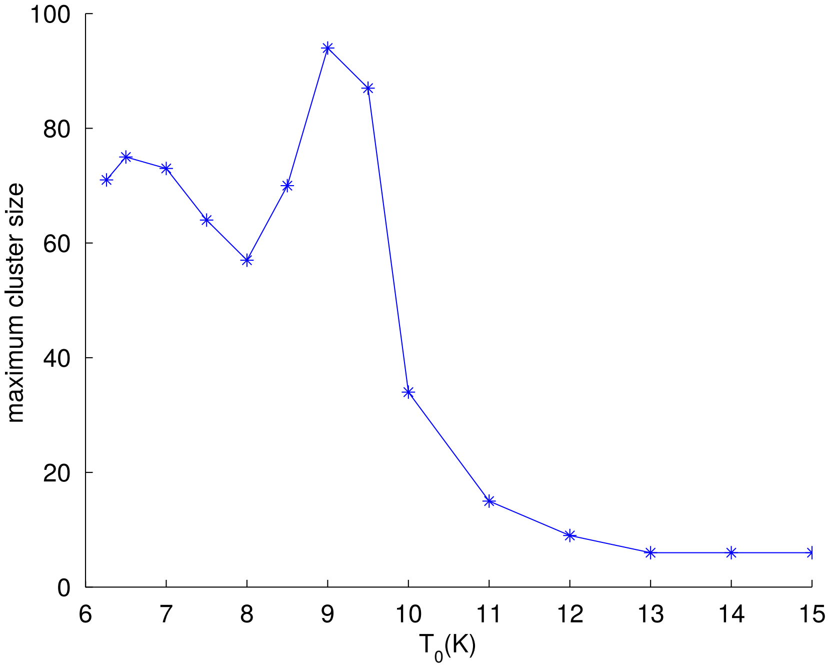

Figure 3.28: Maximum Au cluster size in the TOF spectra for different nozzle temperatures ($p_0 = 20\,\text{bar}$). The datapoints are connected to guide the eye.

3.5 Size Distribution of Clusters

As mentioned before, the size distribution of the resulting clusters, synthesised in a He droplet beam, is dependent on both, the source conditions and the vapour pressure, i.e. the oven temperature. For Ag and Au, the same considerations hold true. The size distributions, plotted in Fig. 3.17, 3.20, 3.24 and 3.27 remind of a log-normal distribution with their maximum dependent on the source- or the oven condition. A log-normal distribution

$$f(x;\mu,\sigma) = \frac{1}{x\sigma\sqrt{2\pi}} e^{-\frac{(\ln(x)-\mu)^2}{2\sigma^2}} \tag{3.1}$$

can be fitted to the data (estimation of the parameters μ and σ), as demonstrated in Fig. 3.29, and the mean cluster size can be calculated from the obtained parameters

$$\langle N_{\mathrm{fit}}\rangle = e^{\mu+\frac{\sigma^2}{2}} \tag{3.2}$$

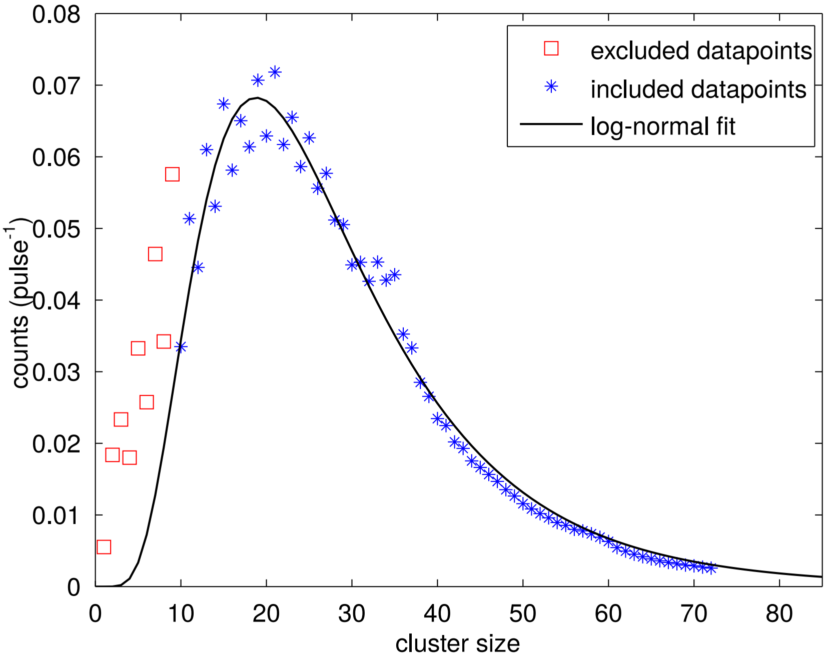

Figure 3.29: Demonstration of a log-normal fit to a cluster size distribution. The data are obtained with the source conditions $T_0 = 9\,\mathrm{K}$, $p_0 = 20\,\mathrm{bar}$ and the Au oven heated to $T_{\mathrm{TC}} = 1100\,°\mathrm{C}$ (green curve in Fig. 3.24). Only the datapoints marked with blue stars contribute to the curve-fit.

A comparison of the log-normal distribution, shown as the black line in Fig. 3.29, with the cluster size distributions for different conditions (e.g. Fig. 3.24) shows that the small cluster sizes do not fit the log-normal model. The more frequent occurrence of small clusters can be ascribed to the fragmentation of bigger clusters during the ionisation process. Therefore, smaller clusters are excluded (marked in red in Fig.

3.29) from the fit and thus do not contribute to the calculated mean cluster size.

Another approach to calculate the mean cluster size is to use the estimation for the mean cluster size, given in Eq. 1.4 by knowing the beam attenuation, which can be measured with a QMS, the mean He droplet size, which can be extracted from Tab. A.5 on page and the binding energies of the dopants, which are listed in Tab. A.6. The binding energy is dependent on the cluster size itself and can be calculated with an empirical formula [37]

$$E_{\mathrm{b}}(N) = E_{\mathrm{b,bulk}} + 2^{\frac{1}{3}}(\frac{1}{2}D_{\mathrm{e}} - E_{\mathrm{b,bulk}})N^{-\frac{1}{3}} \tag{3.3}$$

where the energies $E_{\mathrm{b,bulk}}$ and D_{e} are given in Tab. A.6. For the cluster size N, the value obtained by the fit of the log-normal-distribution as described above is plugged in.

Table 3.4: Mean cluster sizes and beam attenuation for a He droplet beam ($T_0 = 9\,\mathrm{K}$, $p_0 = 20\,\mathrm{bar}$) doped with Ag at different temperatures T_{TC}, where A is the beam attenuation calculated with Eq. 1.2, $\langle N_{\mathrm{Ag,calc}}\rangle$ is the mean cluster size, calculated with Eq. 1.4 and $\langle N_{\mathrm{Ag,fit}}\rangle$ is the mean cluster size obtained by a fit, as demonstrated in Fig. 3.29.

T_{TC} (°C)	A (%)	$\langle N_{\mathrm{Ag,calc}}\rangle$	$\langle N_{\mathrm{Ag,fit}}\rangle$
750	4	22	20
800	24	113	81
850	55	245	162
875	77	302	-

Table 3.5: Mean cluster sizes and beam attenuation for a He droplet beam ($T_0 = 9\,\mathrm{K}$, $p_0 = 20\,\mathrm{bar}$) doped with Au at different temperatures T_{TC}, where A is the beam attenuation calculated with Eq. 1.2, $\langle N_{\mathrm{Au,calc}}\rangle$ is the mean cluster size, calculated with Eq. 1.4 and $\langle N_{\mathrm{Au,fit}}\rangle$ is the mean cluster size obtained by a fit, as demonstrated in Fig. 3.29.

T_{TC} (°C)	A (%)	$\langle N_{\mathrm{Au,calc}}\rangle$	$\langle N_{\mathrm{Au,fit}}\rangle$
1000	2	10	8
1050	2.5	11	16
1100	5	20	26
1150	19	74	36
1200	40	152	49
1250	71	280	-

Both methods are compared in Tab. 3.4 for Ag and in Tab. 3.5 for Au. For small cluster sizes they yield comparable results. For big clusters fragmentation processes or sensitivity related issues might become dominant and therefore the measured size distribution in the spectra is shifted towards smaller masses. In the analysis of the spectra only the bare metal clusters ($\mathrm{M_n}$) were taken into account. Since all clusters with the size n also appear as a compound of metal and water $\mathrm{M_n(H_2O)_m}$ the actual occurrence for the size $\mathrm{M_n}$ would be the sum over all m. The same goes for the additional He atoms (solvation shells). Practically these summations are very difficult or even impossible as $\mathrm{M_n(H_2O)_m}$ may overlap with $\mathrm{M_{n+1}(H_2O)_k}$.

The values for $\langle N_{\mathrm{Au,calc}}\rangle$ evaluated with Eq. 1.4 may have a systematic error due to the difference in the diameters of the nozzle plates and thus in the actual mean droplet size at a certain pressure and nozzle temperature. Although both platinum nozzle plates used in the apparatus within this thesis and the one used by Gomez *et al.* have a nominal diameter of $5\,\mu$m, the actual diameter can differ, as the SEM measurement in Fig. 2.2 showed. Also the temperature and pressure measurements can be sources of uncertainty. For the calculation it is assumed that every He atom that evaporates from the droplet dissipates the binding energy of 0.62 eV. However, it is also possible that small He droplets get evaporated from the droplet. They fully contribute to the beam attenuation but dissipate less binding energy, because they are still bound, which results in an error in the cluster size $\langle N_{\mathrm{Au,calc}}\rangle$.

A comparison of the measured mass spectra with a simulation of the droplet- and pickup-process failed because of the complexity of the process. Multiple convolutions are present in this process. The droplet size distribution (log-normal or exponential) convolutes with the pickup statistics (poisson-distribution) and for detection this also convolutes with the ionisation probability, the cluster stability and the sensitivity function of the TOFMS.

3.6 Anomalies in Noble Metal Clusters

Noble metals, as Ag and Au, have an electronic configuration (ending on $n\mathrm{d}^{10}(\mathrm{n}+1)\mathrm{s}^1$), which is similar to the one of alkali metals like Na ($[\mathrm{Ne}]3\mathrm{s}^1$). Therefore, the considerations for magic numbers for Na clusters in Sec. 1.5.4 can be adopted for noble metals and both metals, Ag and Au, should behave alike. As seen in the previous Sec. 3.3 and 3.4, the abundance pattern for the different cluster sizes include some non trivial effects, including even-odd-oscillations and the occurrence of magic numbers.

3.6.1 Even-Odd-Oscillation

In all plots, where the counts contained in each peak in the different mass spectra were summed up (Fig. 3.17, 3.20, 3.24 and 3.27), an even-odd-oscillation in the abundance pattern of small clusters is present.

In Fig. 3.30 the abundance of Ag clusters (also plotted in Fig. 3.16 for $T_0 = 9\,\mathrm{K}$,

$p_0 = 20\,\mathrm{bar}$ and $T_{\mathrm{TC}} = 800\,^\circ\mathrm{C}$) is shown. As seen before, the clusters consisting of an odd number of atoms are more common than the even numbered ones. The even-odd alternation is particularely well illustrated in the inset of Fig. 3.30 which shows the ratio of adjacent peaks. For Ag it vanishes at a cluster size of about 40 atoms. The same value was found for Cu as well [80], whereas the even-odd oscillations for Cu are not as distinct as for Ag [81]. The cause of the even-odd effect is ascribed to electron pairing [82], as can be seen in mass spectra of the alkali-metals rubidium (Rb) and cesium (Cs) [83].

An odd numbered cluster can be ionised easier, i.e. has a lower ionisation potential as an even numbered cluster because of the unpaired electron. The ionisation potential of Ag is given in Fig. 3.31 and also shows the even-odd-alternation as observed in the mass spectrum. Another aspect is the alternating growth of the binding energy as the cluster gets bigger and slowly approaches the bulk binding energy of $3\,\mathrm{eV}$ [29, 84].

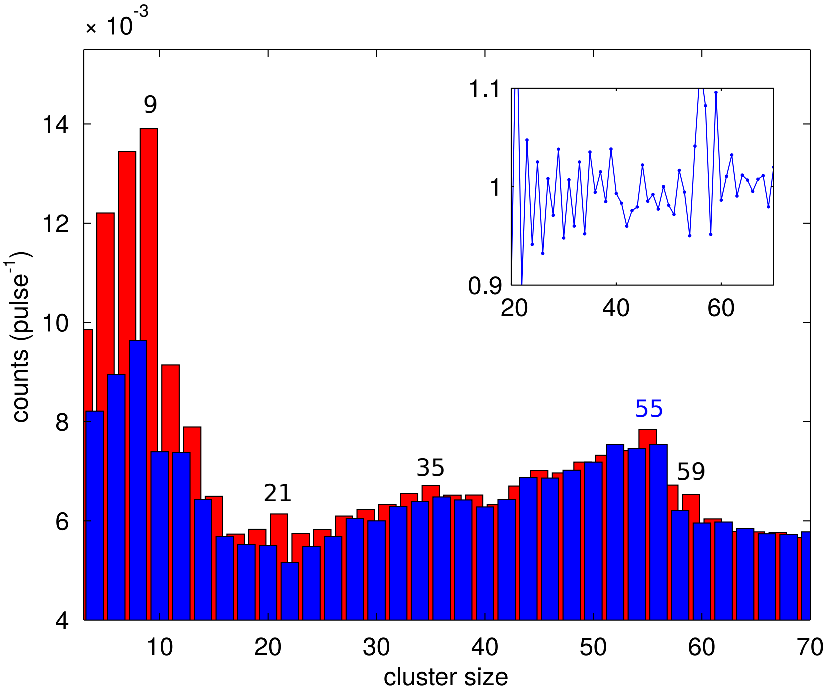

Figure 3.30: Abundance of the different cluster sizes for an Ag doped He droplet beam. The red and blue bars mark the odd and even numbered cluster sizes, respectively. The inset shows the ratio of adjacent peaks. The magic numbers are indicated.

For an Ag mass spectrum with bigger clusters ($T_{\mathrm{TC}} = 850\,^\circ\mathrm{C}$) no overall even-odd-alternation exists, but there are some ranges, e.g. from $n = 54$ to 63, where the odd numbered clusters are more dominant, as Fig. 3.32 shows.

Au has a bigger ionisation energy and a bigger binding energy than Ag. Therefore, the effects induced by electronic properties, which include both the even-odd alternation and the occurrence of magic numbers, are expected to be stronger for Au. Fig. 3.33 shows the abundance of Au clusters in an Au doped ($T_{\mathrm{TC}} = 1200\,^\circ\mathrm{C}$) He droplet

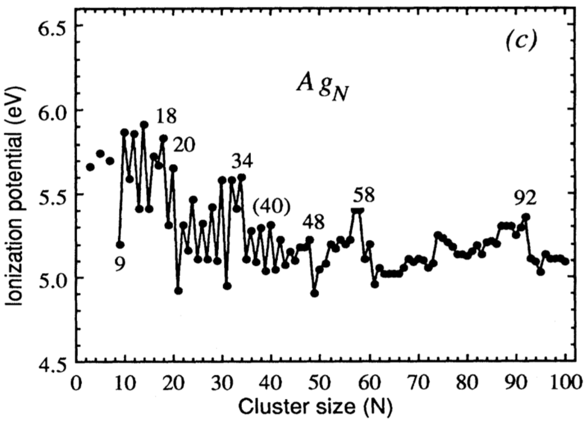

Figure 3.31: Ionisation Potential of Ag. The smaller the ionisation potential the less energy is needed for ionisation. Taken from Ref. [85].

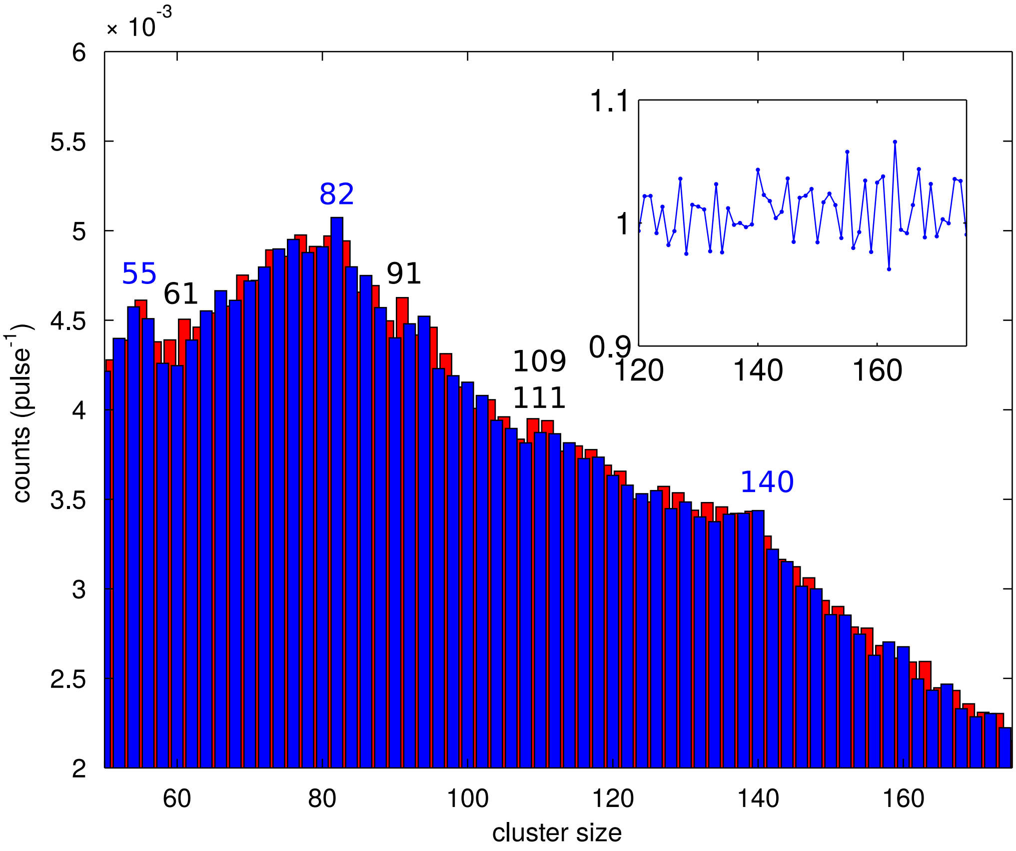

Figure 3.32: Abundance of bigger Ag clusters. The blue bars mark the even, the red bars the odd numbered clusters. The inset shows the ratio of adjacent peaks. Magic numbers are indicated.

beam ($T_0 = 9\,\mathrm{K}$, $p_0 = 20\,\mathrm{bar}$). The even-odd alternation is visible up to a cluster size of 58 (see inset in Fig. 3.33) which is well above the limit for Ag. A comparison between Ag and Au reveals a bigger even-odd-effect for small clusters for Ag but a faster decay with the cluster size.

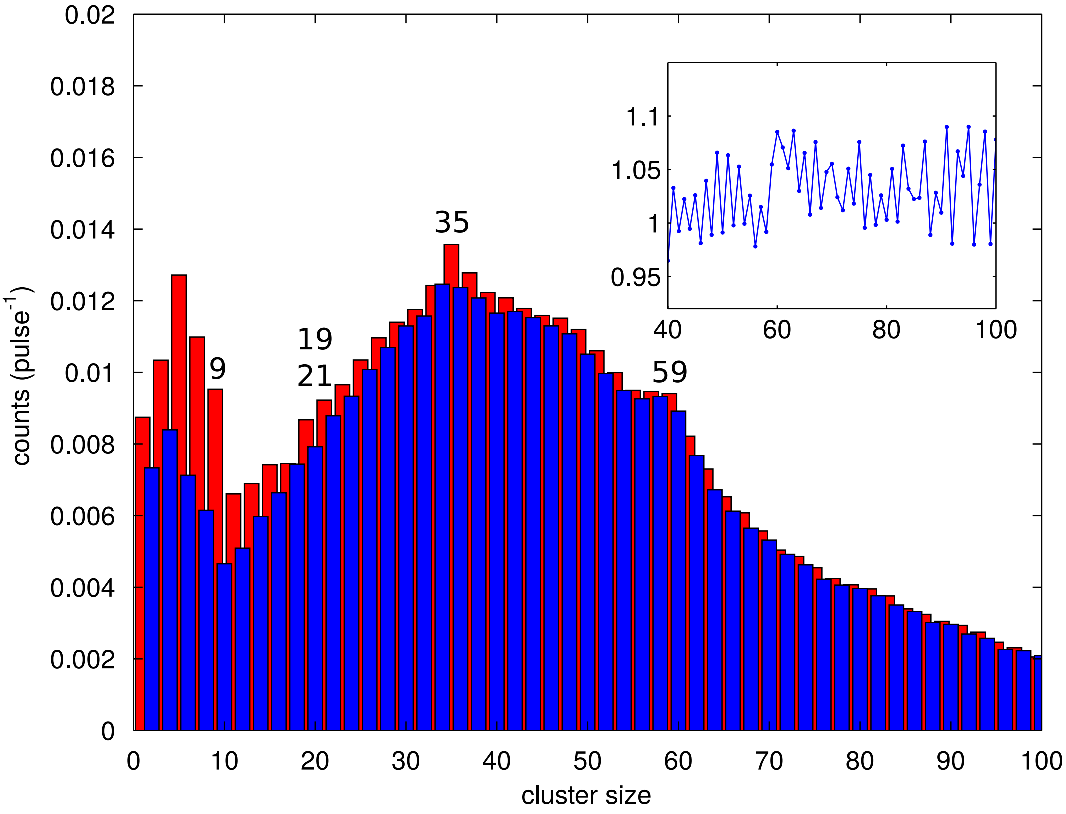

Figure 3.33: Cluster size abundance for Au clusters. The blue bars mark the even, the red bars the odd numbered clusters. The inset shows the ratio of adjacent peaks. Magic numbers are indicated.

3.6.2 Magic Numbers

In the abundance-plots for the cluster sizes (Fig. 3.30, 3.32 and 3.33) the magic numbers were indicated. With black labels the magic numbers, originating from closed electronic shells and with blue labels the sizes with structural enhanced stabilities are given. Baletto *et al.* calculated structurally favoured Ag cluster sizes for different possible morphologies (Ih, Dh and fcc) [55]. For Ag_n the structural magic numbers for cluster sizes of 55 (Ih), 82 and 140 (both fcc) can be observed. The small feature at a cluster size of 100 can be ascribed to a decahedral structure. For Au none of these cluster sizes can be found to be magic in the abundance pattern.

Magic numbers, not ascribed to structurally favoured cluster sizes, corresponding to minima of the ionisation potential which appear because of closed electronic shells, are visible in both the Ag- and Au mass spectra. The cluster sizes 9, 19, 21, 35, 59, 61 and 91 were already ascribed to closed electronic shells in the spherical jellium model in Sec. 1.5.4[3]. They are in good agreement with the values reported for Rb and Cs in

---

[3] They are shifted by a size of 1 because not the neutral cluster but the positive cluster ion is analysed.

Ref. [83].

Some anomalies (109/111, 158/160, 163, 195) cannot be ascribed to either effect and their origin remains to be understood. A possible explanation could be provided by a different model to describe the pattern for the filling of the electronic shells.

3.7 He on Noble Metal Clusters

In this section the He comb, attached to the bare metal clusters, is analysed. The attached He is only visible in the mass spectrum, if the mean He droplet size is small enough, i.e. for relatively high nozzle temperatures and is only present on small metal clusters ($n \lesssim 5$). Fig. 3.34 shows the mass spectrum for an Ag doped He droplet beam, formed under the nozzle conditions of $T_0 = 12\,\mathrm{K}$ and $p_0 = 20\,\mathrm{bar}$ ($\langle N_{\mathrm{He}} \rangle \approx 11600$).

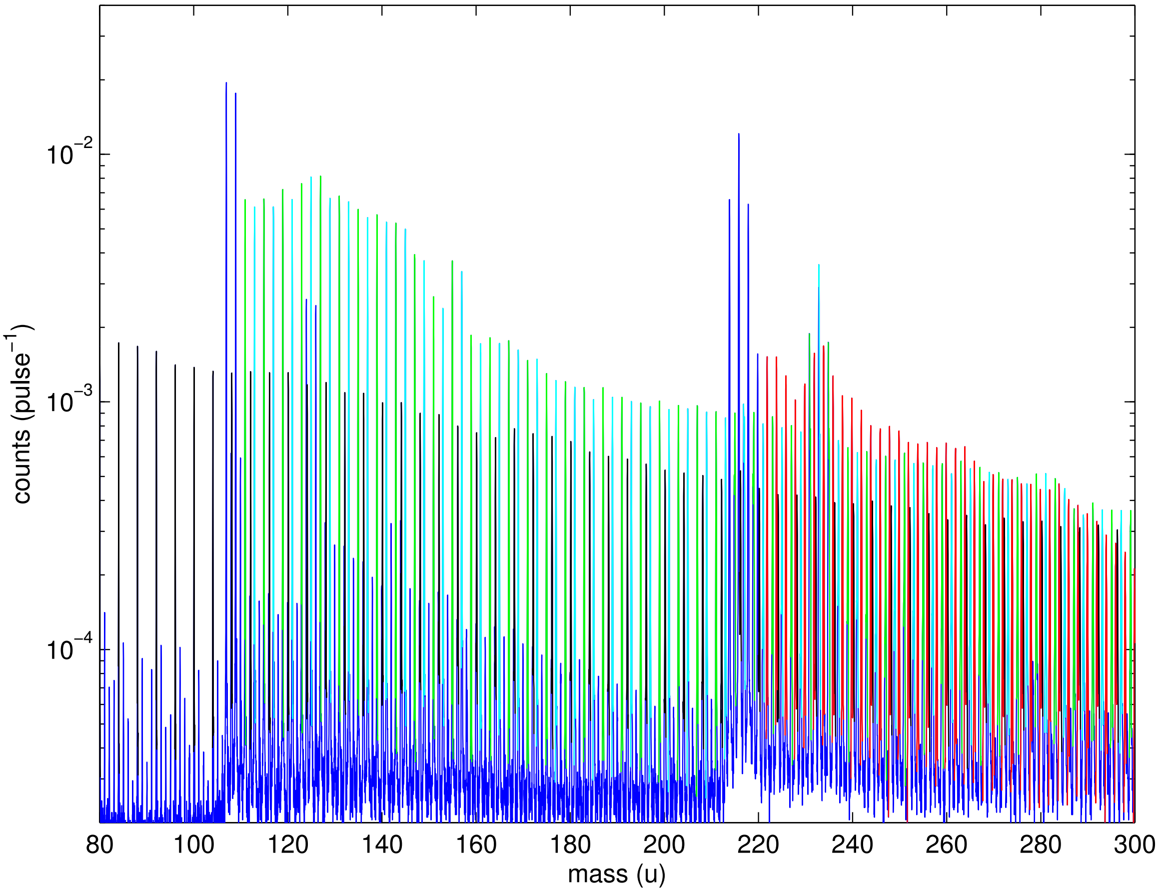

Figure 3.34: Mass spectrum of an Ag ($T_{\mathrm{TC}} = 850\,°\mathrm{C}$) doped He droplet beam. The black peaks indicate the bare He droplet beam, the green and cyan peaks mark the He that is attached to the Ag_1, the red peaks mark the He that is attached to the Ag_2. The blue line represents the rest of the mass spectrum, including the peaks for the Ag_1 and Ag_2 at around 108 and 216 u, respectively.

When summing over each peak, originating from He attached to the Ag monomer while distinguishing between the two isotopes of Ag, Fig. 3.35 can be plotted.

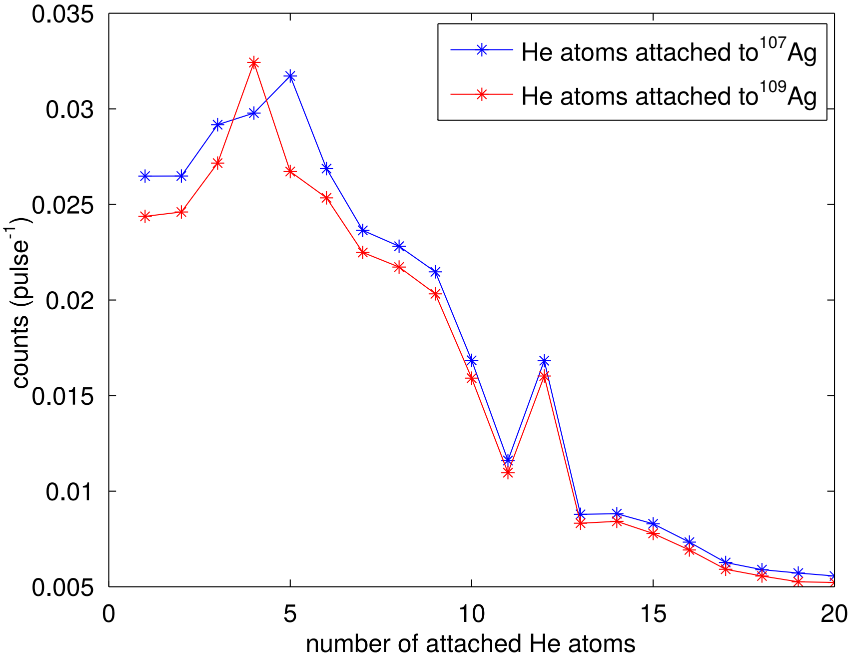

Figure 3.35: Counts contained in each He peak, attached to the Ag monomer (green and cyan in Fig. 3.34). Extracted from Fig. 3.34.

The dopant is solved in the He droplet, one speaks of so called solvation shells. The formation of such structures is governed by the higher binding energy of D^+-He compared to the He-He interaction (where D is the dopant atom) [86]. The peak at $n = 12$ can be explained by the formation of a closed icosahedral structure, consisting of one Ag atom at the centre and 12 He atoms. For the peaks at $n = 4$ and $n = 5$ for ^{109}Ag and ^{107}Ag, no explanation exists for now. Especially the different behaviour of the two isotopes remains to be understood. A solvation shell for such small compounds was only observed for light atoms of the alkali species [87]. Schöbel *et al.* analysed the solvation shells for krypton and did not find any difference in the solvation shells for different isotopes [74]. However there is also the possibility that the peaks at $n = 4$ and $n = 5$ originate from other compounds (e.g. $Ag_1(H_2O)$).

For an Au doped He droplet beam under the same source conditions ($T_0 = 12\,K$, $p_0 = 20\,bar$, $\langle N_{He} \rangle \approx 11600$) the mass spectrum is shown in Fig. 3.37.

Fig. 3.36 again shows a closed solvation shell at $AuHe_n$ for $n = 12$, hence a stable icosahedral structure. Additionally a feature at $n = 7$, especially for the Au dimer is present. A solvation shell of $n = 7$ was calculated for Li and Na dimer cations in He droplets and could therefore also be present for Au [86, 88]. In Ref. [89] it was shown that for heavier atoms the solvation shells tend to get bigger. This trend can be seen in a comparison of the curves for Ag and Au.

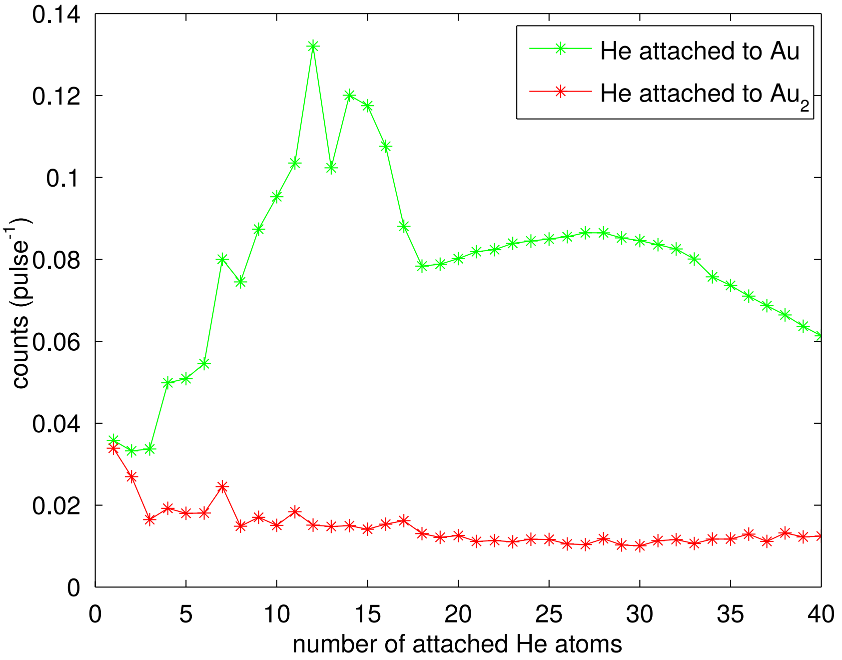

Figure 3.36: Counts contained in each He peak, attached to the Au monomer (green) the Au dimer (red). Extracted from Fig. 3.37.

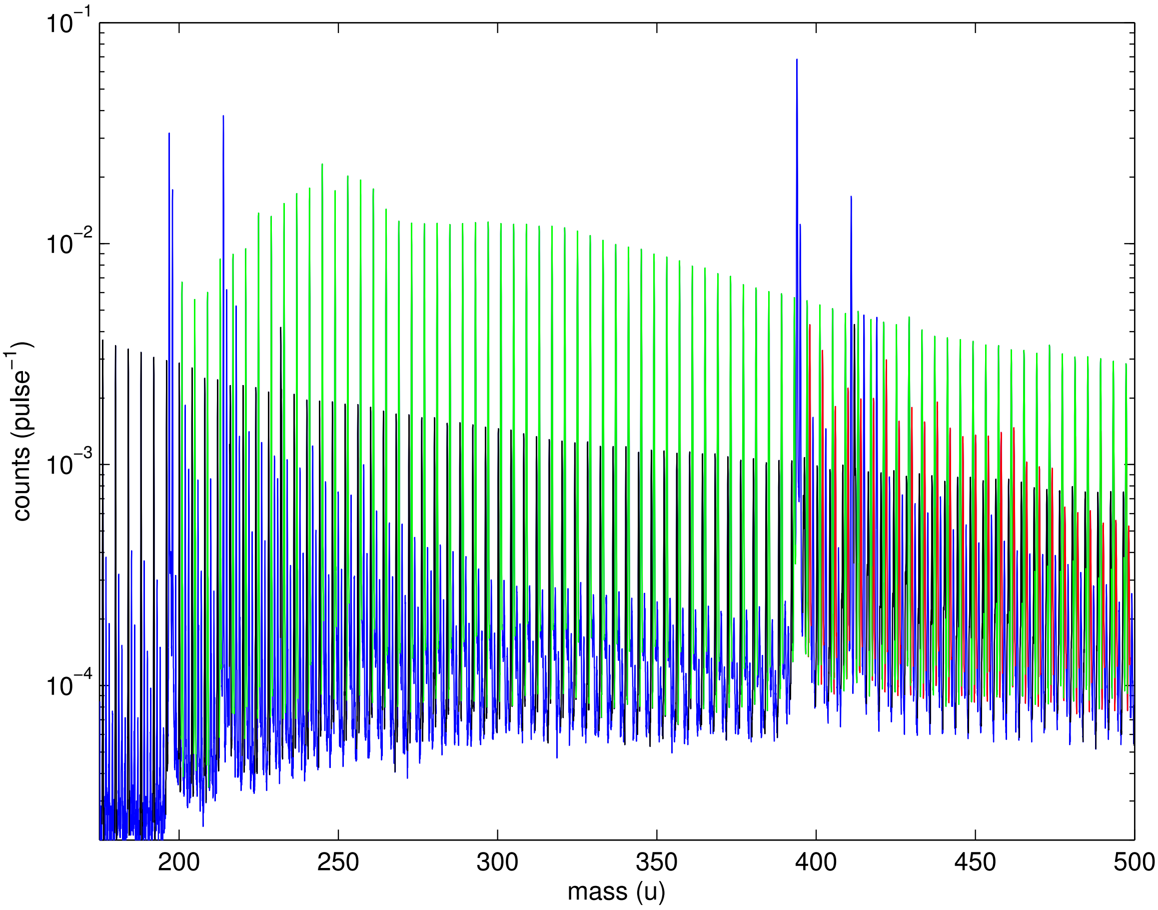

Figure 3.37: Mass spectrum of an Au ($T_{\mathrm{TC}} = 1150\,^{\circ}\mathrm{C}$) doped He droplet beam. The black peaks indicate the bare He droplet beam, the green peaks mark the He that is attached to the Au monomer, the red peaks mark the He that is attached to the Au dimer. The blue line represents the rest of the mass spectrum, including the peaks for the Au_1 and Au_2 at 197 and 394 u, respectively.

3.8 Water on Noble Metal Clusters

As mentioned before, not the whole droplet beam path is at UHV conditions. There is still a reasonable amount of water in the PU-chamber. This water is picked up by the He droplet along with the vaporised metal and manifests in the mass spectra. For a low oven temperature the water pickup can overcome the metal pickup. This case is plotted in Fig. 3.38 and especially for the Au dimer the $Au_2(H_2O)_x$ is higher than the bare Au_2 cluster signal.

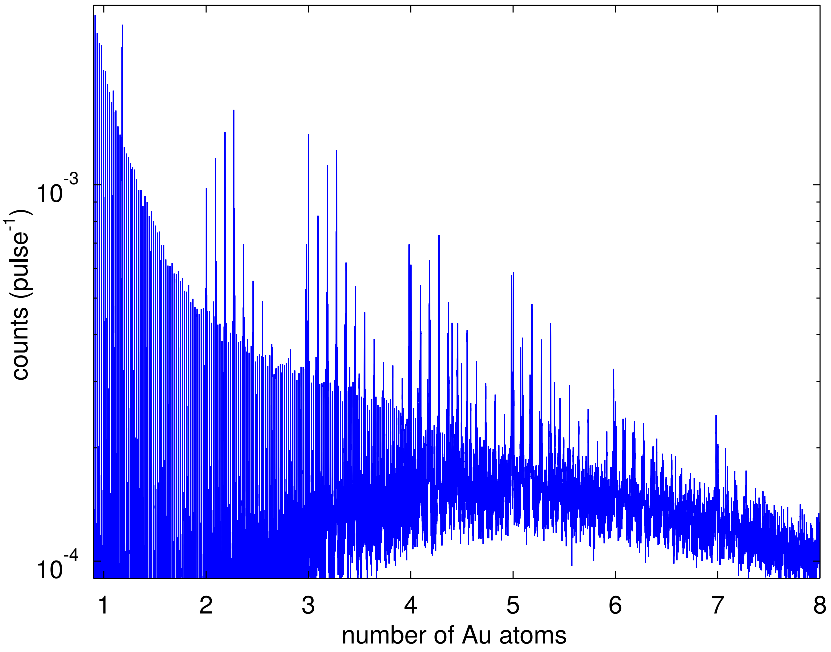

Figure 3.38: Au doped He droplet beam for a low oven temperature to illustrate the water pickup ($T_0 = 9\,\mathrm{K}$, $p_0 = 20\,\mathrm{bar}$, $T_{\mathrm{TC}} = 950\,°\mathrm{C}$).

Every peak originating from an Au cluster is followed by multiple water peaks $Au_n(H_2O)_m$. The bigger the metal cluster gets, the more water peaks follow the metal cluster peak ($m \propto n$). Additionally, and shown for the Ag_8-cluster in Fig. 3.15, not only H_2O but also OH and H_3O are present in the mass spectrum, which results in a broadening of the $Au_n(H_2O)_m$ peaks. The reaction taking place is [90]

$$\mathrm{H_2O(H_2O)_n + e^- \longrightarrow H^+(H_2O)_{n-m-1} + mH_2O + OH} \tag{3.4}$$

or similar with another dopant (e.g. Au or Ag) present in the He droplet [91].

A closer look, especially into the mass spectra of Ag (e.g. 3.14) and its $Ag_n(H_2O)_m$ peaks, reveals even-odd oscillations in n for the $Ag_n(H_2O)_1$ peaks. This is depicted in the upper plot of Fig. 3.39. A slightly higher abundance of the even sizes can be seen. The lower plot shows the relative height of the $Ag_n(H_2O)_1$ with respect to the Ag_n peak, where the effect gets more distinct. The same alternation but weaker goes for $Au_n(H_2O)_1$ plotted in Fig. 3.40. In both cases the opposite even-odd oscillation, compared the the bare metal clusters, is present. Here the even numbered metal clusters with one water molecule are more common than the odd numbered metal clusters with one water molecule. The reason for this could be that even numbered cluster ions have one valence electron, hence dangling bond, which odd numbered clusters don't have and are therefore more reactive. Winter *et al.* showed that the reacivity of a cluster does not only depend on its electronic but also on its geometric structure [80]. Especially for Au this can be seen in the form of a maximum around the closed icosahedron at $n = 13$.

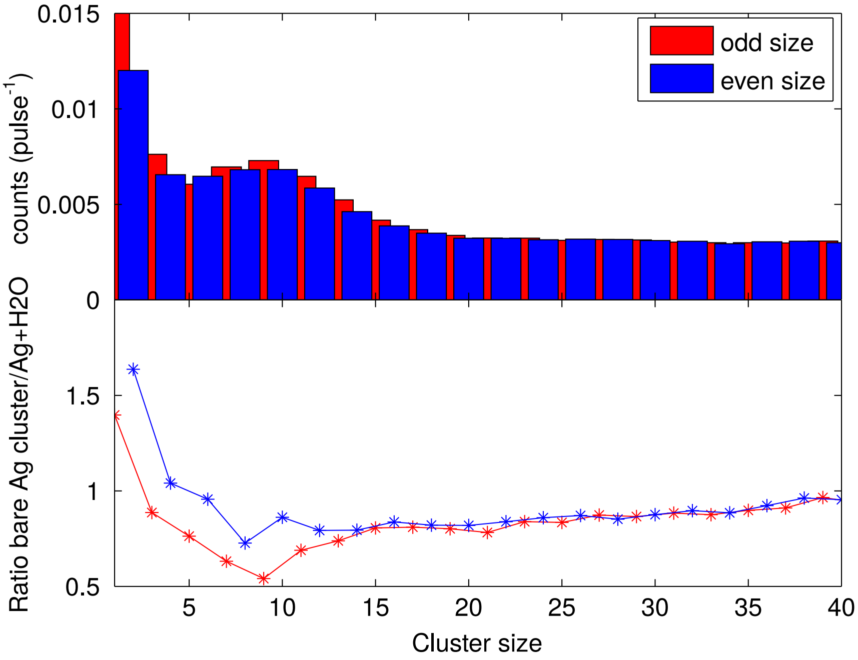

Figure 3.39: To the even-odd-effect of $Ag_n(H_2O)_1$. ($T_0 = 9\,\mathrm{K}$, $p_0 = 20\,\mathrm{bar}$, $T_{\mathrm{TC}} = 750\,°\mathrm{C}$).

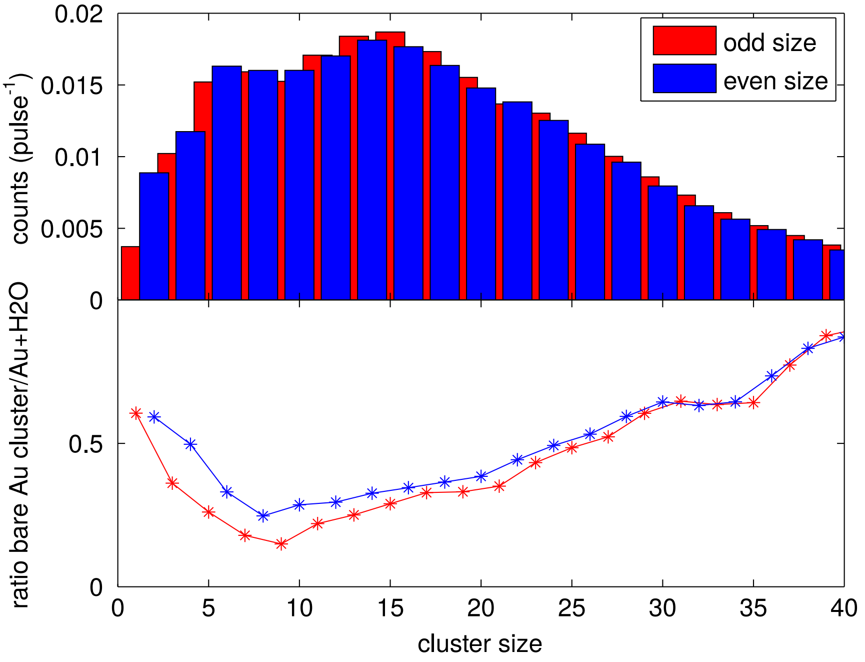

Figure 3.40: To the even-odd-effect of $Au_n(H_2O)_1$. ($T_0 = 9\,K$, $p_0 = 20\,bar$, $T_{TC} = 1050\,°C$).

3.9 Analysis of Xenon Clusters

Xe clusters are held together by Van-der-Waals interaction between the atoms. The corresponding binding energies are much lower than the ones of metal clusters (see Tab. A.6). Therefore, not as many He atoms get evaporated if a Xe atom is picked up (92 atoms)[4] as if a metal atom is (4800 atoms for Ag). This effect is also indicated by the fact that there are no clusters visible in the TOF mass spectrum for low nozzle temperatures (below 10 K in this experiment with $p_0 = 20\,bar$). Because of large big He shell around the Xe cluster, the dopant is not ionized efficiently, as explained in Sec. 1.5.1.

In Fig. 3.41 the TOF mass spectrum for Xe pickup by using the gas pickup cell ((5) in Fig 2.1) is plotted. The pressure in the PUC is maintained at about $p_{PU} = 10^{-6}\,mbar$ by pouring in Xe with a dosing valve through the gas pickup cell (the pressure in the gas pickup cell is significantly higher). The magic numbers are indicated in the plot. For reference a mass spectrum obtained by adiabatic expansion of Xe is plotted in Fig. 3.42. The spectra are in good agreement. The origin of this magic numbers is discussed in Sec. 1.5.4.

Noticeable in the measured spectrum Fig. 3.41 is the abrupt decrease in signal intensity at $n_{Xe} = 55$. At $n = 55$ a icosahedral structure has a closed shell, i.e. the number of atoms is a magic number. This configuration is more stable than slightly

---

[4] Note that for Xe the thermal energy ($k_B T$) is bigger than the Xe-Xe binding energy

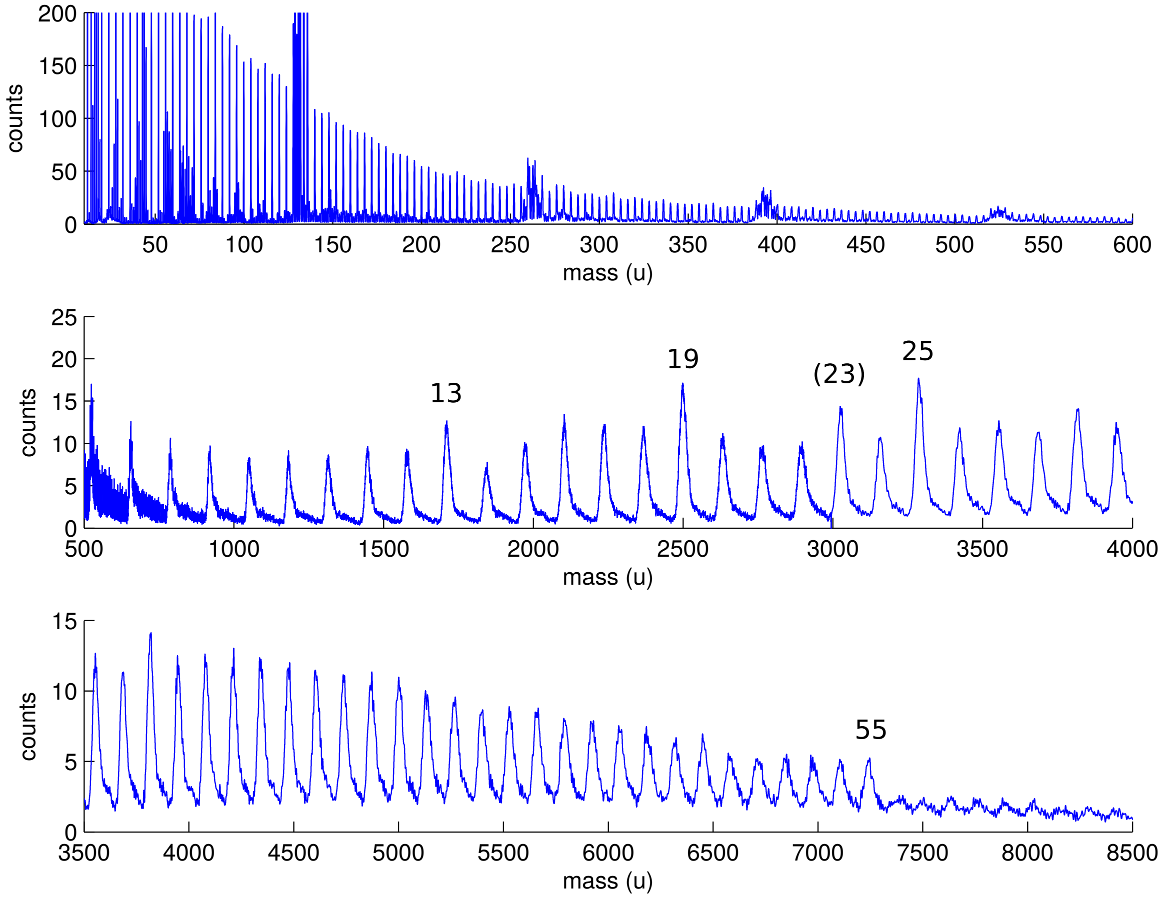

Figure 3.41: Mass spectrum of Xe clusters aggregated in a He droplet beam under the source conditions $T_0 = 10.5\,\mathrm{K}$ and $p_0 = 20\,\mathrm{bar}$. For masses < 600 the mass spectrum of the He droplets (He comb) is visible. The data up to mass 3000 is smoothed. For bigger masses a Dirichlet-filter was applied. The TOFMS-settings from Tab. A.2 were used.

bigger clusters, which might not survive the ionisation and extraction by the mass spectrometer and break up, e.g. in two clusters with $n = 55$ and $n = 5$, and will be detected as such.

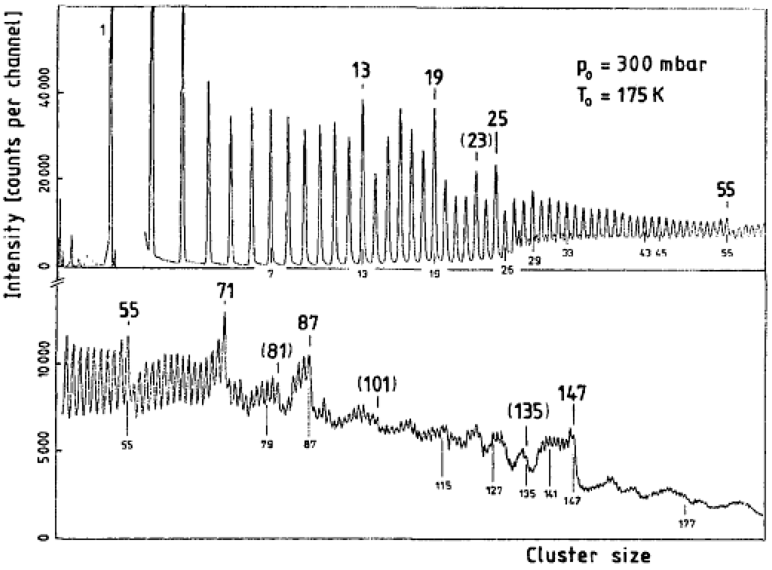

Figure 3.42: Mass spectrum of Xe clusters generated by adiabatic expansion. Taken from Ref. [92].

3.10 TEM Analysis

For the analysis of size distributions or atom arrangements (crystal structures) of nanoparticles transmission electron microscopy (TEM) is a suitable technique. The substrates[5] are mounted on a manipulator in the MC. The deposition conditions are controlled by monitoring the He partial pressure in the MC and by measuring the deposition rate with the QCM. With the partial pressure the beam attenuation can be calculated, which is important for the resulting cluster size distribution. For the analysis of size distributions a high surface coverage is beneficial. Fig. 3.43a shows a TEM image of such a substrate after the deposition of Ag clusters.

With such an image, size distributions like the one in Fig. 1.6 can be obtained. By additional HRTEM imaging, as shows in Fig. 3.43b, insight in the clusters crystal structure can be gained.

To influence the resulting size of the clusters, the nozzle conditions are varied and the beam attenuation is held constant by e.g. raising the oven temperature when lower nozzle temperatures are approached.

At some point the droplet formation mechanism changes from gas condensation to the break up of a fluid jet into droplets, which results in the occurrence of so called quantised vortices (see Sec. 1.4). Their appearance manifests in the shape of the resulting deposited clusters as a comparison of Fig. 3.43a and Fig. 3.44a shows.

In the latter case the particles have tracklike shapes (see Fig. 3.44b). This shapes were first observed by Gomez *et al.* for Ag doped He droplets [19]. They also ob-

---

[5] Ted pella ultrathin carbon film on holey carbon support film / 400 mesh copper grid

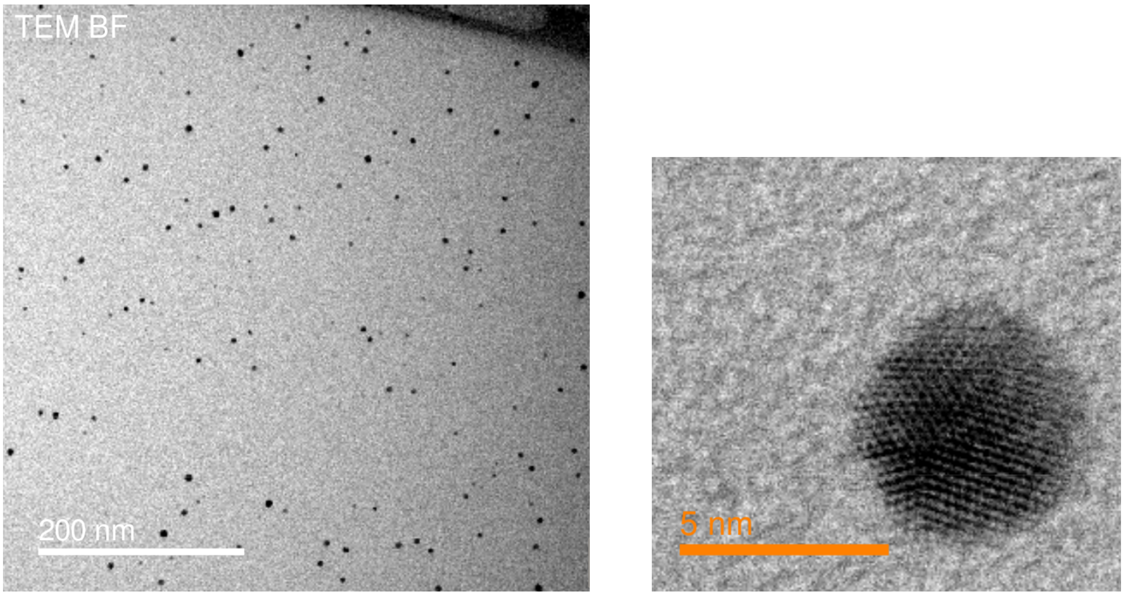

(a) (b)

Figure 3.43: (a): TEM image of an amorphous carbon substrate with Ag clusters deposited for 5 min ($T_0 = 6.52\,\mathrm{K}$, $p_0 = 50\,\mathrm{bar}$ and $I_{\mathrm{Ag}} = 24\,\mathrm{A}$, $U_{\mathrm{Ag}} = 6.6\,\mathrm{V} \rightarrow A \approx 74\,\%$). (b): HRTEM image of a twinned Ag particle with a diameter of about 5 nm.

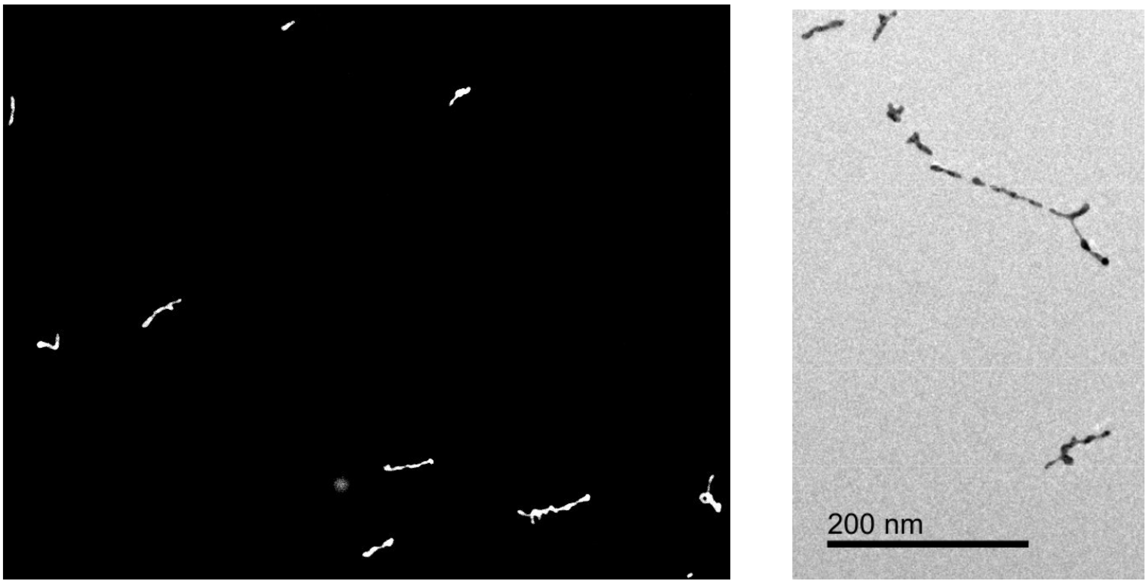

(a) (b)

Figure 3.44: (a): TEM image of a deposited He droplet beam ($T_0 = 6.51\,\mathrm{K}$, $p_0 = 50\,\mathrm{bar}$, $\langle N_{\mathrm{He}} \rangle \approx 10^{10} \rightarrow r_{\mathrm{He}} \approx 1000\,\mathrm{nm}$) doped with Au ($T_{\mathrm{TC}} = 1300\,^{\circ}\mathrm{C} \rightarrow \ A \approx 70\,\%$). The contrast of the original image was enhanced. The deposited Au particles are shown in white, the substrate in black. The resulting nanowires have a length of up to over 100 nm. The deposition time was 10 s. (b): detailed image of a nanowire from the same substrate.

served multiple vortices in one droplet, which could be the explanation for the parallel nanowires in Fig. 3.44a which could originate from the same droplet.

A remaining question was if the dopants are pinned to the vortex one by one or if the atoms synthesise into clusters in a multi-center-growth process and the clusters get pinned to the vortex line. The two cases should manifest in a different atom arrangement in the resulting nanowires. In the first case a monocrystalline structure throughout the nanowire and for the latter case a structure with multiple domains of different crystal orientation and/or crystal structures is expected.

This question could be answered by HRTEM imaging (see Fig. 3.45). Different crystal orientations are present within the nanoparticle. The mechanism that attracts the clusters to the vortices and joins the spherical clusters into rod-like shapes remains to be understood. Either some atoms are attached to the contact area or the clusters undergoes some sort of melting process due to the release of the cluster-cluster binding energy. The picture is different for nanowires (e.g. indium nanowires) produced in superfluid bulk He which are monocrystalline [93].

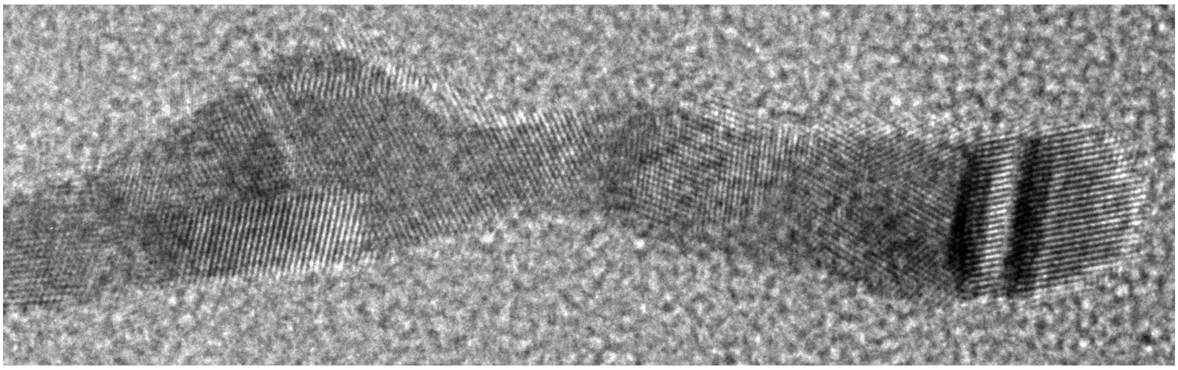

Figure 3.45: HRTEM image of an Au nanowire from Fig. 3.44a. Multiple structural domains are visible.

In a further experiment the droplet beam ($T_0 = 6.02\,\mathrm{K}$, $p_0 = 21\,\mathrm{bar}$) was subsequently doped with both, Au ($T_{\mathrm{TC}} = 1250\,^\circ\mathrm{C}$) and Ag ($I_{\mathrm{Ag}} = 22\,\mathrm{A}$, $U_{\mathrm{Ag}} = 6.25\,\mathrm{V}$, crossed beam setup used). An image of a resulting deposited nanowire is shown in Fig. 3.46a. The EDX spectra show the Au in the centre and the Ag as a shell around the Ag core. From a comparison of Fig. 3.46c and Fig. 3.46d the thickness of the Ag shell can be estimated to be about 1 nm.

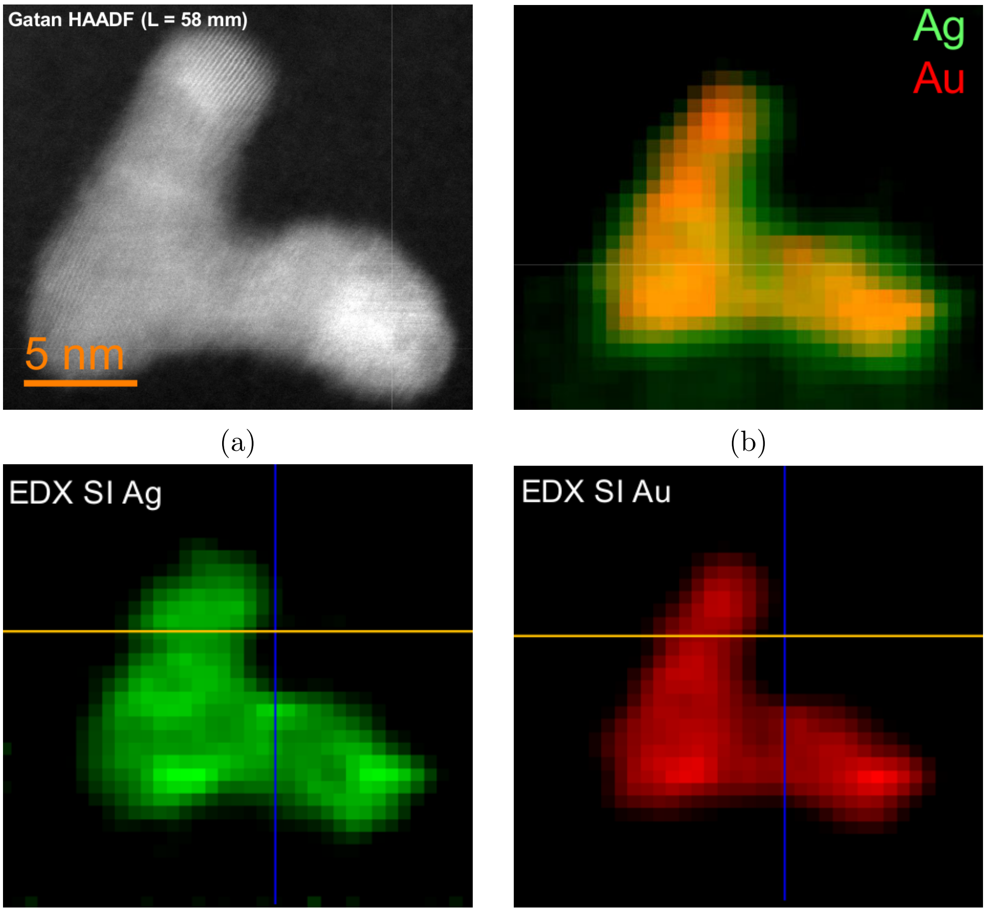

(a) (b)

(c) (d)

Figure 3.46: HRSTEM image of a short nanowire (a). EDX image of the same nanowire (b). EDX images filtered for Ag (c) and Au (d). The Au resides in the centre and is covered by an Ag shell.

Conclusion

Within this thesis the apparatus for cluster deposition was completed with a proper temperature stabilisation of the quartz crystal microbalance which allowed accurate determination of deposition rates with an uncertainty in the order of $1 \cdot 10^{-6}\,\frac{\mu\mathrm{g}}{\mathrm{cm}^2\mathrm{s}}$. Additionally a beam flag for the crossed beam oven design was introduced in order to allow a quick determination of beam attenuations during experiments. This is important to estimate the resulting mean cluster size.

Time-of-flight mass spectroscopy was conducted on doped and undoped He droplets. The mass spectra revealed the limit of electron impact ionisation, since no clusters bigger than about 200 Ag atoms could be observed, although the actual cluster size is estimated to be orders of magnitude bigger for some cases. In mass spectra for different droplet sizes the transition temperature from single- to multi-centre growth could be determined to be at $T_0 \approx 8\,\mathrm{K}$.

In the mass spectra of van der Waals clusters anomalies and magic numbers, at structural stable atom arrangements were observed. The structure for these clusters was determined to be icosahedral, since the magic numbers are equal to the closed icosahedral shells for $n = 13$ and $n = 55$ atoms.

For Ag clusters the icosahedral structure also manifests itself in the abundance pattern along with minor fcc structure indication ($n = 82$ and $n = 140$). The major anomalies could be ascribed to filled electronic shells for the cluster ion at $n = 9$, 21, 35, 59, 61 and 91. For Au the picture is comparable, however, no structurally related magic numbers were observed. Closed electronic shells were observed for $n = 9$, 19, 21, 35 and 59. For both metals a dominant even-odd-oscillation is present for small clusters ($n \lesssim 40$ for Ag and $n \lesssim 60$ for Au) which vanishes for bigger clusters.

Analysis of transmission electron microscopy images after deposition revealed a change in the deposited nanoparticles' shapes when nozzle temperatures lower than $T_0 = 6\,\mathrm{K}$ are approached. Rod-like shapes, so called nanowires, were observed whereas for higher nozzle temperatures the synthesised nanoparticles exhibited a spherical shape. The formation of nanowires is ascribed to the occurrence of quantised vortices in the superfluid helium droplet and subsequent pinning of dopants to the vortex. The deposition then shows a two dimensional projection of the vortex line. Additionally nanowires made of two metals, Au and Ag, were fabricated and analysed. Energy dispersive X-ray spectroscopy revealed core-shell-like nanowires with an Au core and a Ag coating.

Outlook

For further mass spectroscopic experiments the ionisation with a laser rather than via electron impact would allow a softer ionisation due to the lack of big excess energies. Therefore, a better analysis of the cluster abundances, including the better understanding of the occurrence of He solvation shells around an ionic cluster core of one or more atoms would be possible. Since Au does not seem to have any preferred atomic arrangement that would manifest as structural magic numbers, HRTEM imaging and following analysis of the crystal structures would be interesting.

In a deposition experiment with switched pickup order for Au and Ag with subsequent TEM and EDX analysis a better understanding for the growth of core-shell nanoparticles could be established. With a new nozzle design lower temperatures and thus much bigger droplets should be accessible. This would clear the way for the investigation of very long nanowires up to the μm-range.

Appendix A

Appendix

A.1 Operating the Time-of-Flight Mass Spectrometer

A.1.1 Recording a Mass Spectrum with the TOFMS

In the following, a guideline for the operation of the TOFMS is given:

- The MCP should have been under a pressure $< 5 \cdot 10^{-6}\,\mathrm{mbar}$ for a few hours before the measurement.
- In the TOF55-software: heat up the filament and start the pulse generator
- Slowly increase the voltages to their operation value. For the MCP not faster than $0.5\,{}^{\mathrm{kV}}/_{\mathrm{min}}$. While increasing the MCP voltage the preamplifier has to be disconnected in case of a sparkover that can destroy the preamplifier.
- Start a series measurement with e.g. 20000 sweeps and optimise one peak, that is not saturated[1]. This can be done by successively changing the last grid, central grid, x-deflection, y-deflection and repeller offset voltages. An optimised peak has a small FWHM, $< 1\,\mathrm{ns}$ for OH ($m = 17\,\mathrm{u}$), while the number of counts under a peak stays nearly constant, independent of the voltage settings.
- If big masses are to be detected this procedure must not be conducted with a low mass peak like OH but with a metal cluster peak, e.g. the Au_{20} cluster. In a spectrum where a peak at a high mass was optimised a low mass peak looks asymmetric and the other way around.

---

[1] A peak is saturated, if the counts under this peak is greater than half the number of sweeps.

A.1.2 Troubleshooting

When there is no signal at all or the signal is very low there are a few things one can try:

- Optimise the electrometer current by adjusting the magnets position. Connect a 50 Ω resistor to the BNC pin #12 to get a continuous electron beam. Then adjust the magnet's position to the maximum electrometer current.
- Check the electrical offset of the preamplifier. Therefore, connect a Multimeter to the output of the preamplifier and measure the direct voltage while the input of the preamplifier is connected to the TOFMS. Adjust the trimmer until the offset is 0.
- Set other values for the discriminator levels in the multiscaler menu.
- Check 9 V battery.
- Try changing a delay value in the pulse generator menu to force a restart of the pulse generator.
- Monitor the output of the preamplifier with a fast oscilloscope.
- Try a higher MCP voltage (ageing of the MCP).

A.1.3 TOF Settings

Table A.1: Some voltage combinations for operating the TOFMS from Ref. [65].

settings number	U_{Repeller}	$U_{\text{Extraction}}$	U_{Liner}	U_{Lens}	U_{LastGrid}	$U_{\text{CentralGrid}}$
	V	V	V	V	V	V
#1	4800	4800	8000	8000	1100	2240
#2	4000	4000	8000	8000	1200	2190
#3	3000	3000	8000	8000	1380	2120
#4	2000	2000	8000	8000	1500	2140

Table A.2: TOFMS settings used in this thesis to obtain mass spectra of doped or bare He droplets up to a mass < 7000 u. The given values, especially the ones for the deflection unit, correspond to the ones set directly at the TOFMS power supply, not the ones read in by the analog-to-digital converter (ADC).

Ion source	
Filament current	2.1 - 2.2 A
electron energy	89 eV
resulting electrometer current	in the range of 1 μA
Voltage settings	
HV settings	#3 in Tab. A.1 → last- and central grid alternately adjusted for best resolution
repeller offset	0
mass filter	off
deflect-x	5.5
deflect-y	5.5
MCP	2.3 - 2.5 kV depending on the mass of interest
Post acceleration	20 kV
Pulse generator	
repetition frequency	10 kHz
duration e-beam	1 μs
delay ion extraction / ionisation	0 μs
duration ion extraction	2.4 μs
duration mass filter	no influence if the mass filter is off
Fast Multiscaler	
number of sweeps	$2 \cdot 10^4$ - several millions
range	$2.8 \cdot 10^5$ (for a bin width of 1)
bin width	1 - 2
Start/Stop Disc.	0.3/-0.15

Table A.3: TOFMS settings used in this thesis to obtain mass spectra of doped or bare He droplets for big masses up to about 25000 u. The given values, especially the ones for the deflection unit, correspond to the ones set directly at the TOFMS power supply, not the ones read in by the ADC.

Ion source	
Filament current	2.3 - 2.4 A
electron energy	89 eV
resulting electrometer current	15 - 20 μA
Voltage settings	
HV settings	#1 in Tab. A.1 → last- and central grid alternately adjusted for best resolution ($U_{\mathrm{centralgrid}} = 2.25\,\mathrm{kV}$, $U_{\mathrm{lastgrid}} = 1.08\,\mathrm{kV}$)
repeller offset	5.2
mass filter	250 V
deflect-x	5.75
deflect-y	5.6
MCP	2.7 kV
Post acceleration	20 kV
1st aperture	2.7
Pulse generator	
repetition frequency	4 kHz
duration e-beam	20 μs
delay ion extraction / ionisation	0 μs
duration ion extraction	6 μs
delay mass filter / ion extraction	1 μs
duration mass filter	3 μs
Fast Multiscaler	
number of sweeps	$5 \cdot 10^5$ - 10^7
range	$2 \cdot 10^5$
bin width	4
Start/Stop Disc.	0.3/-0.15

A.2 Numerical Methods

For the recognition of peaks in the mass spectra in Chap. 3 the following method was used. In Fig. A.1 a peak from a mass spectrum of an Au doped He droplet beam is plotted. The peak was recognised as such, if

$$\frac{S_g}{S_r} > a \tag{A.1}$$

where S_g is the sum of all counts in the green interval and S_r in the red one.

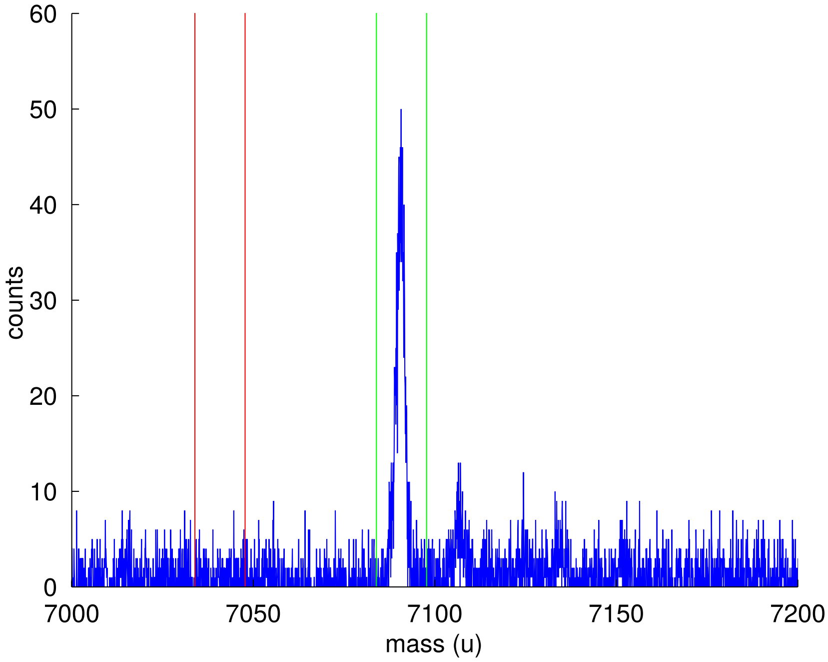

Figure A.1: Clipping from an Au mass spectrum to explanation of the peak recognition.

The intervals were defined as

$$n \cdot m_{\text{element}} \pm (m \cdot f) - m_{\text{offset}} \tag{A.2}$$

where n is the number of atoms in the cluster, m_{element} is the atomic mass of the element to analyse in the mass spectrum, m is the mass in atomic units (x-axis), f is a factor and m_{offset} a mass offset which is 0 for the green interval and non zero for the red interval. The interval has to become wider for bigger masses, because of the constant time resolution and the quadratic time-mass relationship. The values for a, f and m_{offset} used in Eq. A.1 and A.2 are listed in Tab. A.4.

For the plots of the maximum visible cluster size (e.g. Fig. 3.24) the mass for the last recognised peak was plotted. The size distributions were obtained by plotting every recognised peak as the sum of all counts in the green interval in Fig. A.1.

Table A.4: List of the used factors for the peak recognition.

element	experiment	a	f	m_{offset}
Ag	different oven temperature (Fig. 3.17)	1.3	$7.1 \cdot 10^{-4}$	30
Ag	different nozzle temperature (Fig. 3.20)	1.35	$7.1 \cdot 10^{-4}$	30
Au		1.5	$7.1 \cdot 10^{-4}$	50
He		1.8	$1.1 \cdot 10^{-4}$	2

A.3 Material Parameters and Experimental Characteristics

Table A.5: Mean number of He atoms in a droplet for different nozzle temperatures T_0 for a stagnation pressure of $p_0 = 20\,\text{bar}$. The corresponding droplet velocities were extracted from [26].

T_0 (K)	$\langle N_{\text{He}} \rangle$	droplet velocity
6.0	$3.08 \cdot 10^8$ [26]	175
6.5	$5.90 \cdot 10^7$ [26]	194
7.0	$9.64 \cdot 10^6$ [26]	200
8.0	$5.31 \cdot 10^6$ [26]	207
9.0	$1.82 \cdot 10^6$ [26]	223
9.5	$3.25 \cdot 10^5$ [26]	236
10.0	$6.39 \cdot 10^4$ [26]	239
11.0	16960 [94]	276
12.0	11622 [94]	300
13.0	8083 [94]	323
14.0	5735 [94]	340
15.0	4155 [94]	357

Table A.6: Relevant energies for Ag, Au, He and Xe in eV. D_e is the dimer binding energy, $E_{\text{b,bulk}}$ is the bulk binding energy and E_{ion} is the first ionisation energy.

	Ag	Au	He	Xe	H_2O
D_e	1.65 [b]	2.61 [b]	$0.62 \cdot 10^{-3}$ [a]	$19 \cdot 10^{-3}$ [c]	-
$E_{\text{b,bulk}}$	3 [d]	3.8 [d]	-	-	-
E_{ion}	7.58 [e]	9.23 [e]	24.59 [g]	12.13 [f]	12.62 [h]

[a] from ref [43]

[b] from ref [40]

[c] from ref [39]

[d] from ref [95]

[e] from ref [96]

[f] from ref [97]

[g] from ref [42]

[h] from ref [98]

A.4 Estimating the Error in the Oven Temperature

A.4.1 By Observation of the Melting Plateau

Ag has a sufficiently high vapour pressure for the pickup of Ag atoms by the He droplet beam around the melting point ($3.6 \cdot 10^{-3}$ mbar at $T_m = 962\,^\circ\mathrm{C}$, see Fig. 3.9). During a deposition measurement the behaviour plotted in Fig. A.2 was observed.

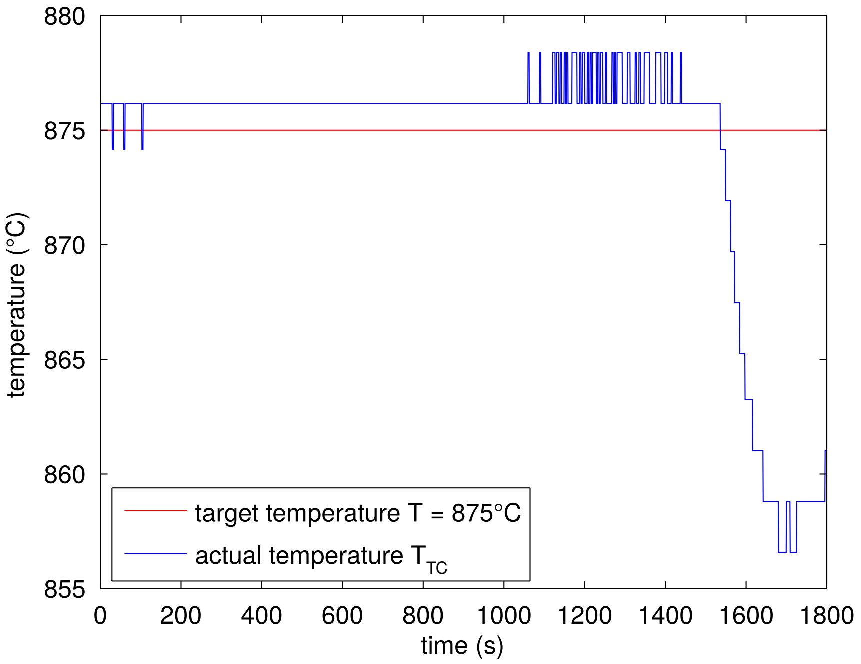

Figure A.2: Plot of the oven temperature T_{TC} determined with a thermocouple, housed in a ceramic husk.

The temperature was held constant by a PID controller. After about 1500 s (the system should be in equilibrium) a sudden drop in the temperature was observed, while the heating power for the crucible was constant. This could signify, that during the observed plateau in Fig. A.2 the solidification heat contributed to the heating power. Until the whole Ag is solid this influence is constant. Afterwards the heating power drops and as a repercussion the temperature drops, if the external heating power stays constant. Simulation of the behaviour of the crucible were performed to check, if the melting and the solidifying really take times in the range observed in the case of Ag [99]. The solidification in the simulation takes about 30 min (see Fig. A.3), which is comparable to the value observed in experiments, where the melting took about 25 min (see Fig. A.2).

With this method the error in the temperature measurement with the thermocouple can be estimated as

$$T_E = T_m - T_{\mathrm{TC,plateau}} = 962\,^\circ\mathrm{C} - 876\,^\circ\mathrm{C} \approx 86\,^\circ\mathrm{C} \tag{A.3}$$

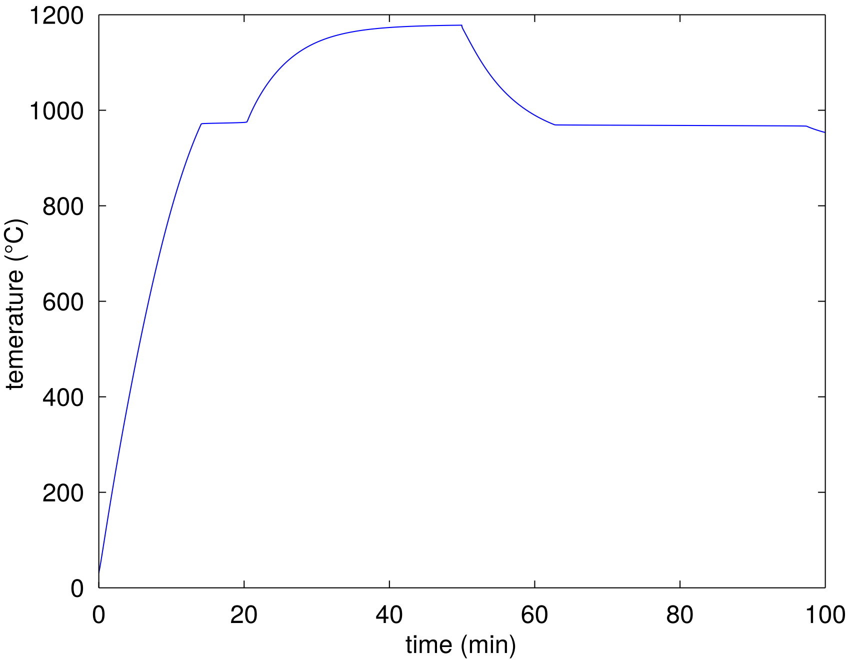

Figure A.3: Simulated temperature of the Ag in a crucible heated with 200 W for 50 min and afterwards heated with 100 W. During the melting of the Ag from minute 14 to 20, the temperature stays constant. When the heating power is lowered, the Ag cools down until the melting temperature is reached again. At minute 95 the solidification is complete and the temperature starts decreasing again [99].

A.4.2 By the Effusive Atom Beam

The symmetric oven design, employed for the evaporation of Au, reminds of a Knudsen-cell. There the mass transport through the effusive beam is proportional to the pressure inside the cell [100]. In case of the Au source the pressure inside is only dependent on the temperature of the crucible. The relationship between vapour pressure and temperature is plotted in Fig. 3.9. This curve can be fitted to the data for the effusive beam, plotted in Fig. 3.12. For the fit, the function for the temperature dependent vapour pressure $p(T)$ was adapted to

$$p_{\text{fit}}(T; T_E, A, p_0) = \frac{p(T - T_E)}{A} - p_0 \tag{A.4}$$

where T_E is the temperature error, which we are interested in, A and p_0 are parameters to fit the curve to the scale of the effusive data. By a fit with the MATLAB-function nlinfit the temperature error was estimated to be $T_E = (85 \pm 55)\,°\text{C}$. Fig. A.4 shows the effusive data with the fitted vapour pressure curve. The error in the temperature measurement is in very good agreement with the one estimated in Sec. A.4.1.

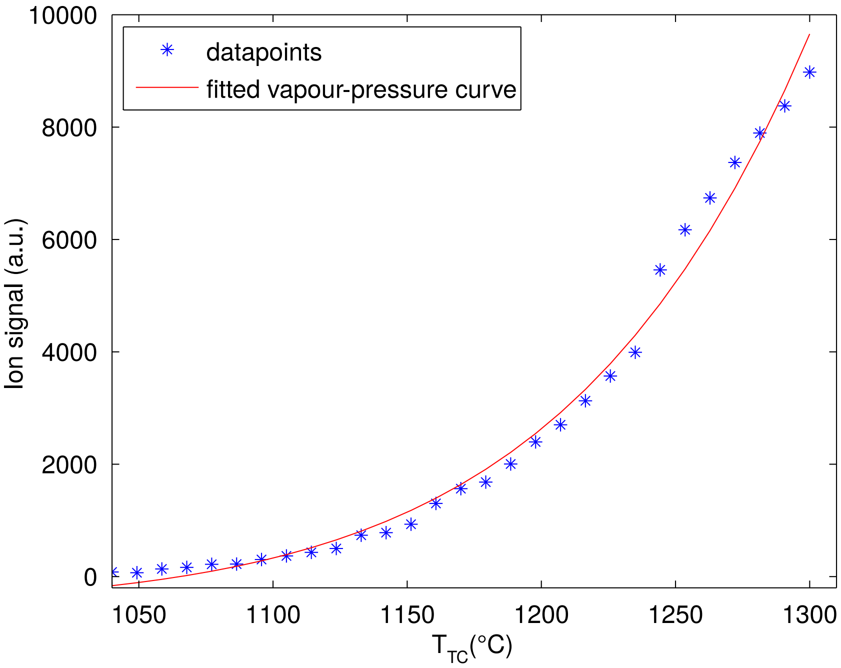

Figure A.4: Plot of the effusive regime of the Au oven with the fitted curve for the Au vapour pressure. The relative uncertainty of the temperature data was estimated to be ±20 °C.

A.5 CD content

- Thesis
- Drawings
    - Apparatus
    - TOFMS schematics
- MATLAB scripts for the recreation of all figures

Bibliography

[1] A. W. Castleman and K. H. Bowen. Clusters: Structure, Energetics, and Dynamics of Intermediate States of Matter. *The Journal of Physical Chemistry*, 100(31):12911–12944, 1996.

[2] S. Yang, A. M. Ellis, D. Spence, C. Feng, A. Boatwright, E. Latimer, and C. Binns. Growing metal nanoparticles in superfluid helium. *Nanoscale*, 5(23):11545–11553, 2013.

[3] A. Boatwright, C. Feng, D. Spence, E. Latimer, C. Binns, A. M. Ellis, and S. Yang. Helium droplets: A new route to nanoparticles. *Faraday Discuss.*, 162:113–124, 2013.

[4] M. A. Garcia. Surface plasmons in metallic nanoparticles: fundamentals and applications. *Journal of Physics D: Applied Physics*, 44(28):283001, 2011.

[5] H. A. Atwater and A. Polman. Plasmonics for improved photovoltaic devices. *Nat Mater*, 9(3):205–213, March 2010.

[6] C. R. Henry. Surface studies of supported model catalysts. *Surface Science Reports*, 31(7–8):231 – 325, 1998.

[7] A. P. Alivisatos. Less is more in medicine - Sophisticated forms of nanotechnology will find some of their first real-world applications in biomedical research, disease diagnosis and, possibly, therapy. *Scientific American*, 285(3):66–73, SEP 2001.

[8] E. C. Corbos, P. R. Ellis, J. Cookson, V. Briois, T. I. Hyde, G. Sankar, and P. T. Bishop. Tuning the properties of PdAu bimetallic nanocatalysts for selective hydrogenation reactions. *Catalysis science and Technology*, 3(11):2934–2943, 2013.

[9] T. J. Kempa, S. Kim, R. W. Day, H. Park, D. G. Nocera, and C. M. Lieber. Facet-Selective Growth on Nanowires Yields Multi-Component Nanostructures and Photonic Devices. *Journal of the American Chemical Society*, 135(49):18354–18357, DEC 11 2013.

[10] I. Borgia, B. Brunetti, I. Mariani, A. Sgamellotti, F. Cariati, P. Fermo, M. Mellini, C. Viti, and G. Padeletti. Heterogeneous distribution of metal nanocrystals in glazes of historical pottery. *Applied Surface Science*, 185(3-4):206–216, JAN 15 2002.

[11] J. P. Toennies and A. F. Vilesov. Superfluid Helium Droplets: A Uniquely Cold Nanomatrix for Molecules and Molecular Complexes. *Angewandte Chemie International Edition*, 43(20):2622–2648, 2004.

[12] C. Callegari and W. E. Ernst. *Handbook of High Resolution Spectroscopy.* edited by F. Merkt and M. Quack (John Wiley & Sons, Chichester), 2011.

[13] J. Harms, J. P. Toennies, and E. L. Knuth. Droplets formed in helium free-jet expansions from states near the critical point. *The Journal of Chemical Physics*, 106(8):3348–3357, 1997.

[14] H. Buchenau, E. L. Knuth, J. Northby, J. P. Toennies, and C. Winkler. Mass spectra and time-of-flight distributions of helium cluster beams. *The Journal of Chemical Physics*, 92(11):6875–6889, 1990.

[15] G. Auböck, J. Nagl, C. Callegari, and W. E. Ernst. Triplet State Excitation of Alkali Molecules on Helium Droplets: Experiments and Theory. *The Journal of Physical Chemistry A*, 111(31):7404–7410, 2007. PMID: 17552501.

[16] M. Hartmann, R. E. Miller, J. P. Toennies, and A. Vilesov. Rotationally Resolved Spectroscopy of SF_6 in Liquid Helium Clusters: A Molecular Probe of Cluster Temperature. *Phys. Rev. Lett.*, 75:1566–1569, Aug 1995.

[17] R. J. Donnelly. *Quantized Vortices in Helium II.* Cambridge University Press, Cambridge, England, 1991.

[18] S. Grebenev, J. P. Toennies, and A. F. Vilesov. Superfluidity Within a Small Helium-4 Cluster: The Microscopic Andronikashvili Experiment. *Science (New York, N.Y.)*, 279(5359):2083–2086, 1998.

[19] L. F. Gomez, E. Loginov, and A. F. Vilesov. Traces of Vortices in Superfluid Helium Droplets. *Phys. Rev. Lett.*, 108:155302, Apr 2012.

[20] N. B. Brauer, S. Smolarek, E. Loginov, D. Mateo, A. Hernando, M. Pi, M. Barranco, W. J. Buma, and M. Drabbels. Critical Landau Velocity in Helium Nanodroplets. *Phys. Rev. Lett.*, 111:153002, Oct 2013.

[21] D. R. Tilley and J. Tilley. Superfluidity and superconductivity. Third edition. *Superfluidity and superconductivity. Third edition*, page 470 pp, 1990.

[22] J. Tiggesbaumker and F. Stienkemeier. Formation and properties of metal clusters isolated in helium droplets. *Phys. Chem. Chem. Phys.*, 9:4748–4770, 2007.

[23] E. L. Knuth and U. Henne. Average size and size distribution of large droplets produced in a free-jet expansion of a liquid. *The Journal of Chemical Physics*, 110(5):2664–2668, 1999.

[24] U. Henne and J. P. Toennies. Electron capture by large helium droplets. *The Journal of Chemical Physics*, 108(22):9327–9338, 1998.

[25] M. Lewerenz, B. Schilling, and J. P. Toennies. A new scattering deflection method for determining and selecting the sizes of large liquid clusters of ^{4}He. *Chemical Physics Letters*, 206(1–4):381 – 387, 1993.

[26] L. F. Gomez, E. Loginov, R. Sliter, and A. F. Vilesov. Sizes of large He droplets. *The Journal of Chemical Physics*, 135(15):–, 2011.

[27] A. Scheidemann, J. P. Toennies, and J. A. Northby. Capture of neon atoms by ^{4}He clusters. *Phys. Rev. Lett.*, 64:1899–1902, Apr 1990.

[28] M. Lewerenz, B. Schilling, and J. P. Toennies. Successive capture and coagulation of atoms and molecules to small clusters in large liquid helium clusters. *The Journal of Chemical Physics*, 102(20):8191–8207, 1995.

[29] C. Kittel. *Introduction to Solid State Physics*. John Wiley & Sons, Hoboken, 2005.

[30] D. M. Brink and S. Stringari. Density of states and evaporation rate of helium clusters. *Zeitschrift für Physik. D, Atoms, molecules, and clusters*, 15(3):257–263, 1990.

[31] E. Loginov, L. F. Gomez, and A. F. Vilesov. Surface Deposition and Imaging of Large Ag Clusters Formed in He Droplets. *The Journal of Physical Chemistry A*, 115(25):7199–7204, 2011.

[32] F. Ancilotto, P. B. Lerner, and M. W. Cole. Physics of solvation. *Journal of Low Temperature Physics*, 101(5-6):1123–1146, 1995.

[33] C. C. Lovallo and M. Klobukowski. Accurate ab initio pair potentials between helium and the heavier group 2 elements. *The Journal of Chemical Physics*, 120(1):246–252, 2004.

[34] K. K. Lehmann and R. Schmied. Energetics and possible formation and decay mechanisms of vortices in helium nanodroplets. *Phys. Rev. B*, 68:224520, Dec 2003.

[35] V. Lebedev, P. Moroshkin, B. Grobety, E. Gordon, and A. Weis. Formation of Metallic Nanowires by Laser Ablation in Liquid Helium. *Journal of Low Temperature Physics*, 165(3-4):166–176, 2011.

[36] F. Baletto and R. Ferrando. Structural properties of nanoclusters: Energetic, thermodynamic, and kinetic effects. *Reviews of modern Physics*, 77(1):371–423, JAN 2005.

[37] H. Haberland. *Clusters of Atoms and Molecules: Theory, Experiment, and Clusters of Atoms*. Springer Series in Chemical Physics. Springer London, Limited, 2011.

[38] W. Ekardt. Work function of small metal particles: Self-consistent spherical jellium-background model. *Phys. Rev. B*, 29:1558–1564, Feb 1984.

[39] K. Sattler, J. Mühlbach, O. Echt, P. Pfau, and E. Recknagel. Evidence for Coulomb Explosion of Doubly Charged Microclusters. *Phys. Rev. Lett.*, 47:160–163, Jul 1981.

[40] M. D. Morse. Clusters of transition-metal atoms. *Chemical Reviews*, 86(6):1049–1109, 1986.

[41] A. M. Ellis and S. Yang. Model for the charge-transfer probability in helium nanodroplets following electron-impact ionization. *Phys. Rev. A*, 76:032714, Sep 2007.

[42] D. Z. Kandula, C. Gohle, T. J. Pinkert, W. Ubachs, and K. S. E. Eikema. Extreme Ultraviolet Frequency Comb Metrology. *Phys. Rev. Lett.*, 105:063001, Aug 2010.

[43] S. Denifl. Formation of cations and anions upon electron interaction with (doped) helium droplets. *The European Physical Journal Special Topics*, 222(9):2017–2033, 2013.

[44] F. M. Penning. Über Ionisation durch metastabile Atome. *Naturwissenschaften*, 15(40):818–818, 1927.

[45] N. Halberstadt and K. C. Janda. The resonant charge hopping rate in positively charged helium clusters. *Chemical Physics Letters*, 282(5-6):409 – 412, 1998.

[46] B. E. Callicoatt, K. Förde, L. F. Jung, T. Ruchti, and K. C. Janda. Fragmentation of ionized liquid helium droplets: A new interpretation. *The Journal of Chemical Physics*, 109(23):10195–10200, 1998.

[47] P. Radcliffe, A. Przystawik, T. Diederich, T. Döppner, J. Tiggesbäumker, and K. Meiwes-Broer. Excited-State Relaxation of ag_8 Clusters Embedded in Helium Droplets. *Phys. Rev. Lett.*, 92:173403, Apr 2004.

[48] C. Bobbert, S. Schütte, C. Steinbach, and U. Buck. Fragmentation and reliable size distributions of large ammonia and water clusters. *The European Physical Journal D - Atomic, Molecular, Optical and Plasma Physics*, 19(2):183–192, 2002.

[49] J. A. Alonso. *Structure and Properties of Atomic Nanoclusters.* Imperial College Press, 2005.

[50] K.-H. Meiwes-Broer (Ed.). *Metal Clusters at Surfaces, Structure, Quantum Properties, Physical Chemistry.* Springer: Berlin, 2000.

[51] P. Thaler, A. Volk, M. Ratschek, M. Koch, and W. E. Ernst. Molecular dynamics simulation of the deposition process of cold Ag-clusters under different landing conditions. *The Journal of chemical physics*, 140(4):044326–(9 pp.), January 2014.

[52] V. N. Popok, I. Barke, E. E. B. Campbell, and K.-H. Meiwes-Broer. Cluster–surface interaction: From soft landing to implantation. *Surface Science Reports*, 66(10):347 – 377, 2011.

[53] G. D. Stein. *Surf. Sci*, 156(44), 1995.

[54] N. F. Aguirre, D. Mateo, A. O. Mitrushchenkov, et al. Helium mediated deposition: Modeling the He-TiO2(110)-(1x1) interaction potential and application to the collision of a helium droplet from density functional calculations. *The Journal of Chemical Physics*, 136(12):–, 2012.

[55] F. Baletto, C. Mottet, and R. Ferrando. Microscopic mechanisms of the growth of metastable silver icosahedra. *Phys. Rev. B*, 63:155408, Mar 2001.

[56] D. Reinhard, B. D. Hall, D. Ugarte, and R. Monot. Size-independent fcc-to-icosahedral structural transition in unsupported silver clusters: An electron diffraction study of clusters produced by inert-gas aggregation. *Phys. Rev. B*, 55:7868–7881, Mar 1997.

[57] A. Volk, P. Thaler, M. Koch, Fisslthaler E., Grogger W., and W. E. Ernst. High resolution electron microscopy of Ag-clusters in crystalline and non-crystalline morphologies grown inside superfluid helium nanodroplets. *The Journal of Chemical Physics*, 138(21):214312, 2013.

[58] K. Michaelian, N. Rendón, and I. L. Garzón. Structure and energetics of Ni, Ag, and Au nanoclusters. *Phys. Rev. B*, 60:2000–2010, Jul 1999.

[59] W. D. Knight, K. Clemenger, W. A. de Heer, W. A. Saunders, M. Y. Chou, and M. L. Cohen. Electronic Shell Structure and Abundances of Sodium Clusters. *Phys. Rev. Lett.*, 52:2141–2143, Jun 1984.

[60] Z. Penzar and W. Ekardt. Electronic shell structure and metal clusters: the self-consistent spheroidal jellium model. *Zeitschrift für Physik D Atoms, Molecules and Clusters*, 17(1):69–72, 1990.

[61] R. M. Cleaver and C. M. Lindsay. Detailed design and transport properties of a helium droplet nozzle from 5 to 50 K. *Cryogenics*, 52(7–9):389 – 397, 2012.

[62] G. Sauerbrey. Verwendung von Schwingquarzen zur Wägung dünner Schichten und zur Mikrowägung. *Zeitschrift für Physik*, 155(2):206–222, 1959.

[63] *Operating Manual Q-pod^{TM} Quartz Crystal Monitor*, 2012.

[64] S. B. Emery, K. B. Rider, B. K. Little, and C. M. Lindsay. Helium Droplet Assembled Nanocluster Films: Cluster Formation and Deposition Rates. *The Journal of Physical Chemistry C*, 117(5):2358–2368, 2013.

[65] S. Kaesdorf. *Manual - Reflectron Time-of-Flight Spectrometer RFT 50*, 2013.

[66] W. C. Wiley and I. H. McLaren. Time of Flight Mass Spectrometer with Improved Resolution. *Review of Scientific Instruments*, 26(12):1150–1157, 1955.

[67] J. L. Wiza. Microchannel plate detectors. *Nuclear Instruments and Methods*, 162:587 – 601, 1979.

[68] Y. Kim and M. E. Rudd. Binary-encounter-dipole model for electron-impact ionization. *Phys. Rev. A*, 50:3954–3967, Nov 1994.

[69] H. Schöbel, P. Bartl, C. Leidlmair, M. Daxner, S. Zöttl, S. Denifl, Tilmann D. Märk, P. Scheier, D. Spångberg, A. Mauracher, and D.K. Bohme. Sequential Penning Ionization: Harvesting Energy with Ions. *Phys. Rev. Lett.*, 105:243402, Dec 2010.

[70] O. Echt, P. Scheier, and Märk T. D. Multiply charged clusters. *Comptes Rendus Physique*, 3(3):353 – 364, 2002.

[71] U. Näher, S. Bjørnholm, S. Frauendorf, F. Garcias, and C. Guet. Fission of metal clusters. *Physics Reports*, 285(6):245 – 320, 1997.

[72] H. Buchenau, J. P. Toennies, and J. A. Northby. Excitation and ionization of 4He clusters by electrons. *The Journal of Chemical Physics*, 95(11):8134–8148, 1991.

[73] P. W. Stephens and J. G. King. Experimental Investigation of Small Helium Clusters: Magic Numbers and the Onset of Condensation. *Phys. Rev. Lett.*, 51:1538–1541, Oct 1983.

[74] H. Schöbel, P. Bartl, C. Leidlmair, S. Denifl, O. Echt, T.D. Märk, and P. Scheier. High-resolution mass spectrometric study of pure helium droplets, and droplets doped with krypton. *The European Physical Journal D*, 63(2):209–214, 2011.

[75] R. Brühl, R. Guardiola, A. Kalinin, O. Kornilov, J. Navarro, T. Savas, and J. P. Toennies. Diffraction of Neutral Helium Clusters: Evidence for Magic Numbers. *Phys. Rev. Lett.*, 92:185301, May 2004.

[76] J. M. Soler, J. J. Sáenz, N. García, and O. Echt. The effect of ionization on magic numbers of rare-gas clusters. *Chemical Physics Letters*, 109(1):71 – 75, 1984.

[77] D. R. Lide. *CRC Handbook of Chemistry and Physics, 72 Ed.* Crc, 1991-1992.

[78] W. R. Shields, V. H. Dibeler, and E. L. Garner. Absolute isotopic abundance of terrestrial silver. *Journal of research of the National Bureau of Standards. Section A. Physics and chemistry*, 66A(1), 1962.

[79] E. Loginov, L. F. Gomez, N. Chiang, A. Halder, N. Guggemos, V. V. Kresin, and A. F. Vilesov. Photoabsorption of AgN 6–6000 Nanoclusters Formed in Helium Droplets: Transition from Compact to Multicenter Aggregation. *Phys. Rev. Lett.*, 106:233401, Jun 2011.

[80] B. J. Winter, E. K. Parks, and S. J. Riley. Copper clusters: The interplay between electronic and geometrical structure. *The Journal of Chemical Physics*, 94(12):8618–8621, 1991.

[81] Friedrich Lindebner, Andreas Kautsch, Markus Koch, and Wolfgang E. Ernst. Laser ionization and spectroscopy of Cu in superfluid helium nanodroplets. *International Journal of Mass Spectrometry*, 2014.

[82] E. C. Honea, M. L. Homer, J. L. Persson, and R. L. Whetten. Generation and photoionization of cold Nan clusters; n to 200. *Chemical Physics Letters*, 171(3):147 – 154, 1990.

[83] M. Theisen, F. Lackner, and W. E. Ernst. Rb and Cs Oligomers in Different Spin Configurations on Helium Nanodroplets. *The Journal of Physical Chemistry A*, 115(25):7005–7009, 2011.

[84] H. Häkkinen and U. Landman. Gold clusters and their anions. *Phys. Rev. B*, 62:R2287–R2290, Jul 2000.

[85] W. A. de Heer. The physics of simple metal clusters: experimental aspects and simple models. *Rev. Mod. Phys.*, 65:611–676, Jul 1993.

[86] F. Marinetti, Ll. Uranga-Piña, E. Coccia, D. López-Durán, E. Bodo, and F. A. Gianturco. Microsolvation of Cationic Dimers in 4He Droplets: Geometries of (He)N (A = Li, Na, K) from Optimized Energies. *The Journal of Physical Chemistry A*, 111(49):12289–12294, 2007. PMID: 17727278.

[87] S. Müller, M. Mudrich, and F. Stienkemeier. Alkali-helium snowball complexes formed on helium nanodroplets. *The Journal of Chemical Physics*, 131(4):–, 2009.

[88] E. Bodo, E. Yurtsever, M. Yurtsever, and F. A. Gianturco. Ionic dimers in He droplets: Interaction potentials for Li2+–He,Na2+–He, and K2+–He and stability of the smaller clusters. *The Journal of Chemical Physics*, 124(7):–, 2006.

[89] F. Ferreira da Silva, P. Waldburger, S. Jaksch, A. Mauracher, S. Denifl, O. Echt, T. D. Märk, and P. Scheier. On the Size of Ions Solvated in Helium Clusters. *Chemistry – A European Journal*, 15(29):7101–7108, 2009.

[90] S. Yang, S. M. Brereton, S. Nandhra, A. M. Ellis, B. Shang, L.-F. Yuan, and J. Yang. Electron impact ionization of water-doped superfluid helium nanodroplets: Observation of He(H2O)n+ clusters. *The Journal of Chemical Physics*, 127(13):–, 2007.

[91] S. Denifl, F. Zappa, I. Mähr, A. Mauracher, M. Probst, J. Urban, P. Mach, A. Bacher, D. K. Bohme, O. Echt, T. D. Märk, and P. Scheier. Ionization of doped helium nanodroplets: Complexes of C60 with water clusters. *The Journal of Chemical Physics*, 132(23):–, 2010.

[92] O. Echt, K. Sattler, and E. Recknagel. *Phys. Rev. Lett.*, 47:1121, 1981.

[93] E. B. Gordon, A. V. Karabulin, V. I. Matyushenko, V. D. Sizov, and I. I. Khodos. Structure of metallic nanowires and nanoclusters formed in superfluid helium. *Journal of Experimental and Theoretical Physics*, 112(6):1061–1070, 2011.

[94] F. Lackner. *Rydberg States of Alkali-Metal Atoms on Superfluid Helium Nanodroplets*. PhD thesis, TU Graz, 2012.

[95] C. Jackschath, I. Rabin, and W. Schulze. Electron-impact Ionization-potentials of Gold and Silver clusters MN-N, N less-than-or-equal-to 22. *Berichte der Bunsen-Gesellschaft-Physical Chemestry Chemical Physics*, 96(9):1200–1204, SEP 1992.

[96] H.-P. Loock, L. M. Beaty, and B. Simard. Reassessment of the first ionization potentials of copper, silver, and gold. *Phys. Rev. A*, 59:873–875, Jan 1999.

[97] F. Brandi, I. Velchev, W. Hogervorst, and W. Ubachs. Vacuum-ultraviolet spectroscopy of Xe: Hyperfine splittings, isotope shifts, and isotope-dependent ionization energies. *Physical Review A*, 64(3), SEP 2001.

[98] R. H. Page, R. J. Larkin, Y. R. Shen, and Y. T. Lee. Highresolution photoionization spectrum of water molecules in a supersonic beam. *The Journal of Chemical Physics*, 88(4):2249–2263, 1988.

[99] P. Thaler. Private conversation. MAR 2014.

[100] A. Freedman, P. L. K. Kababian, Z. Li, W. A. Robinson, and J. C. Wormhoudt. Apparatus for determination of vapor pressures at ambient temperatures employing a Knudsen effusion cell and quartz crystal microbalance. *Measurement Science and Technology*, 19(12):125102, 2008.